

**The quest for accurate three-dimensional water vapour and
temperature fields: A theoretical examination of the capabilities of a
Mesoscale Microwave Radiometer**

By

David Russel Themens

Department of Atmospheric and Oceanic Sciences
McGill University, Montreal
July 2013

A thesis submitted to McGill University in partial fulfillment of the requirements
of the degree of Master of Science

©David Russel Themens, July 2013

Abstract

The initialization of water vapour and temperature fields has long been a concern in mesoscale weather forecasting, where small errors in these fields often produce significant errors in the model characterization of mesoscale processes, such as convective initiation. In order to address this issue, a scanning “Mesoscale” Microwave Radiometer has been designed and built at McGill University with the exclusive goal of accurately providing, or at least constraining, three dimensional water vapour fields.

An assessment of a scanning microwave radiometer’s capability for retrieving water vapour and temperature fields over large (250x250x10km) two- and three-dimensional domains is presented. The information content of an elevation and azimuthal scanning microwave radiometer is assessed using a statistical regression framework. It is shown that a scanning microwave radiometer is, indeed, capable of providing up to 3.9 constraints on water vapour near the instrument decreasing to roughly 0.5 constraints at distances of ~150km, while temperature information is largely restricted to between 1.2 and 0.3 constraints in regions within 50km.

The amount of information inherent in the system is also assessed, where it is found that, in order to constrain water vapour to 0.5g/kg throughout a 2D cross-section through the atmosphere, we require 63.2 independent constraints during July and only 3.2 in January, largely distributed between 500 and 4000m altitude.

Based on these results, we propose possible modifications to the radiometer system to further facilitate its ability to provide accurate water vapour information at mesoscale resolutions within a three dimensional domain.

Résumé

L'initialisation de la vapeur d'eau et de la température est, depuis longtemps, un sujet de préoccupation pour les prévisions météorologiques à la méso-échelle, où de petites erreurs dans ces champs produisent souvent des erreurs significatives dans le modèle concernant la caractérisation des processus à la méso-échelle, telles que l'initiation de la convection. Afin de répondre à cette question, un radiomètre micro-ondes à « méso-échelle » a été conçu et construit à l'Université McGill dans le but exclusif de fournir avec précision, ou au moins de contraindre, les champs de vapeur d'eau en trois dimensions.

Une évaluation de la capacité d'un radiomètre micro-ondes pour recouvrir la vapeur d'eau et température sur un vaste domaine (250x250x10km) en deux et trois dimensions est présentée. Le contenu de l'information d'un radiomètre micro-ondes à balayage en élévation et en azimut est évalué dans un cadre de régression statistique. Il est démontré qu'un balayage radiomètre micro-ondes est, en effet, capable de fournir jusqu'à 3.9 contraintes sur la vapeur d'eau à proximité de l'instrument diminuant à environ 0.5 contrainte à des distances de ~150km, tandis que les informations de température est en grande partie limitée à entre 1.2 et 0.3 contraintes dans les régions plus proche que 50 km. La quantité d'information inhérente au système est également évaluée; on y constate que, dans le but de contraindre la vapeur d'eau avec un précision de 0.5g/kg pour une section 2D à travers l'atmosphère, nous avons besoin de 63.2 contraintes indépendantes en juillet et seulement 3.2 en janvier, distribuées principalement entre 500 et 4000m d'altitude.

Basé sur ces résultats, nous proposons d'éventuelles modifications du système radiomètre pour faciliter sa capacité à fournir des informations précises sur la vapeur d'eau à des résolutions méso-échelle dans un domaine tridimensionnel.

Acknowledgements

I would like to thank Dr. Frédéric Fabry for his guidance and support in supervising this project. I would like to thank Dr. Isztar Zawadski and the McGill Radar group for largely introducing me to this field and giving some necessary insight into the trials of weather forecasting. I would like to thank Véronique Meunier for helping me get this work started, for our discussions, and for supplying the forward model used in this study. I would like to thank Master John Harvie for his guidance over the past two years and for our metaphysical and social discussions that have helped keep me grounded. I would like to thank my mother, Mary-Ellen Themens, for her support and for all of my genetic predispositions (both good and bad). Finally, I would like to thank Rachael Wyatt, without whom I would have no social interaction with the outside world. Her support and encouragement has kept me focused and sane.

Table of Contents

1. Introduction.....	1
1.1. Technologies Currently Available	5
1.1.1. Radiosonde	5
1.1.2. LIDAR.....	6
1.1.3. Radar Reflectivity.....	11
1.1.4. Global Positioning System	13
1.1.5 Passive Remote Sensors	17
1.2 Microwave Radiative Transfer.....	19
1.3 Principles of Microwave Radiometry	23
1.4 Microwave Radiometers	26
1.4.1 Previous Systems.....	26
1.4.2 Scanning	27
1.4.3 The McGill Mesoscale Radiometer.....	29
1.5 Previous Studies	31
2. Retrieval Theory	33
2.1 General Principles	33
2.2 Measurement Covariances	38
2.3 A Priori Covariances.....	39
2.4 Sensitivity Kernel.....	43
3. Results and Discussion	46
3.1 A Single Mesoscale Radiometer	47
3.1.1 2D Elevation Scanning.....	48
3.1.2 3D Elevation and Azimuthal Scanning	60
3.2 The More the Merrier.....	66
3.2.1 The Addition of a V-Band Radiometer	67
3.2.2 Multiple Mesoscale Radiometers	71
3.3 How much information do we need?	79
3.4 Sensitivity to A Priori and Measurement Covariances	85

3.5 Instrument Optimization	93
4. Conclusions.....	97
5. Future Work	101
References.....	107

1. Introduction

The ability to properly model convection within large Numerical Weather Prediction (NWP) architectures becomes extremely important in summer periods. At the moment Quantitative Precipitation Forecasting (QPF) demonstrates relatively low forecast skill during the summer, when convective processes are prevalent (Weckwerth et al., 2004).

Weather forecasting is a chaotic process, extremely sensitive to initial conditions. It is thereby crucial that these initial conditions be accurately constrained at appropriate resolutions for the scale of atmospheric phenomena being modeled. The above mentioned weakness in modeling convection has prompted significant interest in the development of a network of instruments capable of constraining water vapour and temperature over a large domain (Weckwerth et al., 1999; Hardesty et al., 2012). Our study focusses on the assessment of the capabilities of a radiometric instrument for meeting this need.

Water vapour and temperature are perhaps the most crucial fields to constrain within convection. This is largely due to the strong dependence of convection on the vertical profile of equivalent potential temperature, where the location and occurrence of convection is strongly dependent on Convective Inhibition (CIN) and the intensity of convective cells is strongly related to the Convective Available Potential Energy (CAPE). The sensitivity of convection to thermodynamic properties within the lower atmosphere is highlighted in Crook (1996), Fabry (2006), and Bodine et al. (2010) through their assessments of the impact of thermodynamic properties on CAPE and CIN.

Crook (1996) demonstrates that convection is most sensitive to the vertical gradient of temperature and water vapour within the boundary layer. CAPE was found to be most sensitive to water vapour variability, where a change of 1g/kg across the boundary layer could result in a change in CAPE of 600 J/kg, more than twice the effect of a 1 K change in temperature. CIN was found to be most sensitive to temperature variability, where the above errors in temperature would be approximately five to six times more significant than the corresponding errors in water vapour. Fabry (2006) and Bodine et al. (2010), however, found that, at scales less than ~20km, moisture variability can have a stronger impact on CIN than that temperature. Nonetheless, these studies highlight the sensitivity of CAPE and CIN, and thereby convection, to thermodynamic properties.

In Sun (2005) and Fabry and Sun (2010), the effects of initialization and assimilation errors in mesoscale modeling are evaluated. Sun (2005) demonstrates that the initialization of water vapour and temperature fields can have a significant impact on the structure, development and progression of convective and meso- γ features. Fabry and Sun (2010) goes one step further, identifying the effects of initialization errors of different fields on one another. They conclude that initial condition errors in one variable begin to contaminate other variables quickly (within 15 minutes) after initialization and that initial errors are indiscernible after six hours. They also, use initialization errors, comparable with current standards, to determine the effects of different initial condition errors on forecast error, concluding that errors in midlevel moisture caused the greatest uncertainty in the

resulting forecasts. These studies beg the question: what amount of initial error is tolerable for assimilation into forecast models?

Based on the results of Crook (1996), the 1998 NCAR-NOAA Lower Tropospheric Water Vapour Workshop suggested that accuracies of 0.4 g/kg and 1 K for water vapour and temperature, respectively, were necessary in order to accurately model storm strength and initiation (Weckwerth et al. 1999). In the more recent 2011 Thermodynamic Profiling (TPT) Workshop, it was suggested that accuracies in water vapour and temperature of 1 g/kg and 1 K, respectively, would be sufficient for operational forecast applications (Hardesty et al., 2012). These assessments, however, are, again, largely based on the results of Crook (1996). The horizontal and vertical resolution of these measurements is the next concern. The 2011 TPT workshop suggests that resolutions of 50 to 100 meters in the atmospheric boundary layer (ABL) and ~500 meters above are necessary for the vertical. For the horizontal, resolutions of 200-3000 meters for weather forecasting and less than 20 km for QPF were deemed necessary by the same workshop. Hewison and Gaffard (2006), however, suggest that horizontal resolutions of 1 to 30 km for temperature and 3 to 30 km for water vapour would provide significant benefit for NWP, while resolutions greater than these would provide little further benefit.

As will be shown in Section 1.1, at the moment, there exists no system capable of meeting all of the above criteria for either water vapour or temperature, making the goal of establishing a network of thermodynamic profiling instruments unfeasible with current technologies. In this study, we build on the

work of Fabry and Meunier (2009) and assess the capability of a scanning microwave radiometer to meet the above criteria for water vapour and temperature over a large horizontal domain (over 100x100km). In addition to evaluating the capabilities of a Mesoscale Radiometer, we also briefly attempt to quantify the amount of information that is necessary in order to describe these fields to accuracies of 1 K and 0.5 g/kg for temperature and water vapour, respectively: in effect assessing the true resolution necessary in order to specify these fields to the above accuracies throughout the atmosphere.

We shall first consider the status of currently available measurement systems capable of providing temperature and/or water vapour information in Section 1.1. This is followed by a brief introduction to radiative transfer theory and microwave radiometry in Sections 1.2 and 1.3. A “Mesoscale Radiometer”, currently under construction at McGill, will be discussed in Section 1.4. In Section 2, information and retrieval theory will be introduced. In Section 3.1, we shall present an evaluation of this system’s capabilities for both elevation and azimuthal scanning. The capability of multiple instruments will be presented in Section 3.2, an assessment of the information necessary to constrain water vapour and temperature fields will be presented in Section 3.3, and the sensitivity of retrievals to measurement errors and an exploration of potential expansions upon the system’s current design will be presented in Section 3.4 and 3.5. Finally, in Sections 5 and 6, we shall conclude with a discussion of the enormous amount of work remaining to be done in order to fully capitalize on the capabilities of a scanning microwave radiometer.

1.1. Technologies Currently Available

In this section we will discuss the capabilities, costs, and limitations of current technologies available that provide some measure of atmospheric water vapour and/or temperature. As the focus of this study is towards measurements of mesoscale phenomena, which have both small spatial and short temporal scales, we will largely restrict the following discussion to ground-based measurement techniques, which can generally guarantee high temporal resolutions. While some satellite-born instruments are capable of meeting (and even exceeding) at least some of our needs, we have neglected them in this study due to the high cost of deployment.

1.1.1. Radiosonde

It is somewhat ironic that we must begin this section with a discussion of a ground-launched instrument that is both restricted to near-vertical profiling and has poor temporal resolution capabilities; the instrument in question being the radiosonde. It is crucial to mention radiosondes, as they encompass the majority of currently available water vapour and temperature information incorporated into synoptic weather forecasting and sub-synoptic reanalysis. The radiosonde, an ensemble of precise instruments typically launched via balloon, is capable of accurately measuring profiles of pressure, humidity, temperature, and, at times, horizontal wind speed and direction. The high accuracy and vertical sampling

frequency of these systems insures that radiosondes are capable of resolving important vertical structures, such as capping inversions and veering shear.

These systems are, however, marred by high instrument and manpower costs and thus are typically only launched between 2 and 4 times per day (in North America) (Hardesty et al., 2012). Such low temporal resolution and the lack of information on the horizontal distribution of crucial meteorological fields make radiosonde data greatly insufficient when considering mesoscale phenomena. This highlights the focus of this study, where we shall attempt to resolve the limitations of radiosondes through the use of a scanning microwave radiometer, which we believe to be capable of providing water vapour and temperature information both at higher temporal resolution and over a significant three-dimensional domain.

1.1.2. LIDAR

LIDAR is a far more attractive measurement system, capable of providing temperature and water vapour information at similar spatial resolution and accuracy to the radiosonde but also sampling at much higher temporal resolution.

LIDARs are active remote sensing instruments that transmit highly focused light of wavelength typically within the 250 – 20000 nm range. This transmitted light is scattered by a target molecule within the atmosphere and measured by a receiver telescope. The radiance measured by the instrument is given by the LIDAR equation detailed below

$$P(R) = KG(R)\beta(R)T(R) \quad (1.1)$$

where P denotes the power detected at the receiver from a range R , K is a LIDAR system performance factor, $G(R)$ is a geometric factor, $\beta(R)$ is the backscatter coefficient at range R , and $T(R)$ is an atmospheric medium transmission term (Weitkamp, 2005; Bösenberg, 1998). For a more detailed description of the LIDAR equation and its components, the interested reader may consult Weitkamp (2005).

There are two LIDAR system types typically used for tropospheric remote sensing, namely Raman and Differential Absorption LIDAR (DIAL). In the case of Raman LIDAR, temperature profiles are derived through the use Raman Scattering from two separate rotational Raman lines. Raman scattering is an inelastic scattering process under which a rotational-vibrational energy transition is induced in the scattering target (Grant, 1991; Weitkamp, 2005). This causes the scattered light to be shifted by a frequency proportional to the energy consumed or released in the transition. This frequency shift has significant implications on the LIDAR equation (1.1) that are beyond the scope of this work; nonetheless, for details Grant (1991) or Weitkamp (2005) can be consulted.

In the case of temperature profiling, the ratio of the detected power between the two wavelengths (typically N_2 lines) is taken. Undertaking a series of simplifications and rearranging the ratio of the LIDAR equations for both wavelengths, one arrives at the following relation for the temperature

$$T = \frac{b}{a - \ln Q} \quad (1.2)$$

where Q is the ratio of the detected power from both wavelengths, b is simply the difference between the energies of the two target lines divided by the Boltzmann constant and a is a function of the differential backscatter cross-section for the Raman lines (Weitkamp, 2005). To minimize errors, a further expansion is undertaken giving for temperature

$$T = \frac{b}{a - \ln Q} + c \left(\frac{b}{a - \ln Q} \right)^2 + d \quad (1.3)$$

where c and d are calibration coefficients to be determined using measurements from another device, such as a radiosonde (Weitkamp, 2005). Different formulations of (1.3) exist but the principle remains the same.

For measuring water vapour using Raman LIDAR, the two wavelengths are chosen such that one is a water vapour Raman line and the other is a Raman line from some reference species (say N_2). The mixing ratio using this technique is then given as

$$w(z) = C \delta \frac{P_H(z)}{P_{ref}(z)} \quad (1.4)$$

where C is a calibration constant to be determined using alternative measurements from, for example, a radiosonde, P_H is the power measured from the water vapour line, P_{ref} is the power measured from the reference line, and δ is the ratio of the integrated extinction of both signals (Weitkamp, 2005). Unfortunately, the fact that an inelastic scattering mechanism is targeted leads to some ambiguity in

daytime Raman LIDAR measurements, due to solar radiation contamination, that has consequences on the accuracy and range of Raman profiling during these periods.

In the DIAL technique, two signals are used: one signal is chosen such that it lies directly on the absorption line of the desired target species; the second signal is chosen off of the same absorption line. DIAL uses the differential absorption of these two signals to infer the density of the target species.

Employing the following relation, derived from a manipulation of the ratio of the LIDAR equation for each line, we have

$$\rho(r) = \left(\frac{-1}{2D}\right) \frac{d}{dr} \ln \left[\frac{P_{off}(r)}{P_{on}(r)} \right] \quad (1.5)$$

where ρ is the density of the target, P_{off}/P_{on} is the power measured by the LIDAR system from the wavelength off/on the water vapour line, r is the range, and Da is the differential absorption cross-section for the target species at both wavelengths (Grant, 1991).

DIAL is a powerful technique for determining the density of various atmospheric constituents but is incapable of determining temperature and requires more complex instrumentation. In the case of water vapour, the technique avoids the sensitivity and daytime solar contamination issues that tend to plague Raman scatter mixing ratio measurements, compromising the capability for temperature profiling in favour of more accurate water vapour measurements up to a higher altitude than that afforded by Raman LIDAR. Both of these LIDAR techniques

are capable of directly measuring thermodynamic parameters (water vapour density and/or temperature) at accuracies and resolutions meeting or exceeding the criteria listed in Section 1.1. The capabilities of example Raman and DIAL LIDARs are listed in Table 1.1.

Table 1.1 Capabilities of example autonomous LIDAR systems (Hardesty et al., 2012)

Name	Type	Approximate Initial Cost (\$K USD)	Operating Cost (\$K USD)	Variable Measured	Accuracy	Resolution		Maximum Range	Reference
						Vertical	Temporal		
RALMO	Raman	600 -700	15 - 20	Temperature	~0.5K	< 6.5km: 15-30m	< 4km: 10 min	5km Day	<i>Dinoev et al. (2012)</i>
				Water Vapour	< 5%	> 6.5km: 100-300m	> 4km: 30min	12km Night	
IMK-IFU	DIAL	> 600	10	Water Vapour	< 5%	50-250m	41s	~12km	<i>Vogelmann and Trickl (2008)</i>

Although LIDAR systems are accurate, high resolution instruments, there exist significant limitations that make their use less than ideal. First, these systems are prohibitively expensive to purchase and operate, requiring regular component calibration and replacement. Second, Raman LIDAR is extremely sensitive to solar radiation contamination, limiting its capability to profile water vapour and temperature during daytime periods (generally limited to below 5 km during the daytime). Finally, LIDAR systems cannot be used during precipitation or in the presence of cloud liquid water due to high scattering.

There has also been recent interest in undertaking scanning with LIDAR systems. In the past, the possibility of scanning was ignored due to eye safety concerns, but, with the development of modern systems, Raman LIDARs are capable of being eye-safe. DIAL systems, however, remain incapable of eye-safe, low level scanning. That said, it remains to be seen whether these systems could provide information over an appreciable horizontal domain, as beam attenuation becomes a significant issue within the lower atmosphere. Thus, at the moment,

LIDAR systems would be limited to high temporal resolution, vertical profiling of the atmosphere and could merely serve as “radiosonde replacement” instruments, largely used in a network conformation for capturing synoptic-scale variability or for boundary-layer process studies.

1.1.3. Radar Reflectivity

Initially presented in Fabry et al. (1997), radar reflectivity retrievals take advantage of the nuisance of ground targets to produce near surface water vapour and temperature information. The speed of propagation of an electromagnetic wave within a medium is controlled by the refractive index of that medium, where the time of travel of a wave between two points in space is given by

$$t = 2r \frac{n}{c} \quad (1.6)$$

where r is the distance between the two points, n is the index of refraction, and c is the speed of light in a vacuum (Fabry et al., 1997). Thus, if one can infer the time of flight of the signal, one can also determine the refractive index of the medium. Unfortunately, this would require that one know the exact location of the ground targets to extreme accuracy. Recognizing that doing so is unfeasible, given the dynamic nature of some targets and the accuracy needed, only the difference in phase between the current time and some reference time, when the state of the atmosphere is well known (typically when the moisture field is

homogeneous and constant in time) is used. The difference in phase between those periods is given by

$$\Delta\phi = \frac{4\pi fr}{c} \Delta n \quad (1.7)$$

where f is the frequency of the signal and Δn is the difference in phase between both times (Fabry, 2004). Thus, if one knows the difference in phase between both times and the refractive index at the reference time, one can determine the refractive index at any time of interest. This information can be converted to useful atmospheric information through the use of the following relationship proposed in Thayer (1974) and revised in Bevis et al. (1994)

$$N = k_1 \frac{P}{T} + k_2 \frac{e}{T} + k_3 \frac{e}{T^2} \quad (1.8)$$

where P is the pressure in millibars, T is the temperature in kelvin, e is the water vapour pressure in millibars, $k_1 = 77.60 \text{ K/hPa}$, $k_2 = 70.4 \text{ K/hPa}$, $k_3 = 3.739 \times 10^5 \text{ K}^2/\text{hPa}$, and N is the refractivity given by

$$N = (n - 1) \times 10^6 \quad (1.9)$$

While there are some challenges in inverting this information into thermodynamic properties directly, the above relations allow for the potential to assimilate the raw refractivity information into forecast models.

There are several advantages to refractivity fields inferred in this manner, the most direct being that this information comes at nearly no cost to the user, as it can be derived from an already established network of radar stations. The high horizontal resolution of these refractivity fields is unrivalled, providing information on near-surface sub-meso- γ moisture variability, which can be used to infer variations in CIN (Bodine et al., 2010).

While there has been considerable work identifying the utility of these near surface refractivity fields, there remains significant work to be done in order to make full use of this data. In particular, while CIN is useful in convective initiation studies, complementary observations of CAPE are necessary in order to correctly observe convection. Thus, the limitations of this information are fairly obvious: the maximum range over which refractivity fields can be constructed is generally only 20-40 km, due to the curvature of the earth; and the refractivity measurements are limited to near surface altitudes, restricting their utility. While this information can be quite useful and will improve our knowledge of the near-surface atmosphere, it cannot be viewed as a solution to the issue of insufficient lower atmospheric moisture and temperature information due to these limitations.

1.1.4. Global Positioning System

Since the launch of the first Global Positioning System (GPS) satellites in 1978, global navigation satellite system (GNSS) data has found utility in various fields, never before envisioned. GPS broadcasts two L-band signals at 1575.42 MHz and 1227.6 MHz from an orbit of roughly 20200 km. These signals experience delays as a result of atmospheric refractive index, similar to those

experienced by radar signals; thus, using similar techniques, it is possible to determine this refractive index and thereby infer information on atmospheric variables.

Unlike radar refractivity, GNSS has the advantage that signal delays can be estimated directly but has the disadvantage of only have a few ray paths and with no range gate. The slant total delay (STD) imposed on a GNSS signal received by a dual-frequency receiver from atmospheric constituents is calculated through the use of a precise point positioning (PPP) or double-differencing technique that takes advantage of extremely accurate clock and orbit information (see Leick, 2004). This STD can be related to the refractivity through

$$STD = 10^{-6} \cdot \int_S N ds \quad (1.10)$$

where the integral is taken over the entire path, S , between the satellite and the receiver. While this general form of the STD can be useful, it is often preferred to separate it into hydrostatic (dry) and wet atmospheric components in order to determine water vapour fields. This is done by first modeling the Zenith Hydrostatic Delay (ZHD) using the following

$$ZHD = \frac{0.0022768 p_o}{f(\varphi, H)} \quad (1.11)$$

where p_o is the pressure at the antenna in hPa and $f(\varphi, H)$ is given by

$$f(\varphi, H) = 1 - 0.00266 \cos(2\varphi) - 0.00028H \quad (1.12)$$

where φ is the geodetic latitude and H is the height above the geoid in km (Bender et al., 2011). This is then mapped to the slant path using a geometric mapping function or that of Neill (1996). One must merely remove this mapped hydrostatic delay from the STD to estimate the slant wet delay (SWD). The wet refractive index associated with the SWD is simply given by the sum of the second and third terms of (1.8). Using a tomographic or Optimal Solution (OP) method with a sufficiently dense network, these STD or SWD can be inverted to determine three dimensional water vapour fields.

In the absence of a dense enough network of receivers, the SWD can be used to determine the slant integrated water vapour (SIWV) through the following relationship

$$SIWV = M \times SWD \quad (1.13)$$

where M is given by

$$M = \frac{10^6 m_w}{\left(k_2 - k_1 \frac{m_w}{m_d} + \frac{k_3}{T_m}\right) R} \quad (1.14)$$

where m_w is the molar mass of water vapour in kg/kmol, m_d is the molar mass of dry air in kg/kmol, R is the universal gas constant ($8.3145 \text{ J K}^{-1} \text{ mol}^{-1}$), the coefficients $k1$, $k2$, and $k3$ are as they were defined in (1.8), and T_m is given by

$$T_m = 70.2 + 0.72T_o \quad (1.15)$$

where T_o is the surface temperature (Foelsche and Kirchengast, 2001). This SIWV can serve as a constraint in data assimilation modeling and is useful in climate studies.

While GNSS promises to provide a plethora of information, there are some significant drawbacks in its application. Due to multipath and mapping errors, only ray paths from above 5° elevation are used. This means that after a range of ~ 35 km, there are no ray paths within the boundary layer, making a very dense network of these receivers necessary to capture boundary layer water vapour fields. Also, there are typically only 5-12 GPS satellites in view at mid-latitudes for each receiver, again meaning that a very dense network is necessary in order to get sufficient voxel coverage for tomographic inversion. The latter drawback can be mitigated through the use of Galileo and GLONASS satellites, which would approximately double the number of available ray paths.

GPS data has a variety of uses outside of atmospheric research that make establishing a very dense network of receivers at least feasible. GPS can be used in geodetic research, ionospheric reconstruction and space plasma research, and geological tectonic research, where all of these groups are in the process of network development campaigns. The wide variety of uses for these instruments insures that funding for such a network can be garnered from several government sources and private industry.

1.1.5 Passive Remote Sensors

The main focus of this study is on the capabilities of a radiometer system for meeting the criteria set out in our introduction. A radiometer is a passive remote sensing instrument that measures the thermal energy, naturally emitted by atmospheric constituents, and exploits their absorption features to determine their temperature and density profiles. Since this technique is both indirect and must address the issue of ill-posed retrieval when converting integrated radiances to the profile quantities, there are significant limitations to its use; namely, these instruments are only capable of providing between ~ 2 and ~ 6 constraints on water vapour and temperature in the vertical and thus retrievals using these instruments suffer from low resolution (Löhnert et al., 2009). For shear vertical profiling these instruments are vastly inferior to current DIAL or Raman LIDAR technologies (except perhaps in their low cost of deployment and operation), but if used in a scanning conformation, these instruments could, potentially, provide forecasters with the water vapour and temperature constraints they so very need. This capability, however, has largely not been assessed, due to concerns that the information from these instruments would be limited to a relatively small domain about the instrument and to the significant increase in the cost of these instruments as scanning at low elevations is incorporated.

There exist two primary types of ground-based radiometry, namely infrared and microwave radiometry. Both of these techniques have relative strengths and weaknesses. While infrared radiometers generally provide more water vapour and temperature information, they cannot remotely sense

information in the presence of liquid water, due to high scattering and dominating liquid water contributions to their detected radiance (Löhnert, et al; 2009). The microwave spectrum, however, is far less sensitive to liquid water contributions and can thus be used in nearly all atmospheric conditions. Also, infrared radiances tend to be far more nonlinear, with respect to water vapour or temperature, than microwave radiances. This makes infrared instruments far more sensitive to the retrieval technique used than corresponding microwave instruments. In this study, our interests focus on the capabilities of microwave radiometry due to the relative simplicity of the instrument and capability for all-weather autonomous operation.

All of the instruments of sections 1.1.2 through 1.1.4, have aspects that make them more desirable than a radiometer: LIDARs profile information at much higher resolution and accuracy; Radars are capable of providing high resolution near-surface horizontal fields of water vapour, which are inaccessible to radiometers even in scanning conformation, require little investment in instrumentation, and provide useful precipitation parameters; and finally GPS is a cheap instrument to implement that can be entirely autonomous and provides information useful to multiple disciplines outside of atmospheric research. However, none of these instruments, except perhaps the deployment of an extremely dense network of GPS receivers, meet the combined coverage and accuracy requirements outlined in our Introduction. It is our hypothesis that, through scanning, a microwave radiometer is capable of meeting the desired criteria; thus, this study will undertake several theoretical experiments, using

various configurations of a radiometer recently developed at McGill, to assess this capability.

The principles of microwave radiative transfer and radiometric retrieval are discussed in the following sections.

1.2 Microwave Radiative Transfer

Prior to introducing microwave radiometry and alluding to the uses of a radiometer, knowledge of microwave radiative transfer is necessary.

The atmospheric absorption spectrum within the 1 to 100 GHz microwave band is largely dominated by contributions from water vapour and oxygen associated with two distinct spectral features of interest, namely the water vapour line at 22.235 GHz and the 60 GHz oxygen complex. The water vapour feature is a relatively weak single line associated with a rotational transition of its electric dipole within a vibrational state at 22.235GHz followed by a non-resonant continuum that increases monotonically with frequency after roughly 30 GHz (Townes and Schawlow, 1975; Westwater et al., 2005a). The very strong 60 GHz oxygen complex is constructed of 33 resonant spin-rotational transitions between 51.5 and 67.9 GHz (Townes and Schawlow, 1975; Janssen, 1993). Also of interest within this range, is non-resonant continuum absorption of liquid water that increases roughly monotonically as frequency or rain rate increases. These spectral features can be seen in Figure 1.1 for standard atmospheric conditions.

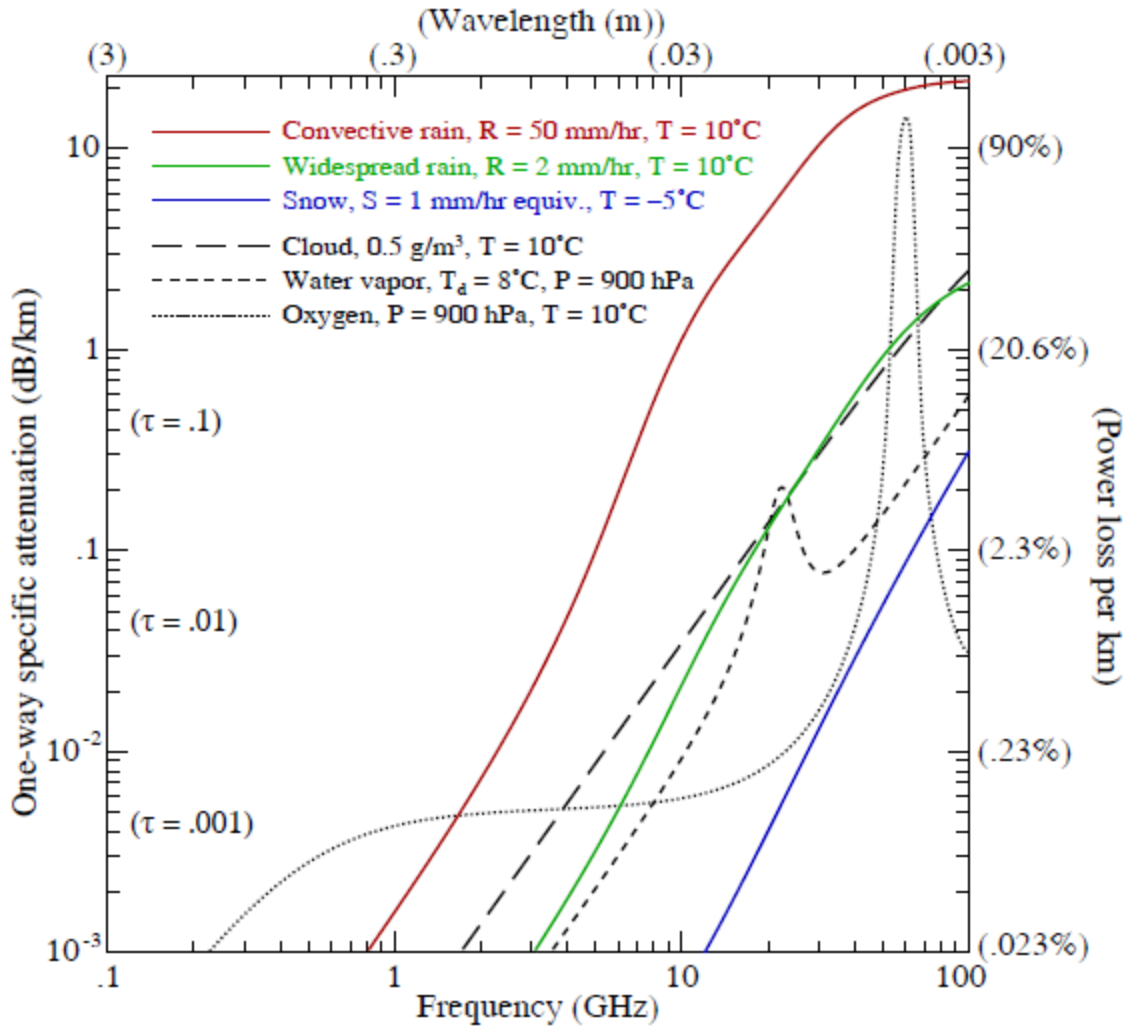


Figure 1.1 Absorption spectra within the microwave band for various atmospheric conditions (Fabry, 2012, personal communication).

You will note that the water vapour line is spectrally wide and that the oxygen complex does not exhibit the distinct features of each line. This is largely the result of pressure broadening and, to a lesser extent, thermal Doppler broadening: pressure broadening results from collisions between molecules that interrupt energy transitions, while thermal Doppler broadening is the result of the Doppler shift associated with the random thermal motions of molecules. The combined effect of both of these broadening mechanisms can be fairly well

modeled by a Voigt profile generated through the convolution of both broadening effects (Goody and Yung, 1989). At high altitudes, pressure broadening weakens and distinct line features of the oxygen complex can be observed.

The emitted radiance of any object is given as that of a corresponding ideal blackbody modified by the emissivity of that object

$$I(\lambda, T) = \varepsilon(\lambda) \cdot B(\lambda, T) \quad (1.16)$$

where $I(\lambda, T)$ is the irradiance of the object, $\varepsilon(\lambda)$ is the emissivity, and $B(\lambda, T)$ is the blackbody radiance associated with temperature T and wavelength λ (Goody and Yung, 1989). In thermal equilibrium, the emissivity of a particular species can be related to the absorptivity of that species through Kirchoff's Law, which states that, in the absence of scattering, any object absorbs and emits the same fraction of incident and outgoing radiance

$$\varepsilon(\lambda) = \alpha(\lambda) = 1 - \tau(\lambda) \quad (1.17)$$

where $\alpha(\lambda)$ is the absorptivity and $\tau(\lambda)$ is the transmittance of the molecule (Goody and Yung, 1989). This means that the absorption spectrum of Figure 1.1 largely dictates how various atmospheric constituents contribute to the radiation detected by a radiometer. The blackbody radiance emitted by a molecule is given by Planck's Law as

$$B(\lambda, T) = \frac{2hv^3}{c^2} \frac{1}{e^{hv/kT} - 1} \quad (1.18)$$

where h is Planck's constant, $\nu = c/\lambda$ is the frequency, c is the speed of light in a vacuum, and k is Boltzmann's constant (Janssen, 1993). For the microwave band (wavelengths between $\sim 1\text{mm}$ and 30cm), this relationship can be approximated, to the first order, by the Rayleigh-Jeans formulation given by

$$B(\lambda, T) = \frac{2kT}{\lambda^2} \quad (1.19)$$

This shows that, in the microwave band, the radiance of an object is roughly linearly related to the temperature of that object. In this approximation, we may define the brightness temperature, the temperature of a perfect blackbody corresponding to the radiance of an object, as

$$T_b = \frac{\lambda^2}{2k} I(\lambda) \quad (1.20)$$

Using the above information describing the radiation emitted and absorbed by particular atmospheric constituents, we may now consider the radiation detected by a ground-based radiometer. All atmospheric constituents emit radiation according to (1.16). The total downwelling radiation detected at the surface is thus composed of contributions from the entire atmosphere along the desired ray path and is given by

$$I_d(\lambda, T) = B(\lambda, T_c) \exp(-\tau_d) + \int_0^\infty B(\lambda, T(s)) \alpha(s) \exp(-\int_0^s \alpha(s') ds') ds \quad (1.21)$$

where T_c is the temperature of the cosmic microwave background ($T_c = 2.75$ K), $T(s)$ is the temperature of the parcel at path location s , $\alpha(s)$ is the absorption coefficient of that parcel, and τ_d is the optical depth of the atmosphere along the ray path given by

$$\tau_d = \int_0^\infty \alpha(s) ds \quad (1.22)$$

Conceptually, these relations state that the total radiation detected at the surface is equal to the sum of the radiances from each parcel along the desired ray path attenuated by the parcels ahead of them. For the sake of simplicity, we have neglected the effect of scattering in these relations; however, some scattering considerations will be discussed in the Future Work section of this study.

1.3 Principles of Microwave Radiometry

Passive radiometer systems measure the intensity of radiation emitted by the atmosphere at various frequencies. As these are integrated measurements of radiation along the ray path, the problem of retrieving atmospheric profiles is ill-posed; thus, information with regards to the structure of the emitting atmospheric constituents needs to be inferred and reconstructed through the use of multiple frequencies sensitive to different depths within the atmosphere. The location

along the ray path at which a particular frequency is sensitive is dependent on the absorptive/emissive properties and the relative abundance of the target constituent, where more opaque frequencies will be most sensitive to the region near the radiometer and less opaque frequencies will provide information from further distances away from the instrument. Ideally, in order to resolve different distances along a ray path, one would choose frequencies such that a range of different opacities are sampled. Based on this, the selection of a radiometer's target frequencies essentially dictates the utility of the instrument.

The sensitivity of measurements by any particular channel to perturbations in the abundance of the target species and their temperature is given as the sum of the contributions from each independent parameter

$$\delta T_b = \int_0^{\infty} (W_T(s)\delta T + W_P(s)\delta P + W_w(s)\delta w + W_{\rho_l}(s)\delta\rho_l) ds \quad (1.23)$$

where δT_b is a perturbation in the measured brightness temperature, and W_T , W_P , W_w , and W_{ρ_l} are temperature, pressure, water vapour mixing ratio, and liquid water density weighting functions, respectively (Westwater et al., 2005b). These weighting functions represent the sensitivity of the measured brightness temperature to changes in atmospheric parameters per unit distance along the ray path. The shape of these weighting functions defines where a channel's information originates along the ray path and can be used to discern the linear independence of the information provided by each channel (Scheve and Swift,

1999). The zenith temperature and water vapour weighting functions for the channels of the radiometer used in this study are presented in Figure 1.2.

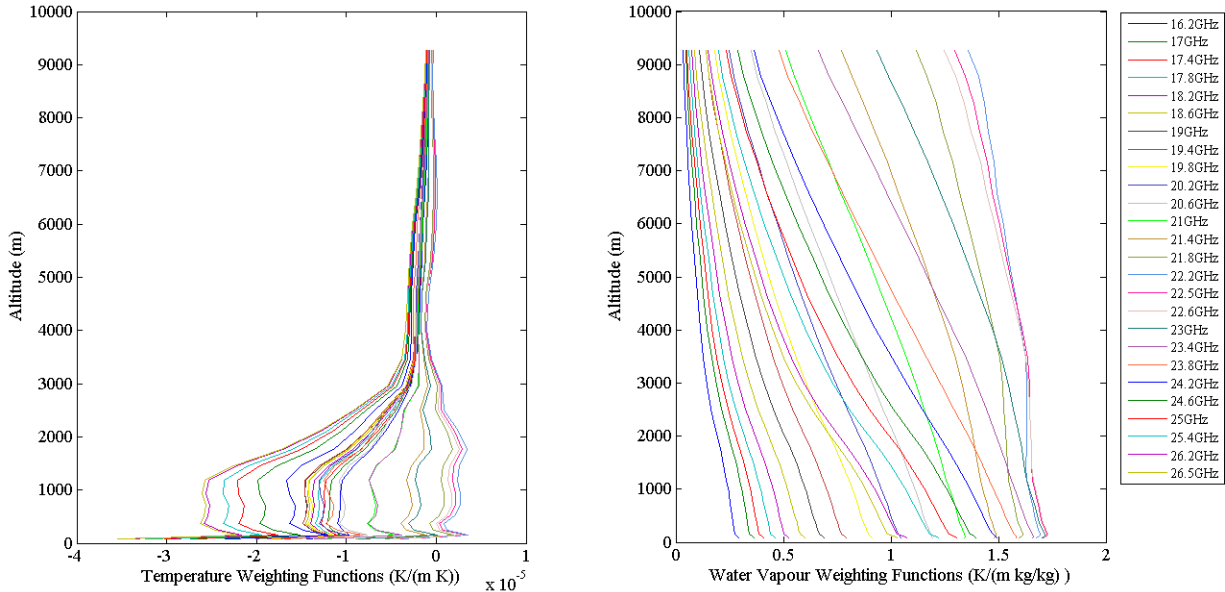


Figure 1.2 Example weighting Functions for temperature (left) and water vapour (right).

For determining atmospheric profiles of temperature or water vapour, particular strategies are generally undertaken. For sensing temperature profile information, frequencies are generally chosen around the 60 GHz oxygen complex. This is due to the fact that oxygen is a well-mixed gas within the atmosphere, where the relative abundance of oxygen, with respect to the atmospheric pressure, is stable and well known; thus, the only remaining unknown variable for retrieval, using these channels, is the temperature of the oxygen. For water vapour remote sensing using a ground-based radiometer, frequencies are generally chosen around the 22.235 GHz water vapour band, where the total contribution to the detected radiation largely originates from atmospheric water vapour. In this case, however, the temperature and the

abundance of water vapour are unknown, leading to a non-linear problem. As an aside, for high latitude, or zenith-pointed instruments mounted at high altitudes, a more opaque water vapour line at 183 GHz is used in addition to the 22.235 GHz line due to the relatively low amounts of water vapour in polar and high altitude regions (Pazmany, 2007). In order to have a good spread of opacities, and thus resolve several distances along a ray path, one will generally select a frequency at the center of an absorption feature, followed by several frequencies on the sloping portion of the line/complex.

1.4 Microwave Radiometers

Microwave radiometers are relatively simple systems consisting of an antenna reflector that focusses downwelling radiation towards a feedhorn. After which the signal is sent through a mixer and amplifier to be followed by a filter that isolates the frequency components of the signal and is interpreted by a detector. The resulting measured radiances from each frequency channel need only be interpreted by the user.

1.4.1 Previous Systems

Most current water vapour radiometers have been designed with vertical profiling in mind and, thus, generally have frequencies between the water vapour line center at 22.235 GHz and the valley region between this line and the 60 GHz oxygen complex (i.e. the more opaque side of the water vapour line). As a vertical ray only travels through a fairly shallow region of water vapour, opaque channels

are needed in order to get useful information and beamwidths can be relatively wide. A list of currently available radiometer systems is presented in Table 1.2.

Table 1.2 *Parameters of currently available Microwave Radiometers*

Radiometer	Beamwidth (°)	Bandwidth (GHz)	Channels	Scanning Capability	References
ADMIRARI	5.0 - 6.5	0.4	X and K band (3 Channels)	Azimuth and Elevation	Battaglia et al. (2010)
ASMUWARA	7.9 - 10.0	4.0 - 0.3	K band, V band and IR (9 Channels)	Azimuth and Elevation	Martin et al. (2006)
HATPRO	2.5 - 3.5	2.0 - 0.1	K and V band (14 Channels)	Azimuth and Elevation	Rose et al. (2005)
MWR3C	3.0 - 3.5	1.9 - 0.3	K and W band (3 Channels)	Azimuth and Elevation	Cadeddu (2012)
MICCY	0.4 - 0.9	1.0 - 0.25	K, V, and W band (22 Channels)	Azimuth and Elevation	Crewell et al. (2001)
MP-3000	2.2 - 6.1	0.4	K and V band (12 Channels)	Elevation	Liljegren (2002)

None of the above systems were designed for the purpose of three-dimensional retrieval; thus, it remains to be seen how they would perform in such an application. Of these systems, the MICCY radiometer of Crewell et al. (2001) is, in the opinion of the author, the most versatile and advanced, but it is likely that its lack of channels at frequencies below the 22.235 GHz water vapour line, would restrict the information retrievable from the system to relatively small horizontal domains in high water vapour conditions.

1.4.2 Scanning

This brings us to a question currently unaddressed within the field; namely, how important is scanning and can scanning provide useful information?

The advantages of scanning with a radiometer are fairly straightforward: scanning allows a radiometer to provide information over large, three dimensional domains, otherwise inaccessible. Less straightforward benefits include the

capability for scanning-based calibration through tipping-curve methods (Janssen, 1993). Also, with the assumption of local horizontal homogeneity, scanning can increase the information available within the boundary layer from low opacity channels, at times even doubling the information content from such instruments (Crewell and Löhnert, 2007; Löhnert et al., 2009).

There are several challenges faced when attempting to undertake scanning with a microwave radiometer, some of the more important being the selection of frequencies to use for such a system, as well as the beamwidth of the instrument, which will have strong implications on the instrument's capability to scan at low elevations.

The selection of the instrument frequencies must be such that information can be resolved at several distances along both low and high elevation scan angles; thus, a spectrum of opacities are necessary, as frequencies useful at zenith may not be useful at low elevations and vice versa. As one attempts to scan in elevation, the target ray travels through more atmosphere; thus, low opacity channels, which would contribute very little information in the vertical, allow an instrument to “see” further along the ray than more opaque channels, contributing useful information at greater distances. This implies that the system will likely require a large number of redundant frequencies. This is also the case, in order to be robust for varying atmospheric conditions, where even moderate changes in the amount of water vapour will have significant implications on the location at which each frequency contributes information. Scheve and Swift (1999) developed a technique for optimizing the frequency selection of an instrument for

vertical remote sensing; though, with the inclusion of a large number of elevation scans, this technique could become non-linear and remains to be tested.

A narrow beamwidth is necessary for low elevation atmospheric scanning for two main reasons: the first being that one should strive to avoid ground contamination, where a wide beamwidth would severely limit the lowest elevation available for scanning; the second being that the lower atmosphere is highly variable, so with larger beamwidths comes a larger spread of atmospheric conditions scanned within a single measurement and an associated, larger, modeling error (Meunier et al., 2012).

These features highlight the purpose of the McGill Mesoscale Radiometer, where 26 frequencies have been selected between 16.2 and 26.5 GHz, encompassing a large spread of opacities, and the beamwidth is kept below 2 degrees.

1.4.3 The McGill Mesoscale Radiometer

The McGill Mesoscale Radiometer was designed expressly for scanning applications; as such, frequencies were selected such that it probes a large spread of opacities while also maintaining a consistently narrow beamwidth. The radiometer's frequencies and bandwidth, in its current conformation, are given in Table 1.3.

Table 1.3 *McGill Mesoscale Radiometer Channel Parameters*

Channel	Frequencies (GHz)				Bandwidth (GHz)
1	16.2	17.4	21.0	22.2	0.2
2	17.0	18.2	21.8	23.0	0.2
3	17.8	19.0	22.6	23.8	0.2
4	18.6	19.8	23.4	24.6	0.2
5	19.4	20.6	24.2	25.4	0.2
6	20.2	21.4	25.0	26.2	0.2
7	22.5				0.4
8	26.5				0.4

The radiometer is an eight channel instrument that uses a digitally tuned oscillator (DTO) to switch across several frequencies. This allows the instrument to, in theory, scan an extremely large number of frequencies within the range allowed by the waveguide, at the cost of undertaking additional sampling. In the case of the Mesoscale Radiometer, the range of frequencies sampled by the instrument was limited largely by the desire to use a single waveguide and thereby keep the cost of the instrument low. As is illustrated in Table 1.3, the current conformation of the instrument has two fixed frequency channels and six switching channels, all of which sampling at 1/60 second. Since the fixed frequencies do not cycle, additional samples can be taken, drastically reducing the measurement errors associated with these channels. Including the time necessary for calibration and noise reduction, a full acquisition cycle takes 1.07 seconds to complete. To insure the capability of scanning at low elevations, the beamwidth is kept relatively constant between roughly 1.4 and 1.7 degrees across all channels. An image of the instrument can be found in Figure 1.3.



Figure 1.3 The McGill Mesoscale Radiometer.

1.5 Previous Studies

Staelin (1966) was the first to use a ground-based, multi-channel radiometer for determining the structure of atmospheric thermal properties. Since then, several studies have further expanded on this concept, where profiles of water vapour, temperature, and liquid water content have been retrieved using microwave radiometry. Recent studies of the vertical profiling capabilities of microwave radiometers (including Crewell and Löhnert (2007), Löhnert et al. (2008), Löhnert et al. (2009), Ebell et al. (2010), Bleisch et al. (2011), Bleisch and Kampfer (2012)) have shown that radiometers are capable of accurate vertical

profiling of water vapour and temperature at low resolutions; however, these studies have ultimately found that such an instrument can only provide between one and four independent pieces of temperature or water vapour information. Only a select few studies have investigated the utility of these instruments for horizontal or three dimensional profiling.

Fabry and Meunier (2009) present preliminary results, where brightness temperature measurements by a scanning microwave radiometer demonstrated notable azimuthal variability associated with a strong horizontal water vapour gradient. Schween et al. (2011) go one step further relating these brightness temperature measurements to estimates of the azimuthal distribution of path integrated water vapour and estimating the direction and intensity of horizontal water vapour gradients. These studies are very preliminary and do not take advantage of a radiometer's capability to resolve information along the ray path.

The only study to date to attempt retrieving three dimensional water vapour profiles using a microwave radiometer is that of Padmanabhan et al. (2009). In that study, three compact four channel radiometers were developed and implemented in a triangular formation with spacing of roughly 10km. The authors showed that a radiometer was in fact capable of determining water vapour fields at fine spatial resolutions over the small domain considered. There are, however, some caveats to that study: the main concern being that the domain is far too small to be considered useful for network implementation. This limited domain was likely chosen to avoid the limitations of only using radiometers restricted to four channels with frequencies chosen similar to those ideal for vertical profiling.

A greater range of opacities would be necessary in order to retrieve information over a larger horizontal domain. Nonetheless, the study is very encouraging, as it essentially serves as a proof of concept for our study, where we will consider a more robust instrument. In our study, however, we will attempt to access the capability for radiometric retrieval over a much larger horizontal domain at lower spatial resolutions.

2. Retrieval Theory

This study undertakes a theoretical analysis of the amount of information retrievable from a scanning microwave radiometer. This requires that we solve the ill-posed, inverse, retrieval problem; as such, we use *a priori* information to constrain the number of possible solution states and then further constrain the remaining set of possible solutions using radiances measured by a microwave radiometer. For that purpose, we employ a fairly standard statistical regression technique; namely, the statistical regression methodologies of Rodgers (2000).

2.1 General Principles

The general purpose of retrieval theory is to transform observations of some measurement field, \mathbf{y} , into a state field, \mathbf{x} , through the inverse use of a forward model or mapping function, $F(\mathbf{x})$. In general, these fields are related through the following

$$\mathbf{y} = \mathbf{F}(\mathbf{x}) \quad (2.1)$$

In the case of two-dimensional retrieval, the measurement field is taken as the brightness temperature measured by a radiometer at the surface and is given by

$$\mathbf{y} = [T_b(f_1, a_1) \quad \dots \quad T_b(f_N, a_1) \quad T_b(f_1, a_2) \quad \dots \quad T_b(f_N, a_2) \quad \dots \quad T_b(f_N, a_M)] \quad (2.2)$$

where $T_b(f_N, a_M)$ is the brightness temperature measured at frequency f_N and elevation angle a_M . The state field of interest is composed of the temperature and water vapour mixing ratio arranged in the following manner

$$\mathbf{x} = [T(x_1, z_1) \quad \dots \quad T(x_1, z_\alpha) \quad T(x_2, z_1) \quad \dots \quad T(x_2, z_\alpha) \quad \dots \quad T(x_\beta, z_\alpha) \quad w(x_1, z_1) \quad \dots \quad w(x_1, z_\alpha) \quad w(x_2, z_1) \quad \dots \quad w(x_2, z_\alpha) \quad \dots \quad w(x_\beta, z_\alpha)] \quad (2.3)$$

where $T(x_\beta, z_\alpha)$ and $w(x_\beta, z_\alpha)$ are the temperature and water vapour mixing ratio, respectively, corresponding to the position at horizontal location x_β and vertical location z_α . We may linearize the forward model of (2.1) to

$$\mathbf{y} = \mathbf{K}\mathbf{x} + \boldsymbol{\varepsilon} \quad (2.4)$$

where \mathbf{K} is the linearized forward model, called the sensitivity kernel or forward model Jacobian, and $\boldsymbol{\varepsilon}$ is the measurement error. If we apply Bayes' theorem and assume that the state and measurement vectors follow Gaussian statistics, we may express the most likely retrieved state through the use of the posterior probability distribution. Doing so, the most likely retrieved state can be expressed in terms of an a priori guess and covariance field

$$\hat{\mathbf{x}} = \mathbf{x}_a + \mathbf{S}_a \mathbf{K}^T (\mathbf{K} \mathbf{S}_a \mathbf{K}^T + \mathbf{S}_\varepsilon)^{-1} (\mathbf{y} - \mathbf{K} \mathbf{x}_a) \quad (2.5)$$

where \mathbf{x}_a is an a priori guess state, \mathbf{S}_a is the covariance matrix associated with the a priori field, and \mathbf{S}_ε is the measurement error covariance matrix (Rodgers, 2000).

This retrieved state has an associated covariance matrix given by

$$\hat{\mathbf{S}} = (\mathbf{K}^T \mathbf{S}_\varepsilon^{-1} \mathbf{K} + \mathbf{S}_a^{-1})^{-1} \quad (2.6)$$

In a linear system, the above can be used directly to determine and characterize the retrieved state; however, radiometric retrievals involve the solution of a nonlinear problem. This requires that one undertake an iterative solution, where the result of the first retrieval is used as the a priori state in the next iteration. Iterations are repeated until a cost function, given by the posterior probability distribution, is minimized. This cost function is given as

$$J(\mathbf{x}) = (\mathbf{y} - \mathbf{F}(\mathbf{x}))^T \mathbf{S}_\varepsilon^{-1} (\mathbf{y} - \mathbf{F}(\mathbf{x})) + (\mathbf{x} - \mathbf{x}_a)^T \mathbf{S}_a^{-1} (\mathbf{x} - \mathbf{x}_a) + c_3 \quad (2.7)$$

where c_3 is a constant (Rodgers, 2000). The minimization of this cost function is undertaken through the use of a Gauss-Newton method or, for increasingly nonlinear systems, a Levenberg-Marquardt method (Levenberg, 1944; Marquardt, 1963). As we do not undertake retrievals in this study and approach our problem through an information theory perspective, we will not delve any further into the process of undertaking a retrieval. The interested reader may consult Rodgers (2000) for more details of this process.

Within the above retrieval framework resides the capability to assess the information content of a radiometer. Using the above framework, one may calculate the averaging kernel matrix of the instrument, given by

$$\mathbf{A} = \widehat{\mathbf{S}}(\mathbf{K}^T \mathbf{S}_\varepsilon^{-1} \mathbf{K}) \quad (2.8)$$

This matrix contains various pieces of information on the characteristics and performance of the retrieval. The rows of this matrix form the averaging kernels of the system. These kernels characterize the sensitivity of the retrieval state to changes in the actual state. An example of the water vapour and temperature averaging kernels for 1D vertical retrieval is presented in Figure 2.1.

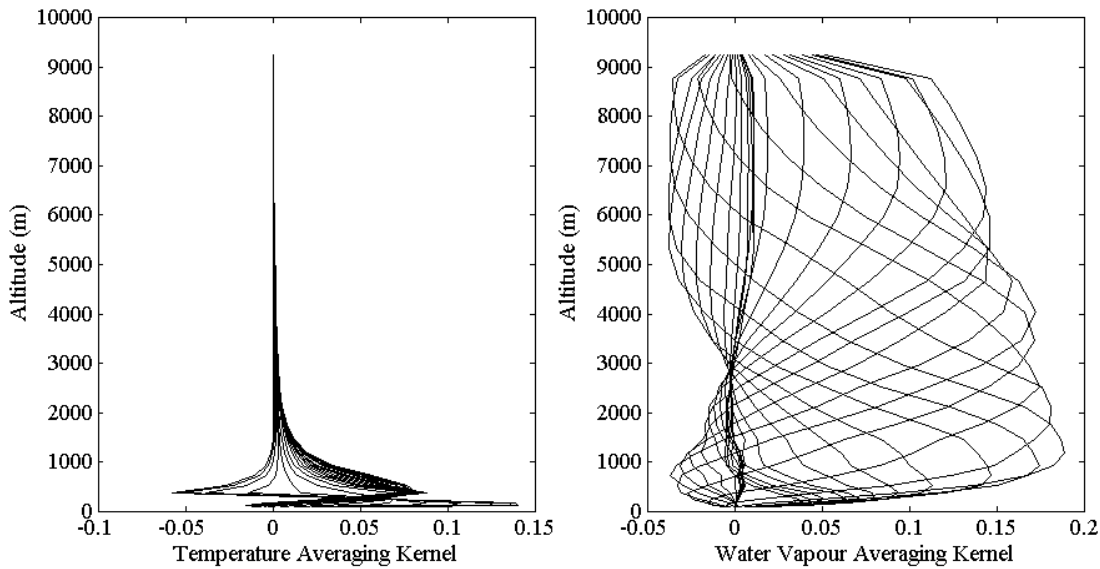


Figure 2.1 Vertical water vapour (left) and temperature (right) averaging kernels for a vertically pointing radiometer on July 1st, 2011 at 01 UTC in the Montreal area.

These averaging kernels represent the partial derivatives of the retrieved state with respect to the elements of the true state, so wide kernels mean that the retrieved state is sensitive to a large area rather than a single, corresponding member of the true state. In that sense they are an indication of the resolution of the retrieval. Similarly the sum of the averaging kernels can be taken as a measure of the overall sensitivity of the retrieval to members of the state vector (Rodgers, 2000).

The diagonal of the averaging kernel matrix contains information with regards to the location and amount of information available within the system, where the individual components of the diagonal can be taken as the number of independent pieces of information associated with a member of the state and its trace can be taken as the total degrees of freedom for signal (DOFs) of the retrieval (Rodgers, 2000). The DOFs of the system represent the total number of

independent constraints that the instrument provides for constraining the a priori to the actual state. In this study, we will make use of these concepts of information theory to assess the capabilities of a microwave radiometer in undertaking elevation and azimuthal scanning.

2.2 Measurement Covariances

As the McGill Mesoscale Microwave Radiometer (MMMR) is currently being upgraded, the instrument measurement covariances required by the above retrieval framework must be estimated analytically. As we do not yet know how the measurement errors are correlated, we ignore off-diagonal elements of the measurement covariance matrix. For our purposes, the diagonal elements of the measurement covariance matrix are chosen as the theoretical thermal noise errors of a Dicke radiometer given by

$$\sigma_T = \frac{2(T_n + T_b)}{\sqrt{B\tau}} \quad (2.9)$$

where T_n is the thermal noise of the instrument, T_b is the measured brightness temperature, B is the channel bandwidth, and τ is the sampling or integration time (Janssen, 1993). In our case, we have assumed a $(T_n + T_b)$ factor of 800K, an integration time of 1/15 seconds, and bandwidths as given in Table 1.3. This corresponds to measurement errors of 0.44K for the varying radiometer channels and 0.31K for the fixed channels.

These errors are only estimates of the system's actual errors and do not account for additional measurement errors associated with the representativeness of the measurements, with profile discretization, with the forward model, and those associated with the instrument calibration. This shortcoming must be addressed prior to undertaking retrievals with the instrument but is not accessible for our proof of concept study. In order to assess the impact of this ambiguity in our assessment of the system's actual measurement errors, we have undertaken a sensitivity study in Section 3.4. Also, methods for calculating these additional errors using the instrument, once operational, are discussed in the Future Work Section of this study.

2.3 A Priori Covariances

The a priori state, \mathbf{x}_a , and its associated covariances, \mathbf{S}_a , have been developed using analyses from the NOAA Rapid Refresh Reanalysis (RAP). RAP provides hourly, three dimensional fields of water vapour, pressure, geopotential height, and temperature over the entirety of North America at 13.545 km horizontal resolution and with 50 hybrid levels in the vertical.

The a priori state is taken as the RAP profile closest to Montreal, where we have adopted the hybrid coordinate system of RAP for our analysis. This choice of the RAP coordinate system for our analysis, allows us to avoid potential correlation artifacts that would result from interpolating to another coordinate system.

The covariances are taken from the monthly climatology assembled from a 500 x 500 km region about Montreal, where we have assumed horizontally isotropic covariances but have made no assumptions with regards to the vertical structure of the covariance field.

Using the isotropic covariance assumption, the covariance field is developed by first isolating all vertical profiles with each desired horizontal separation and concatenating these sets in time (over the course of a month in our case). The covariance of profiles separated by a desired distance is then calculated using this set of data, where this process is repeated for each horizontal separation within the domain. The covariance matrix used in our analysis is then assembled from these covariance sets, where each dimension of the covariance matrix is organized in the same manner as the state vector.

In order to minimize errors in the covariance field associated with smaller sampling sizes at larger horizontal distances of separation (i.e., due to less pairs of profiles being available as we approach the size of the sampling domain), we have limited our retrieval domain to 21 grids at the native horizontal resolution of RAP (i.e. the retrieval domain has be limited to 270.9 km in the horizontal). In the vertical, we have limited our domain to remain within the troposphere, using only 25 hybrid levels, corresponding to an upper bound at roughly 300 hPa.

There are consequences to using a model to generate these covariances in place of actual observations, the most important of which is the tendency for models to smooth out small scale variability, leading to artificially high correlations at these scales. These artificial correlations can produce a non-

positive definite covariance matrix. Eigenvalues of the covariance matrix that are zero or negative imply complete a priori knowledge of the state, where components of the state are not linearly independent of one-another (Rodgers, 2000). A lack of positive definiteness can lead to poorly normalized solutions or negative components in the DOFs determined using 2.8. In most applications of model data for generating a priori covariances, positive definiteness is forced by either reducing the number of elements within the state vector or by modifying the covariances in a physically consistent manner. In the event of using a positive semi-definite covariance matrix (i.e., one where all eigenvalues are positive, but very small or zero-value eigenvalues exist), poor normalization or negative DOF components will only occur if the instrument retrieval information forces the use of these small eigenvalues. Simply put, the use of a positive semi-definite covariance matrix can generate negative DOF components if the instrument scan pattern is dense enough to force the use of the small eigenvalues of the a priori covariance matrix.

In our case, artificial correlations can be identified by a “bite out” in the horizontal structure of the covariance field at and below the lowest three grid scales of the model. This is demonstrated in Figure 2.2, where we have plotted the horizontal structure of the RAP-generated a priori covariances at the 8th hybrid level. Ideally this plot would demonstrate exponential behavior but, as can be clearly seen, there is an obvious departure from this behavior at small scales.

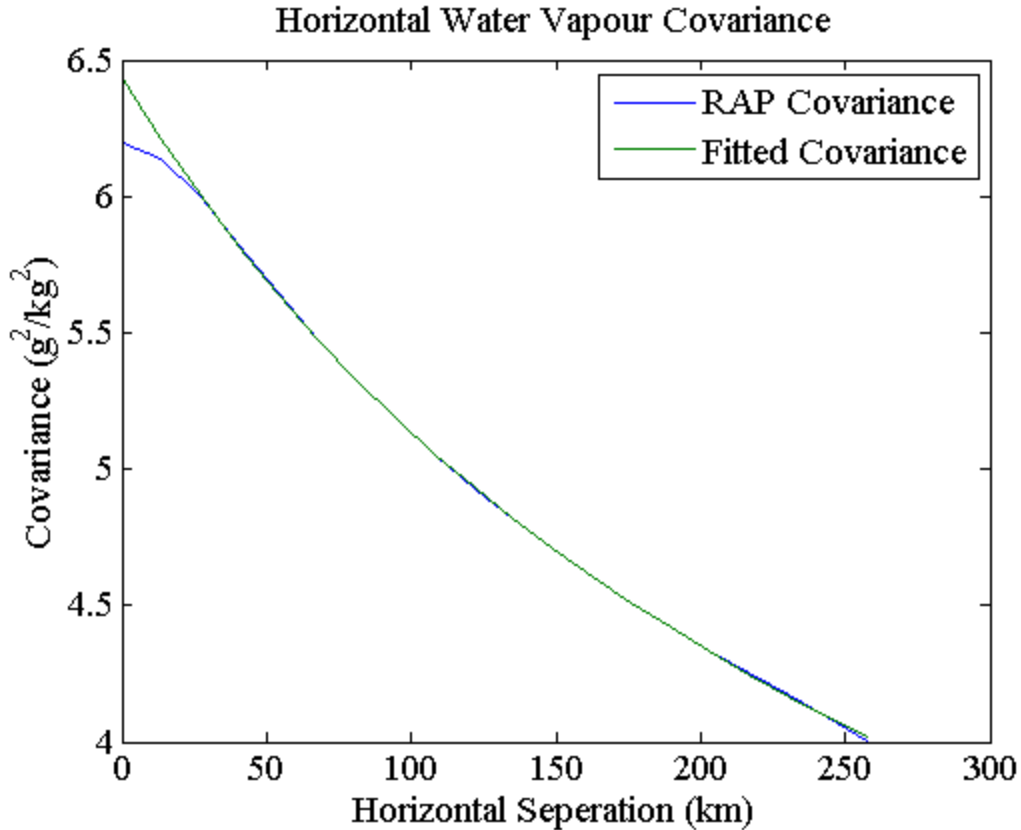


Figure 2.2 Plot of the horizontal structure of the water vapour covariances at the 8th hybrid level for July, 2011. Those generated by RAP are plotted in blue. The fitted double Gauss-Markov function is plotted in green. (Note: the difference between both curves at separations below roughly 40km).

To correct for this “bite out”, we have removed the lowest three horizontal grid scales (scales at or below 40.635 km) from the covariance field and fit the remaining horizontal structure to a double Gauss-Markov model. This fit is then used to extrapolate the covariances for scales less than or equal to 40.635 km and to extrapolate the variances. An example of this fit is presented in Figure 2.2.

For the vertical, a priori covariances are largely anisotropic and a simple method does not exist for identifying the amount of small scale smoothing within the model; as such, we have not modified the vertical structure of the RAP-generated covariance matrix. This should not be a large issue, as microwave radiometers generally provide low-resolution information in the vertical and thus

the smallest vertical scales of the a priori covariance matrix will likely not be used in our application.

2.4 Sensitivity Kernel

The last component necessary for the analysis undertaken in this study is the Sensitivity Kernel, \mathbf{K} . The sensitivity kernel is calculated using a 2D forward model presented in Meunier et al. (2012). This forward model applies the absorption model of Rosenkranz (1998) with an advanced propagation scheme, which accounts for both the earth's curvature and beam bending due to variations in the refractive index. It also accounts for both the bandwidth, assuming a square filter band, and beamwidth, assuming a Gaussian beam pattern with suppressed sidelobes. For our purposes, we have only used the bandwidth function of the forward model, so as to limit the computational requirements necessary in calculating the sensitivity kernel. Since the MMR system has a narrow beamwidth of less than 2 degrees, this assumption should have limited, if not marginal, repercussions on our results (Meunier et al., 2012).

In this study, the sensitivity kernel is estimated using a brute force secant method, where each member of the state vector is independently perturbed above and below the a priori state by 0.5K (for temperature) or 5% of the a priori (for water vapour). The brightness temperatures simulated by the forward model for both the above and below perturbations is differenced and divided by 1K (for temperature) or 10% of the a priori (for water vapour). This is done for each channel at each elevation angle.

For 3D retrieval, the process of calculating the sensitivity kernel becomes significantly more difficult. In the 2D case, we may rely on the model's internal interpolation scheme to spread perturbations to the appropriate grid. In the 3D case, one must either consider a more sophisticated forward model or create an external interpolation scheme that interpolates the gridded input water vapour, temperature, and pressure fields to a 2D cross-section appropriate for use with the 2D model and iterate the process for each azimuthal scan angle. Both of these approaches involve a significant amount of additional processing time and would be inefficient by calculating the sensitivity at all points within the domain, even those nowhere near the beam. In this study, we take a slightly different approach, calculating the sensitivity kernel at each azimuthal cross-section using the 2D forward model and distributing the outputted sensitivities rather than the input fields. This allows us to ignore the calculation of the sensitivity kernel at points nowhere near the instrument beam.

As the forward model is two-dimensional, we are forced to develop a method of using 2D cross sections to construct the 3D sensitivity kernel required for the azimuthal scanning portion of this study. For that purpose, we use the above 2D methodology to calculate the sensitivity kernel of 2D cross sections at the desired azimuths through the domain. The horizontal grid spacing of the cross section domain is chosen such that these grid points fall on each ring of points within the 3D domain. This is demonstrated in Figure 2.3.

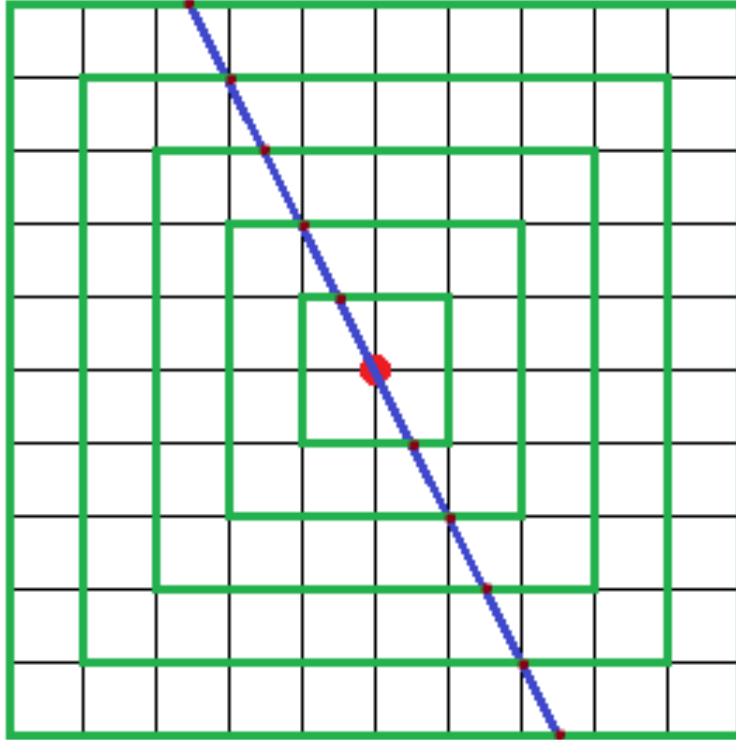


Figure 2.3 Diagram of the horizontal grid of the 3D domain with an azimuthal cross section superimposed. The grid rings are drawn in green, the azimuthal cross section is drawn in blue, the radiometer position is drawn in red, and the horizontal grid of the cross section domain is drawn in burgundy.

If the cross section points do not fall directly on the grid points of the 3D domain, the cross section sensitivities are distributed horizontally to the nearest points in that domain less than 13.545 km (one grid unit) from the cross section point. This distribution is weighted by the distance between the cross section point and the 3D domain grid points, such that the summed sensitivity is normalized to the original sensitivity of the cross section point. The sensitivity at any point within the 3D domain from a given azimuthal scan is given by the following

$$K_{3D}(x_i) = \left(1 - \frac{d_{ij}}{\delta}\right) K_{2D}(x'_j) \quad (2.10)$$

where K_{2D} is the sensitivity of state point x'_j , $d_{i,j}$ is the horizontal distance between the cross section point (x'_j) and the 3D domain point (x_i), and δ is the grid spacing of the 3D domain.

3. Results and Discussion

In this study we will evaluate the capabilities of the MMMR using the information content principles, discussed in Section 2, for four different atmospheric conditions, including a relatively wet and relatively dry environment in July, 2011 and comparable situations from January, 2012. The vertical temperature, water vapour, and pressure profiles used as a priori in this study are given in Figure 3.1.

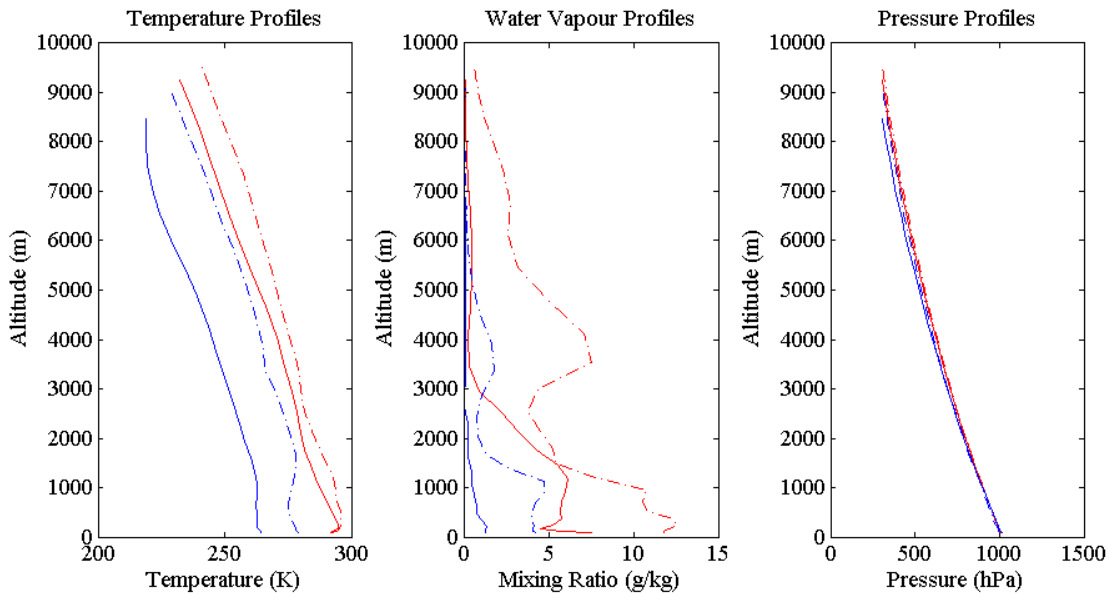


Figure 3.1 Water vapour, temperature, and pressure profiles for a relatively dry winter environment at 15 UTC on January 19th, 2012 (solid blue curves), a

relatively wet winter environment at 15 UTC on January 1st, 2012 (dashed blue curves), a relatively dry summer environment at 01 UTC on July 1st, 2011 (solid red curves), and a relatively wet summer environment at 17 UTC on July 10th, 2011 (dashed red curves).

These conditions represent the extremes of the environmental conditions such an instrument would operate in, in the Montreal area. In particular, we have chosen these conditions based on the characteristics of their moisture profiles, such that we examine the extremes of moisture conditions. As moisture is the dominant target of our instrument, these conditions should encompass the range of information retrievable from the MMR system at any given time.

In both the two- and three-dimensional runs of this procedure, we assume a horizontally homogeneous a priori environment. This allows us to simplify the three-dimensional experiment, since we need only calculate the sensitivity kernel for a single quadrant of the 3D domain and reproduce the resulting sensitivity kernel for the remaining three quadrants. Allowing for variability in the a priori environment could produce slight changes in our results, but as this is simply a proof of concept study, a horizontally homogeneous a priori environment should be sufficient for our purposes.

3.1 A Single Mesoscale Radiometer

The first experiment undertaken in this study simply looks to evaluate the capabilities of a single MMR operating at the center of the aforementioned domain. This assessment is undertaken for two modes of operation: 2D elevation scanning and 3D elevation and azimuthal scanning.

3.1.1 2D Elevation Scanning

For the 2D elevation scanning experiment, we assume the relatively simple scanning pattern plotted in Figure 3.2, where the minimum scanning angle is limited to one degree in elevation so as to avoid ground contributions to the measurement signal due to the beamwidth of the instrument.

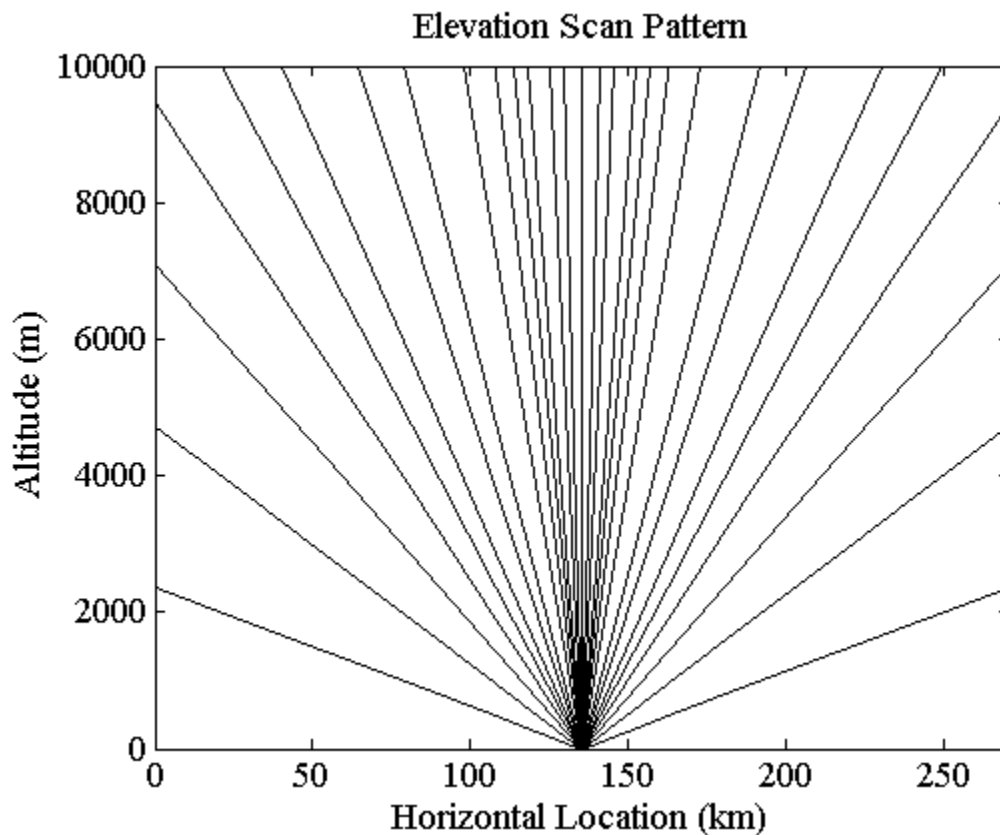


Figure 3.2 Plot of the elevation scan pattern used in this study. Note: This is a simple plot of the scan geometry and thereby does not account for ray bending due to gradients in the refractive index or for the curvature of the Earth. These are, however, accounted for in the forward model.

Using the framework discussed in Section 2, we have calculated the total number of DOFs retrieved by the radiometer under the four atmospheric conditions of Figure 3.1, as well as the individual contributions to the total DOFs

from all locations within the state vector. Contour plots of the distribution of DOFs for temperature, in all four environments, are presented in Figure 3.3 and, for water vapour, in Figure 3.4. The total DOFs for all four cases are presented within the titles of Figures 3.3 and 3.4.

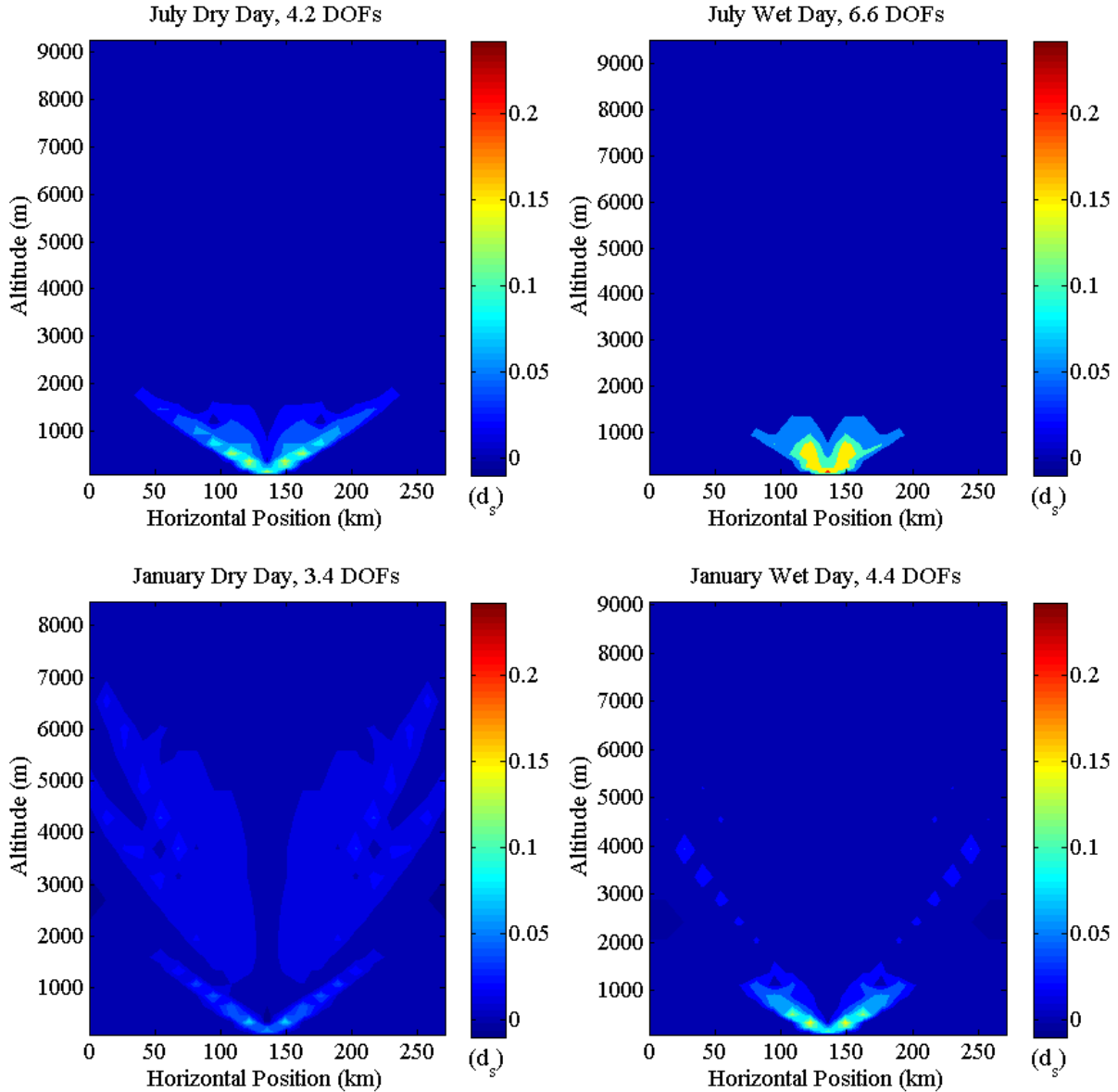


Figure 3.3 Contours of the temperature DOFs for July (top) and January (bottom) wet (right) and dry (left) cases.

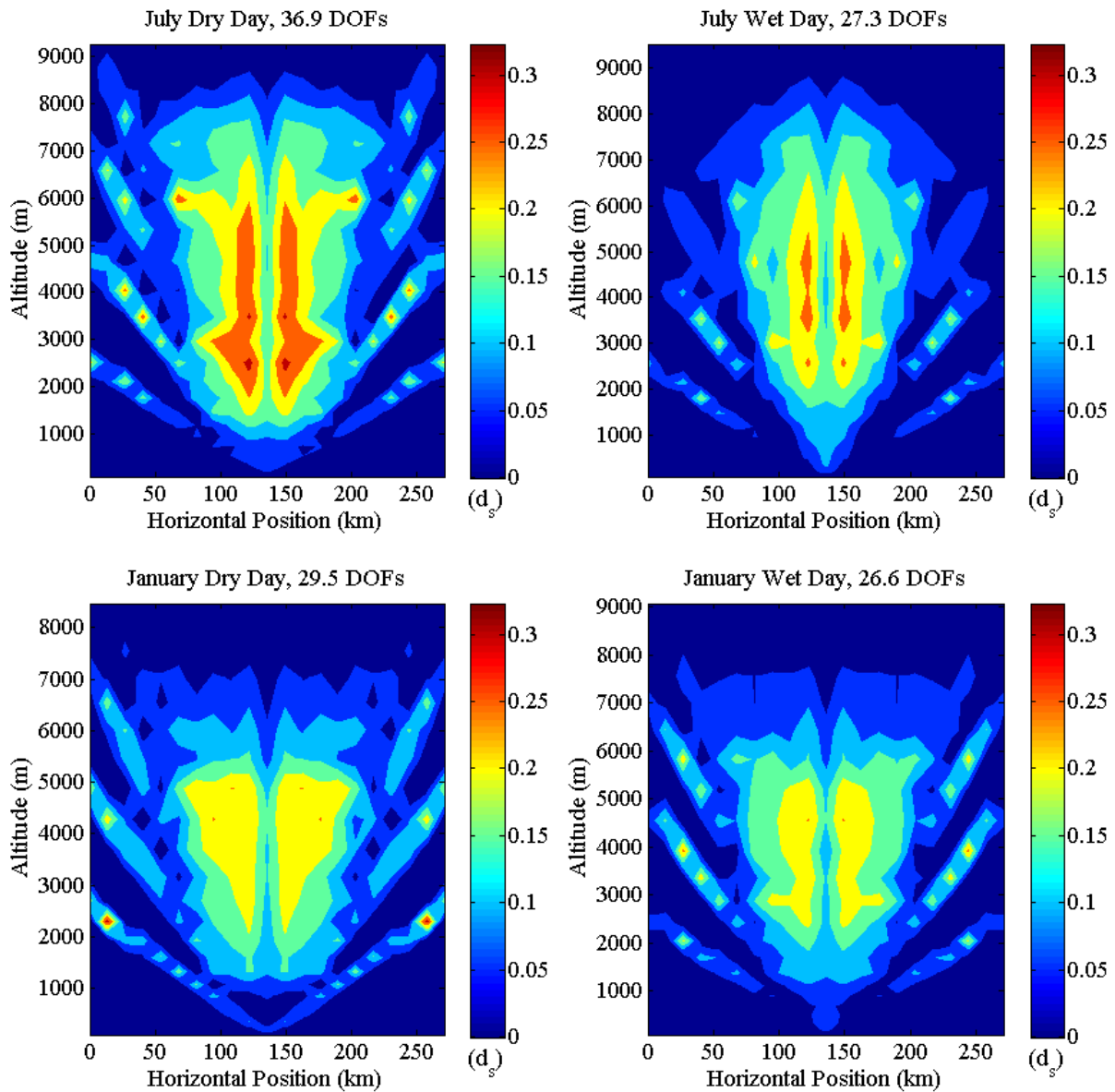


Figure 3.4 Contours of the water vapour DOFs for July (top) and January (bottom) wet (right) and dry (left) cases.

The first, and most notable, feature of these Figures is the presence of appreciable information retrievable at large distances from the radiometer (more than 130 km away for water vapour). This is particularly striking as there have been no studies that have examined the capability of a radiometer over such a

large horizontal domain and thus the prospect of retrieving information at such scales has remained largely unfathomed.

From Figure 3.4, it would appear as if the majority of the retrieved information is retrieved from above roughly 1000 meters altitude with little information retrieved near the instrument. This, however, is a deception caused by our choice of vertical coordinate. The use of a hybrid vertical coordinate in our retrieval framework results in fairly dense vertical levels near the surface (roughly 10 of the 25 vertical levels of our domain are within the first 1000m of the atmosphere). Since there is an abundance of grids near the surface, the retrieved DOFs will tend to spread over the many closely spaced grids. To overcome this illusion of less information near the instrument and get a better idea of the proper distribution of the information retrieved, we need only consider the DOFs per unit area; thereby, removing the grid size dependence of the DOF distribution. Contours of the DOF density for water vapour for our four cases are presented in Figure 3.5. We do not present the DOF density for temperature as the temperature information at the receiver is nearly singular in comparison with that from elsewhere in the field.

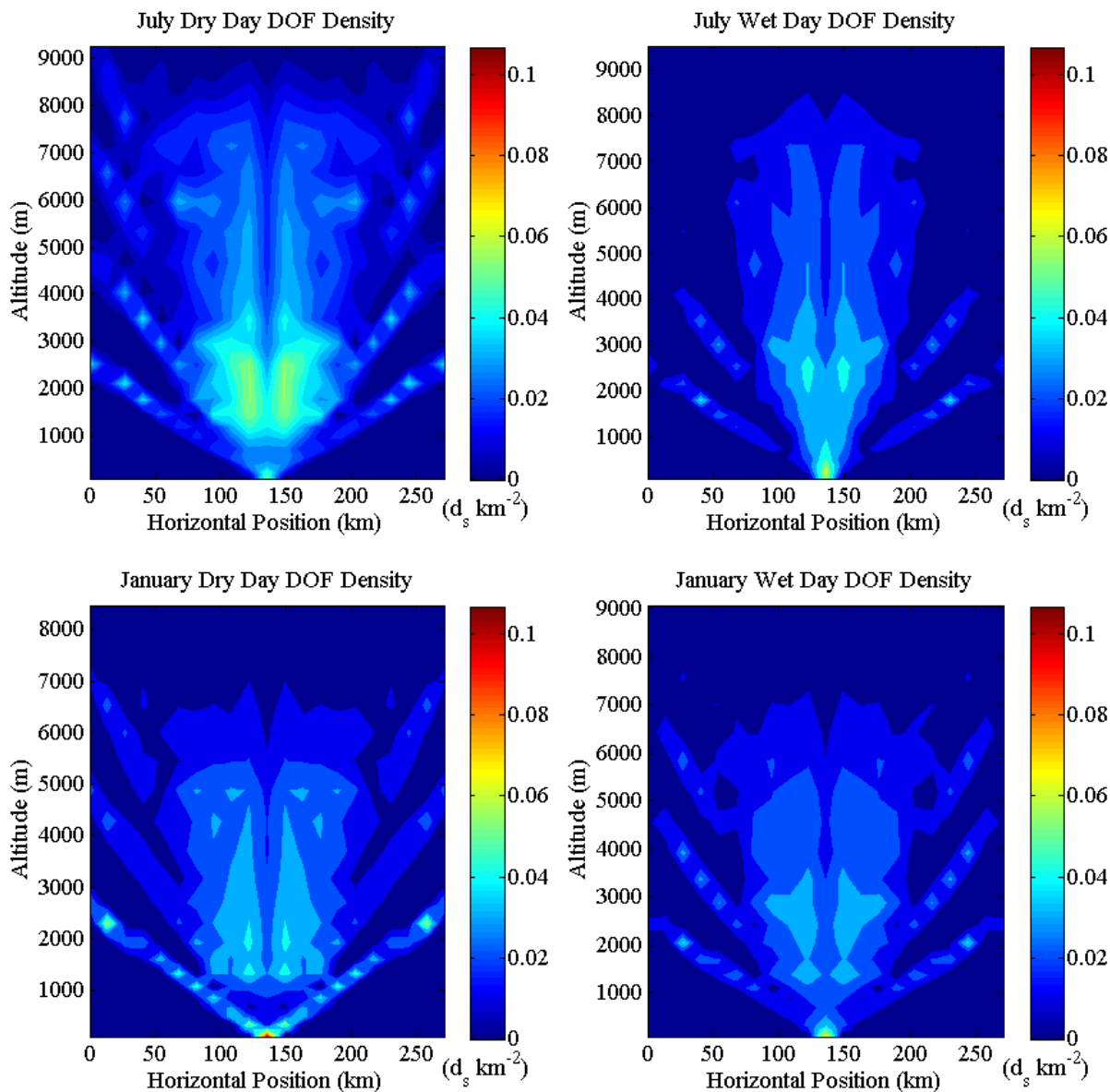


Figure 3.5 Contours of the water vapour DOF density for July (top) and January (bottom) wet (right) and dry (left) cases.

As one may notice, water vapour information is still greatest above 1000m altitude, but a second maximum in information at and near the instrument is now evident. This makes sense, as the instrument is located at the intersecting point of all of the ray paths and thus should be the strongest constrained point within the field.

Overall, we observe between 26.5 and 37.0 DOFs for water vapour and between 3.3 and 6.6 DOFs for temperature. This is striking, as previous implementations of radiometers for vertical profiling have demonstrated only ~2-3 DOFs for water vapour (Löhnert et al., 2009). Looking at the vertical sum of DOFs for all four cases presented in Figure 3.6, it is clear that our method actually retrieves well in excess of 2 DOFs in the vertical at each horizontal grid within ~60 km of the instrument and between 1 and 2 DOFs outside of that range, where we observe a peak of roughly 4 DOFs approximately 25km from the instrument.

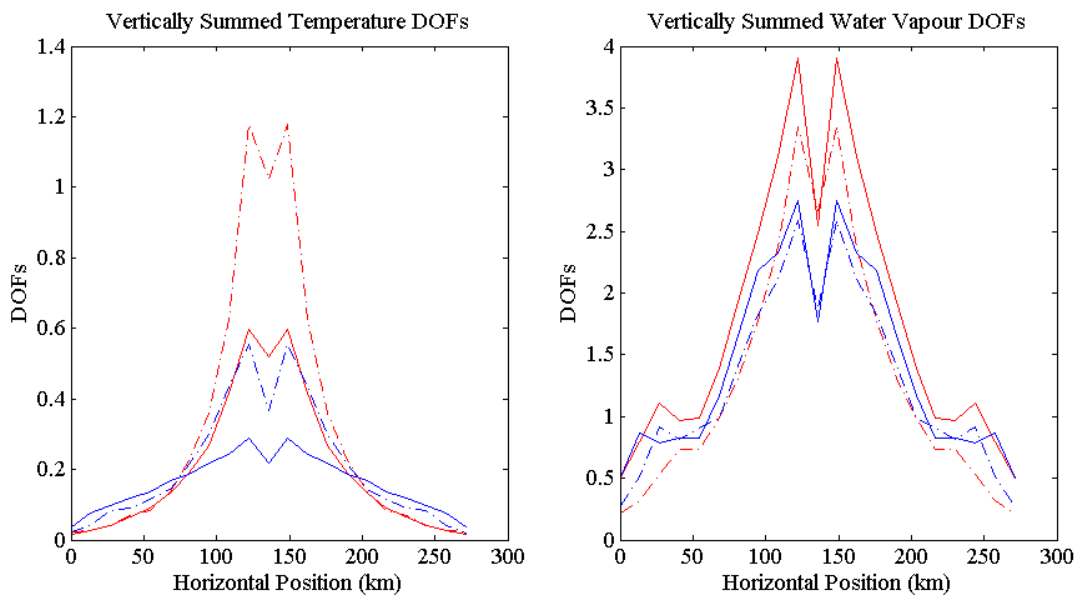


Figure 3.6 Vertically summed water vapour and temperature DOFs for the dry January (solid blue curves), wet January (dashed blue curves), dry July (solid red curves), and wet July (dashed red curves) experiments.

These observations all, of course, assume our relatively simple scan pattern; with the use of a more sophisticated or efficient scan pattern, it may even be possible to extend the region of greater than 2 water vapour DOFs to further than 60 km from the instrument.

In general, a retrieval process attempts to constrain the a priori variability, presented in Figure 3.7, such that the expected retrieval error is minimized.

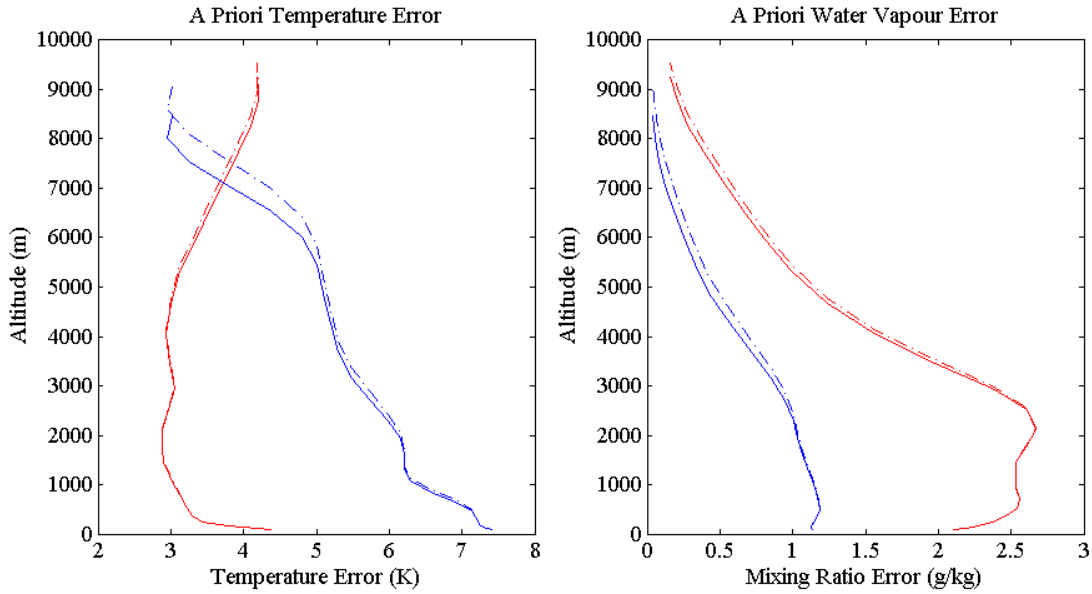


Figure 3.7 Water vapour and temperature a priori standard deviations for the dry January (solid blue curves), wet January (dashed blue curves), dry July (solid red curves), and wet July (dashed red curves) experiments. (NOTE: There is a slight spread in the standard deviations within each month since this plot is in height coordinates and our covariance matrix was calculated in hybrid coordinates).

We may take the expected retrieval error as the square root of the diagonal entries of the retrieval covariance matrix given by (2.6). The expected retrieval errors from all four cases are presented in Figures 3.8 and 3.9.

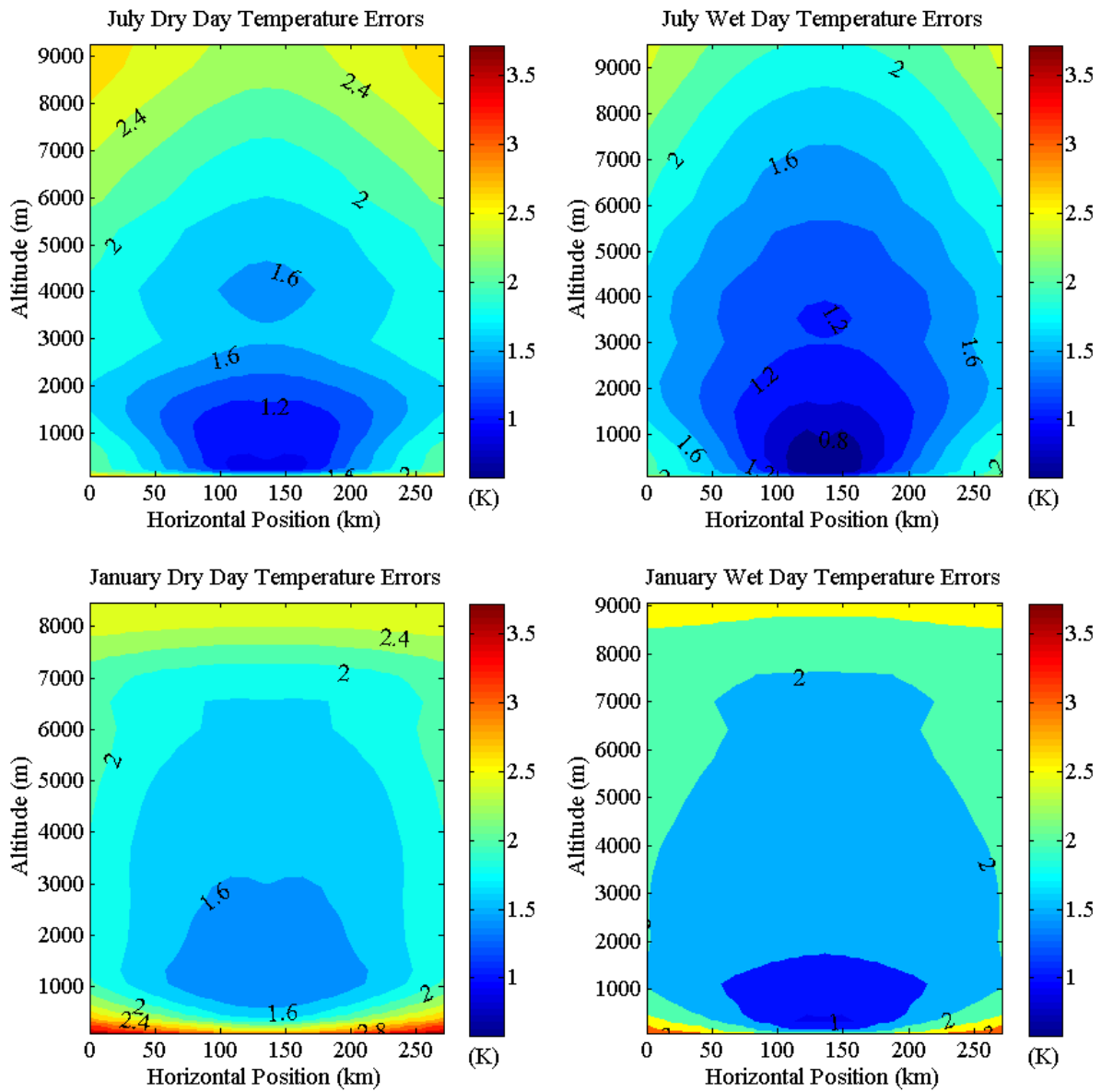


Figure 3.8 Contours of the expected temperature retrieval errors for July (top) and January (bottom) wet (right) and dry (left) cases.

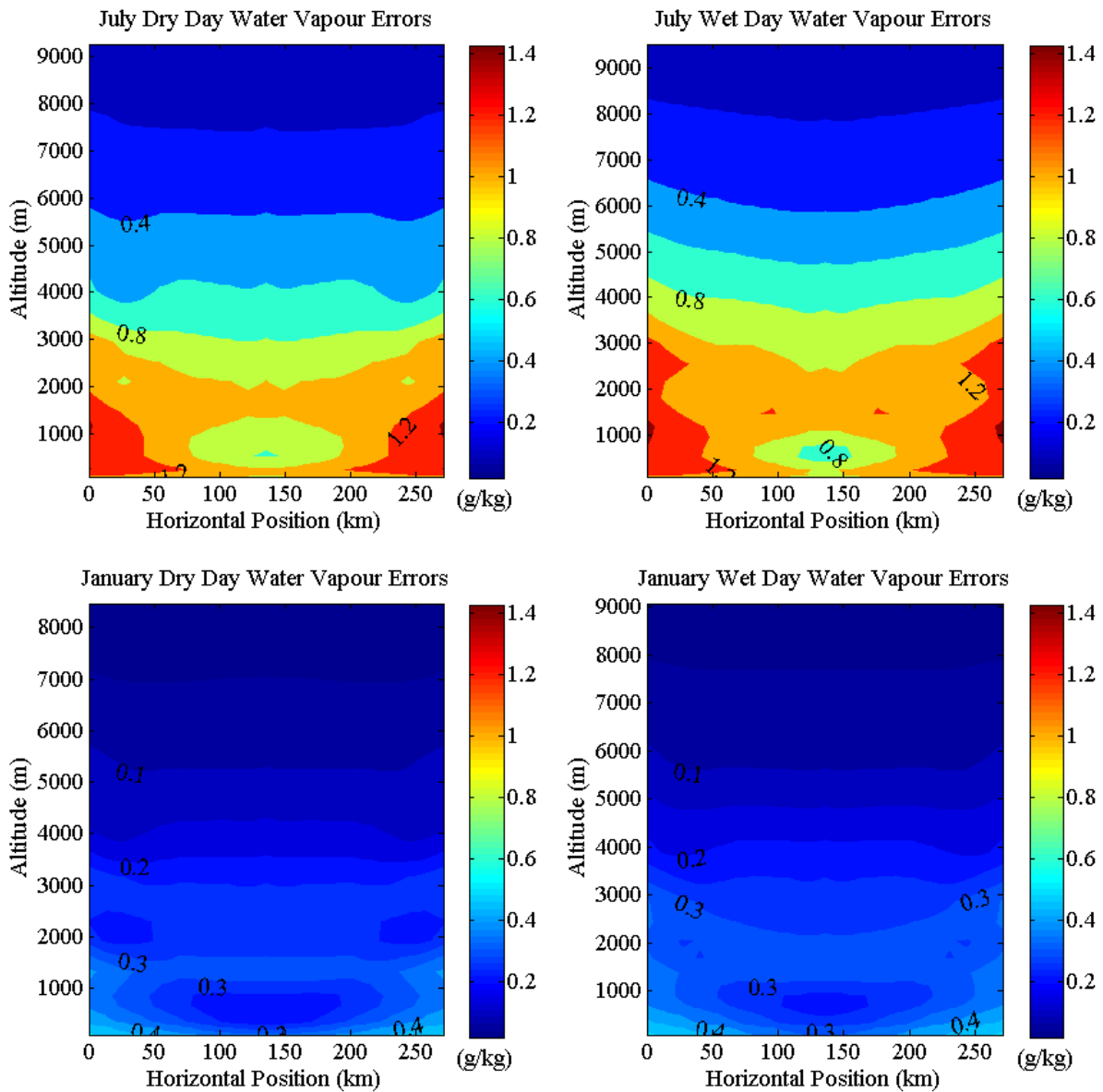


Figure 3.9 Contours of the expected water vapour retrieval errors for July (top) and January (bottom) wet (right) and dry (left) cases.

In general, a single radiometer appears to be capable of constraining water vapour to greater than 1.4g/kg accuracy during summer periods and greater than 0.45 g/kg accuracy during winter periods throughout the atmosphere at up to 140 km range. Greater accuracies during the winter experiments can be largely attributed to the decreased a priori variability of water vapour during that period.

Accuracies greater than 1 g/kg, during summer periods and within 0.25 g/kg during winter periods, can be found within the boundary layer within roughly 50 km of the instrument.

For temperature, the results are far less encouraging, where we have little to no constraint on temperature above 1000 meters or beyond 50 km from the instrument. This results in temperature retrieval accuracies of no better than ~ 0.8 K during even the wettest periods of July and no better than ~ 1 K during even the wettest periods of January. This is, however, a stronger constraint than we had initially anticipated, as these frequencies are not typically used for temperature retrieval.

There are several interesting, qualitative features present in Figures 3.3 through 3.6 that should be discussed before proceeding to three dimensional scanning, the first of which is the local minimum of information available from directly above the instrument evident in Figure 3.6. This feature is fairly simple to explain: the vertical beam is the one that travels through the least amount of water vapour; thus, low-opacity channels, used at vertical, contribute little information to the retrieval. Off-vertical beams, however, rapidly begin to intersect several times more water vapour than the pure-vertical path; thus, low-opacity channels begin to contribute significant information to the retrieval along these paths.

Comparing the results from both months, one may notice a general decrease in both the water vapour and temperature DOFs from July to January. These results are, essentially, as expected. Looking at temperature, the temperature weighting functions are highly dependent on the amount of water

vapour available within the system: as water vapour increases, the linear independence of the temperature weighting functions also increases, increasing the amount of information that can be retrieved by the instrument. For water vapour, there appears to be a general trend of increasing DOFs with decreasing water vapour. In this case, as water vapour increases, the regions of maximum sensitivity for each channel begin to crowd together, closer to the instrument, causing a loss in information as correlations within the field begin to remove what used to be spatially uncorrelated information. In Figure 3.10 we present the difference in the expected water vapour retrieval error fields between the wet and dry experiments of July, 2011.

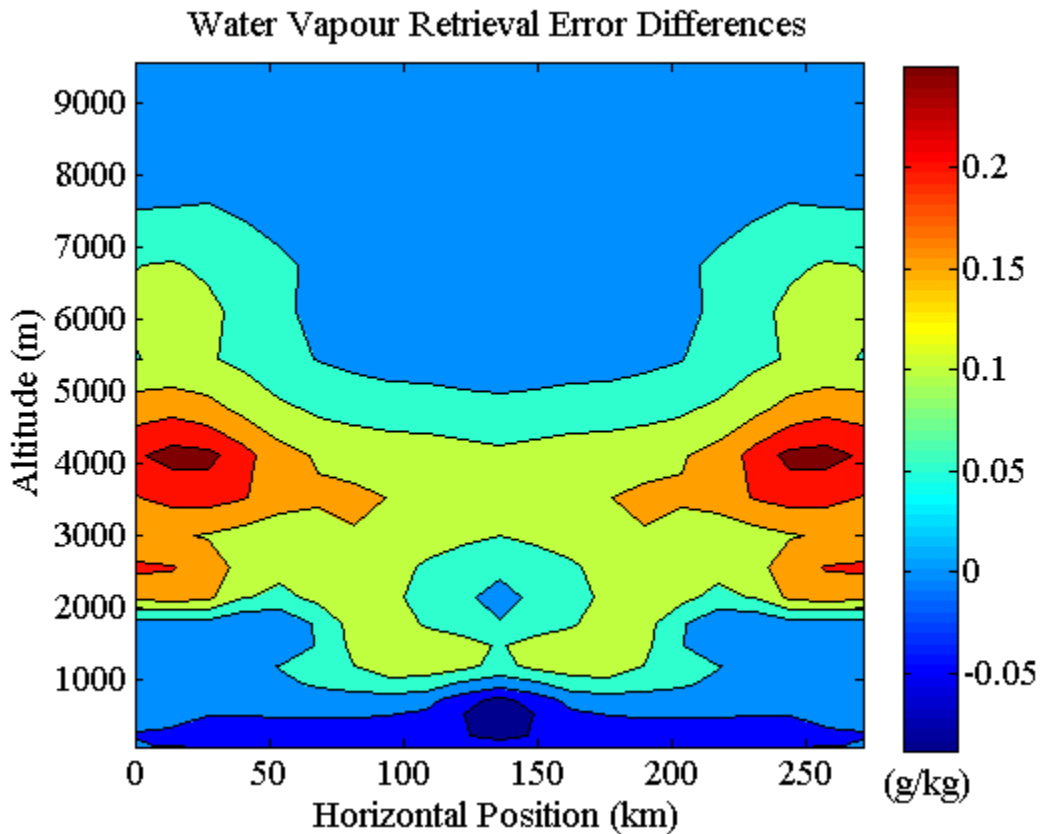


Figure 3.10 Contour of the difference between expected retrieval errors of the wet and dry summer experiments ($\sigma_{wet} - \sigma_{dry}$).

As can be clearly seen, as water vapour increases, we retrieve a stronger constraint on water vapour near the instrument but at the cost of a much weaker constraint further away from the instrument. Considering the observations between seasons, we find that the above factors cannot be the only factors affecting the DOFs retrieved by the instrument, as there is a clear difference in the retrieved DOFs between the wet winter and dry summer cases. We must thereby consider the amount of information available in the system a priori.

Temperature variability is larger in January than it is in July and water vapour variability is larger in July than it is in January, as is evident in Figure 3.7. While there is more temperature information available to be retrieved in January than in July, there is significantly less water vapour available during this period; thus, these two mechanisms roughly balance out, except during the wettest periods of July, where we observe appreciably more temperature DOFs than during other periods of the year. For water vapour, there is more information available to be retrieved in July than in January but there is far more water vapour in July as well; thus, we find comparable water vapour DOFs during the wet July experiment as during the January experiments but significantly more DOFs during the relatively dry July experiment.

Overall, these results are very encouraging and demonstrate that a microwave radiometer can, in fact, provide appreciable water vapour information at distances of over 100km. The question now is “how will these results translate as we undertake full three-dimensional scanning” and “what amount of azimuthal scanning will provide useful information for three-dimensional retrieval”?

3.1.2 3D Elevation and Azimuthal Scanning

Expanding on the 2D experiment, we proceed to consider a three dimensional retrieval that incorporates azimuthal scanning. For that purpose, we undertake a single experiment for the dry July case, where we have reduced the number of experiments due to the computational and time requirements of the three dimensional retrieval.

In this experiment, an MMR system is placed at the center of a 270.9 x 270.9 km domain (i.e. a 3D version of the 2D domain used previously). We maintain the same elevation scanning pattern as was used in the 2D experiments, while trying various azimuthal scan patterns, and attempt to identify the benefit of increasing the density of azimuthal scans. In Figures 3.11 and 3.12, we present the calculated water vapour and temperature DOFs along East-West cross-sections through the 3D domain using azimuthal scans separated by five degrees. The header of each subplot identifies the North-South distance of the cross-sections from the edge of the domain, where the cross section going through the instrument is located at 135.45km.

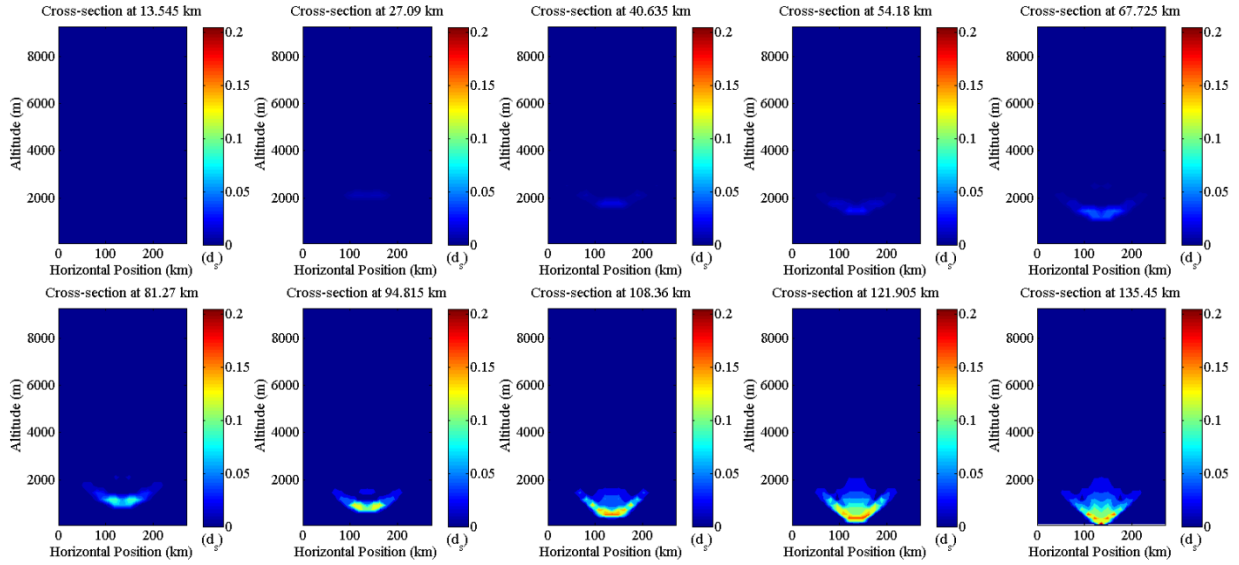


Figure 3.11 Contours of the distribution of temperature DOFs for July (top) and January (bottom) wet (right) and dry (left) cases. Contours are plotted at various East-West cross-sections at a North-South position identified in the subplot header.

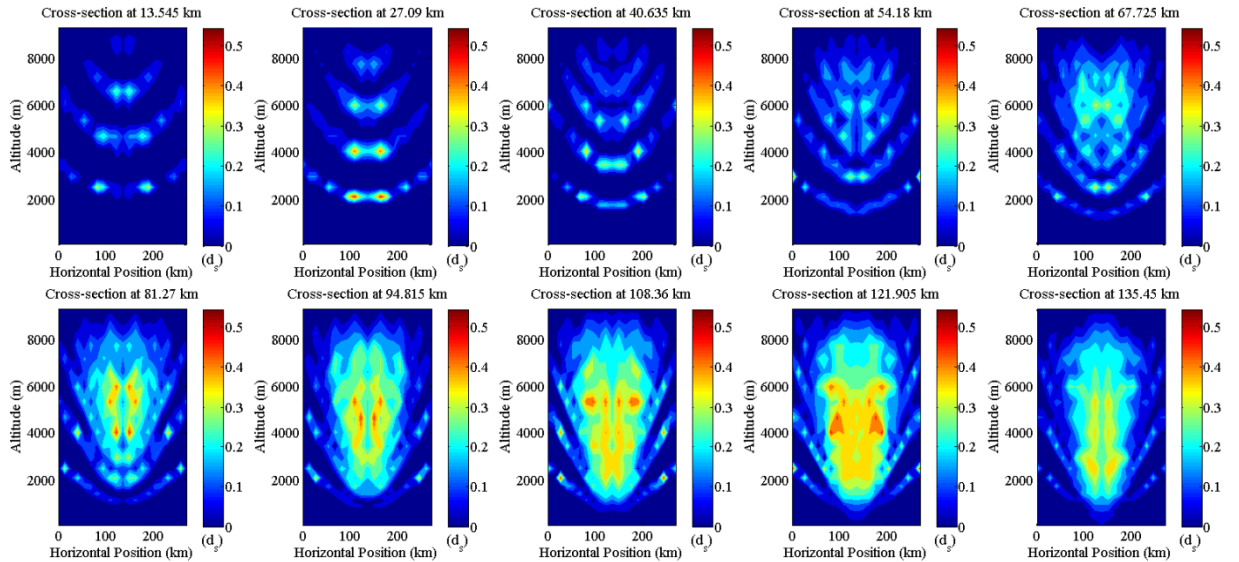


Figure 3.12 Contours of the distribution of water vapour DOFs for July (top) and January (bottom) wet (right) and dry (left) cases. Contours are plotted at various East-West cross-sections at a North-South position identified in the subplot header.

These plots are all consistent with the associated 2D experiment results presented in the previous section.

While this type of representation gives a good indication of the vertical structure of the information retrievable by the instrument and is useful for comparisons with our 2D experiments, it is sometimes difficult to infer the horizontal structure of this information from these representations; as such, we present contours of the vertically summed water vapour and temperature DOFs at each horizontal element of the domain in Figures 3.13 and 3.14.

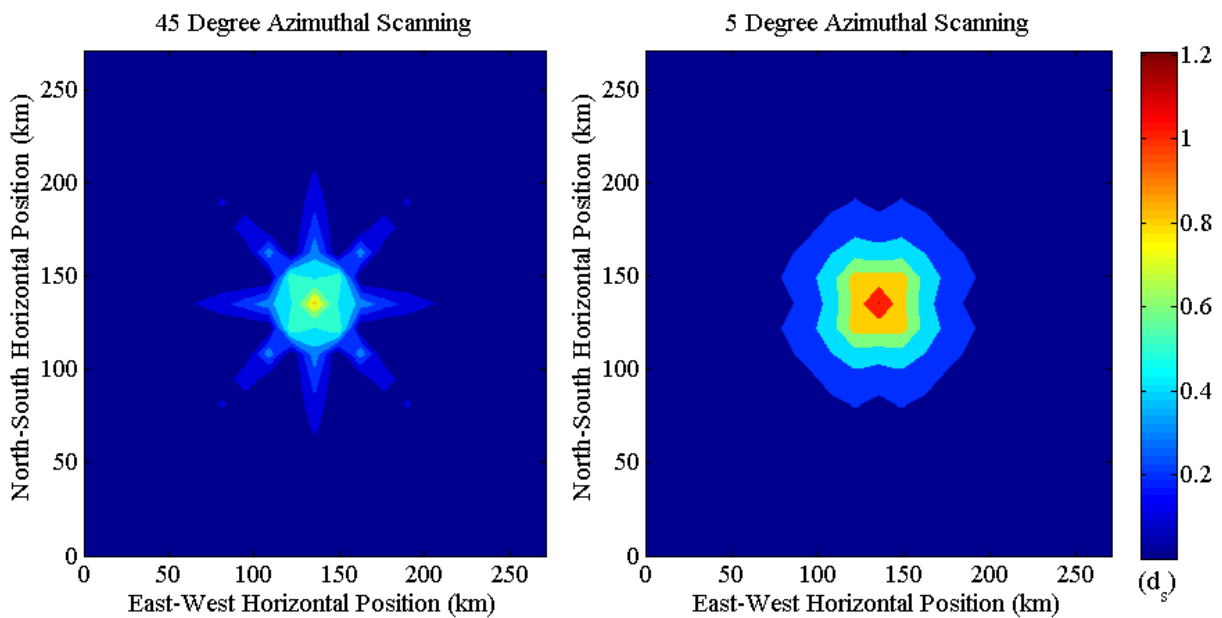


Figure 3.13 Vertically-summed temperature DOFs at each horizontal position within the specified domain. The density of azimuthal scans used in each case is presented in the header of each subplot.

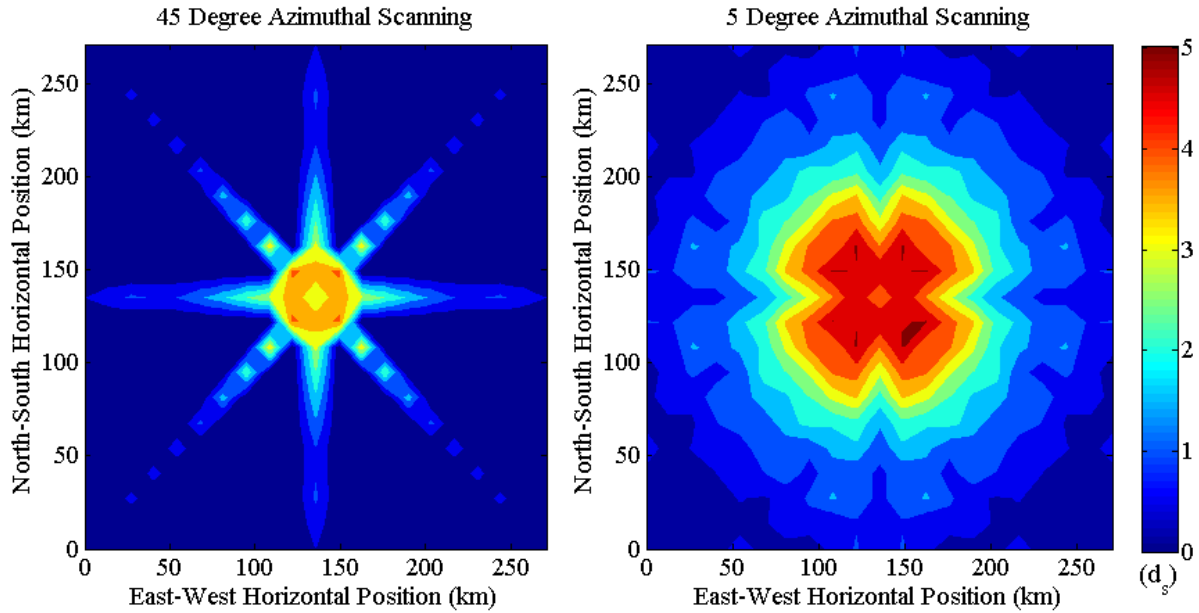


Figure 3.14 Vertically-summed water vapour DOFs at each horizontal position within the specified domain. The density of azimuthal scans used in each case is presented in the header of each subplot.

These contours can be compared to those of the 2D dry July experiment presented in Figure 3.6. As can be seen there is a considerable increase in the vertically summed water vapour and temperature DOFs achieved through the incorporation of azimuthal scanning.

We may also look at the expected retrieval errors associated with the five degree azimuthal scanning experiment. These retrieval errors, represented in a similar manner as Figures 3.11 and 3.12, are presented in Figures 3.15 and 3.16.

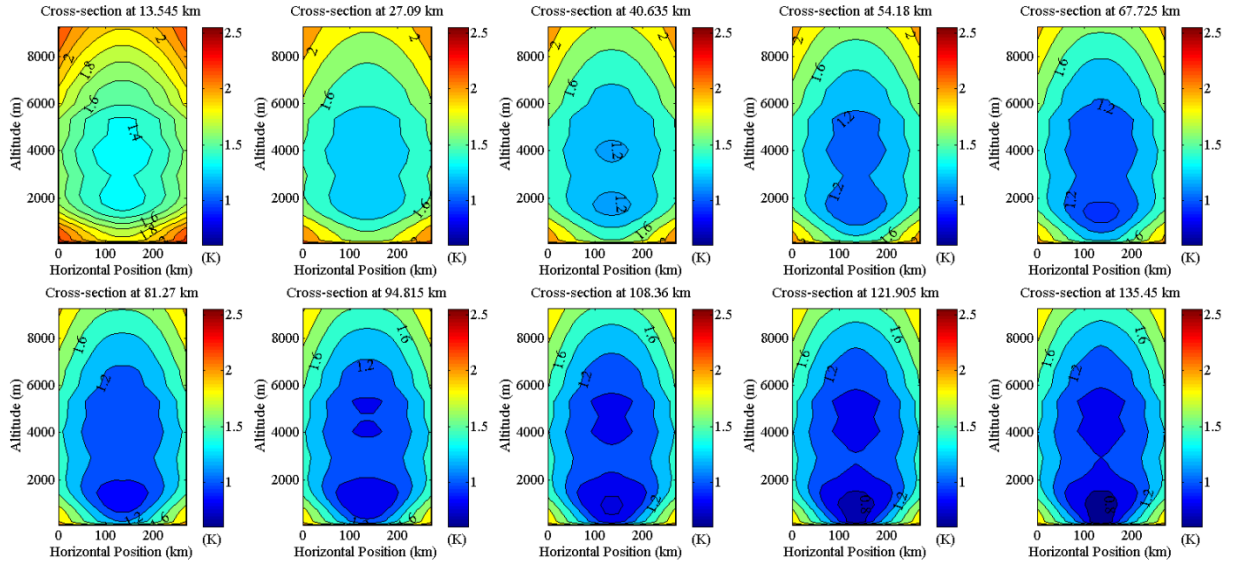


Figure 3.15 Contours of the distribution of expected temperature retrieval errors for July (top) and January (bottom) wet (right) and dry (left) cases. Contours are plotted at various East-West cross-sections at a North-South position identified in the subplot header.

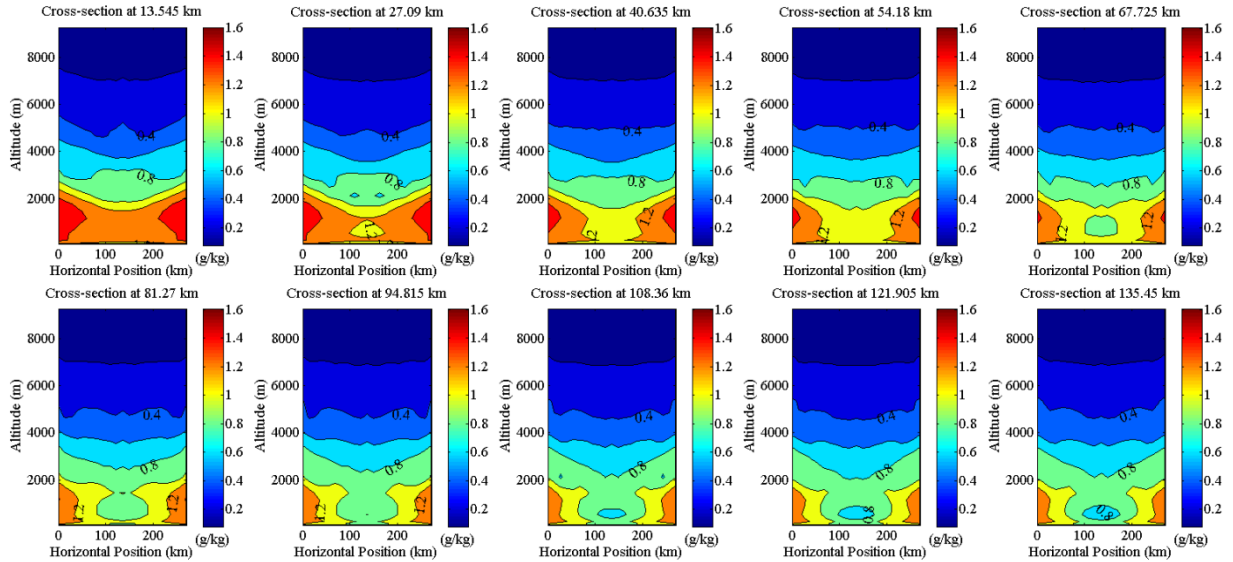


Figure 3.16 Contours of the distribution of expected water vapour retrieval errors for July (top) and January (bottom) wet (right) and dry (left) cases. Contours are plotted at various East-West cross-sections at a North-South position identified in the subplot header.

Comparing the 135.45km cross-section (i.e. the cross-section through the instrument) retrieval errors to those of the 2D elevation scanning experiment, we note that there is an appreciable benefit to azimuthal scanning outside of the

simple coverage benefits one would expect, where nearby azimuthal scans have helped constrain the water vapour and temperature retrieval errors of the cross section through the instrument. This is expected, given the comparison of Figures 3.13 and 3.14 to Figure 3.6, mentioned previously.

It is also of interest to assess the benefit of increasing azimuthal scan density. In Table 3.1 we present the total water vapour and temperature DOFs retrieved from this system using various azimuthal scan densities.

Table 3.1 *DOFs for various azimuthal scan patterns*

Azimuthal Scan Spacing	Water Vapour DOFs	Temperature DOFs
45°	133.28	12.85
20°	258.14	20.09
15°	326.52	24.01
10°	419.75	26.82
5°	617.97	34.78

As can be seen, there is a significant increase in water vapour and temperature DOFs with increasing azimuthal scan density. Even at five degree separation, there is still an appreciable increase in the amount of water vapour information associated with the addition of further azimuthal scans. This increase is less significant for temperature, as temperature information tends to come from close to the instrument, where the distance between elements of each azimuthal scan is quite small and the information of each scan is thus highly correlated in the horizontal. We were unable to undertake azimuthal scanning at smaller than 5 degree intervals due to the limitations of our a priori covariance matrix and to computational limitations.

These results combined with the results of the 2D experiments of the previous section clearly demonstrate the significant coverage and information content benefits of undertaking scanning with a microwave radiometer. There are, however, caveats to the use of these instruments in scanning conformation: these results clearly show a lack of skill of these instruments for temperature profiling and, while the MMMR system can provide an appreciable constraint on temperature, this is only a slight added benefit compared to the much more significant capability for profiling water vapour. Also, the beamwidth of these instruments and the potential for ground contamination significantly limits their ability to retrieve information in the lower boundary layer, where, even scanning at an ambitious one degree elevation leaves us with no ray paths below 2.5km altitude at the edge of the retrieval domain. The latter limitation could possibly be addressed through deploying these instruments at radar sites, where the use of radar refractivity measurements could constrain water vapour at lower elevations. Methods for overcoming the former limitation are discussed in Section 3.2.1.

3.2 The More the Merrier

The ultimate goal of this study is to evaluate the capabilities of the MMMR for meeting the criteria of Weckwerth et al. (1999); namely, we strive to assess the capabilities of such an instrument in a network conformation. For this purpose, we have undertaken a few simple experiments where multiple instruments have been included. Prior to that, however, we first look at the potential benefit of adding a V-band radiometer to the system.

3.2.1 The Addition of a V-Band Radiometer

As can be seen in Section 3.1 a K-band microwave radiometer is severely lacking in its ability to profile temperature, particularly at altitudes above 1000 meters. A V-band radiometer is designed to operate within the 60GHz Oxygen complex frequency range. Since Oxygen is a well-mixed gas and the 60GHz Oxygen complex is a strong band, a V-band instrument is largely sensitive to temperature. In this experiment, we attempt to assess the potential benefit of adding a V-band radiometer to the existing MMR system.

This is done by simply adding a set of V-Band radiometer channels to the initial measurement vector following the specifications of a typical V-Band system. The system chosen for this study is the Radiometrics MP-3000 V-Band radiometer with channels chosen as 51.250, 52.280, 53.855, 54.955, 56.660, 57.290, and 58.800 GHz, following the work of Hewison and Gaffard (2003). The specifications used for the instrument are as given in Table 1.2 and Liljegren (2002).

The results of implementing this procedure are presented in Figures 3.17 and 3.18, where we have plotted contours of the temperature DOFs and expected retrieval errors for all four experiments.

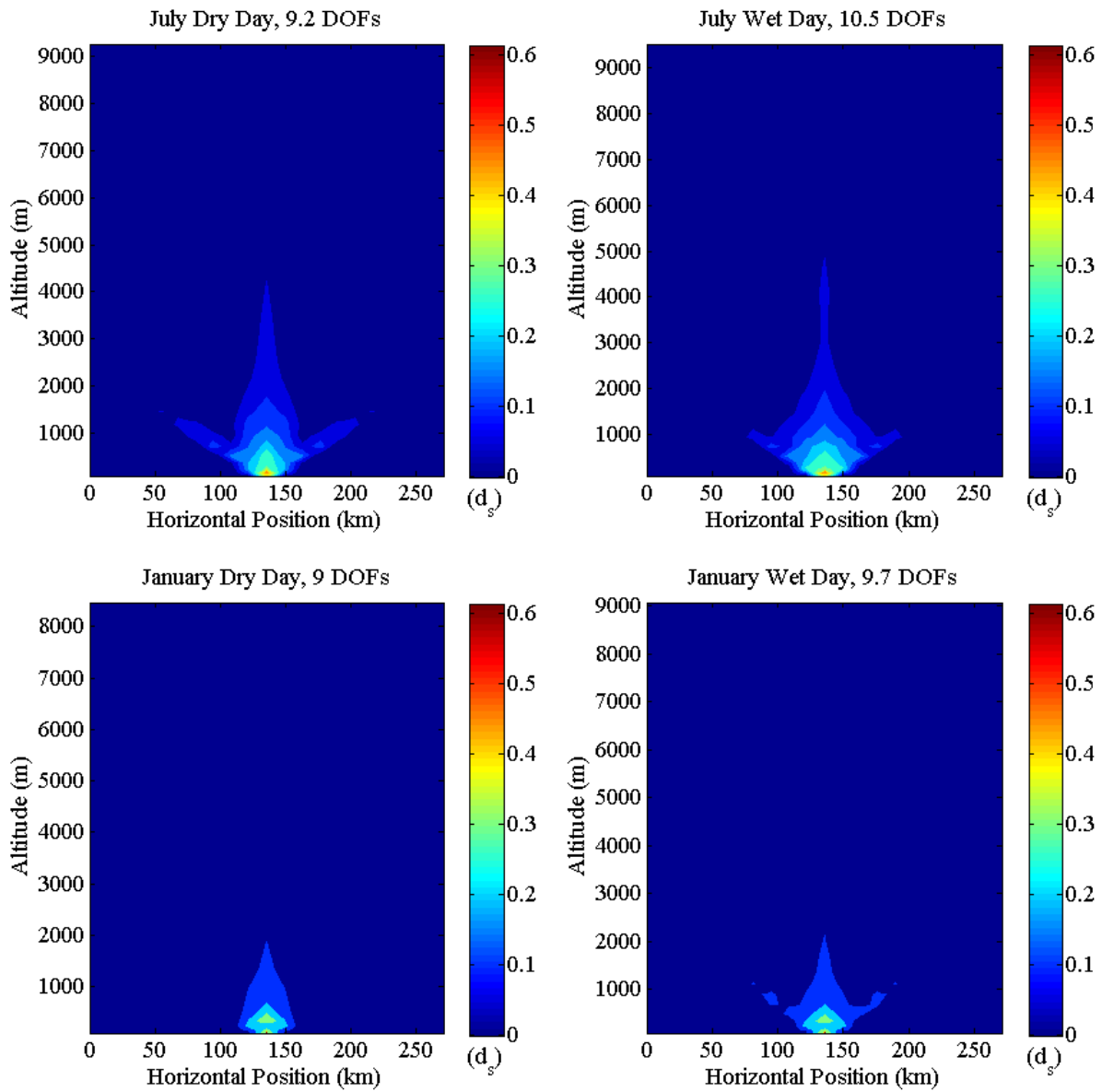


Figure 3.17 Contours of the temperature DOFs for July (top) and January (bottom) wet (right) and dry (left) cases using both a K- and V-Band radiometer.

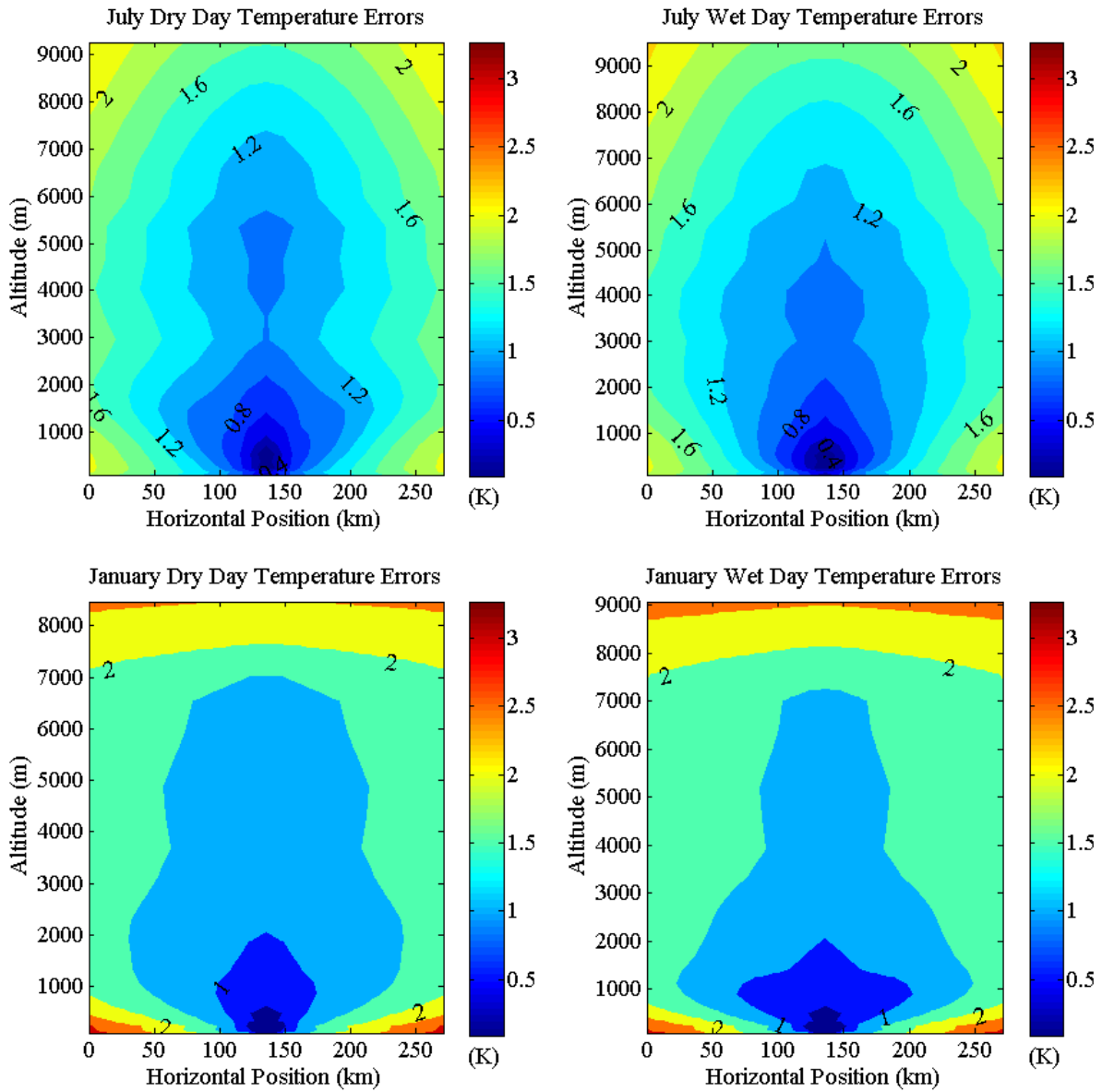


Figure 3.18 Contours of the expected temperature retrieval errors for July (top) and January (bottom) wet (right) and dry (left) cases using both a K- and V-band radiometer.

We have neglected to plot the water vapour DOFs and expected retrieval errors in this manner due to the largely insignificant information contributed to the water vapour retrieval by the added V-band channels; nonetheless, we have plotted the vertically summed DOFs for both water vapour and temperature in Figure 3.19.

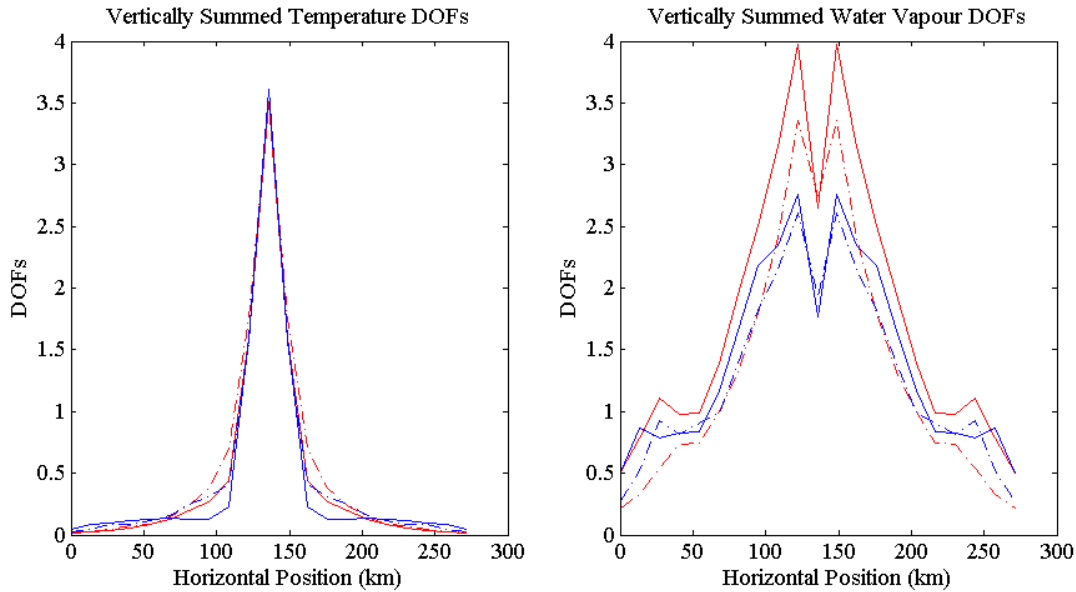


Figure 3.19 Vertically-summed temperature and water vapour DOFs at each horizontal position within the specified domain using both a K- and V-band radiometer.

With the addition of the V-Band radiometer, we achieve both a stronger and better distributed temperature constraint from the instrument, where temperature errors have been reduced significantly in the region closest to the instrument and in the column directly above the radiometer. For the wet July experiment errors of less than 1K are achieved up to 50km from the instrument and up to altitudes of ~ 4000 meters, while for the dry winter experiment, 1K errors are limited to distances within 25km of the instrument and only up to altitudes of 2000 meters. In terms of DOFs, these results are consistent with the previously observed trends, where more water vapour has translated into more temperature information retrieved by the instrument.

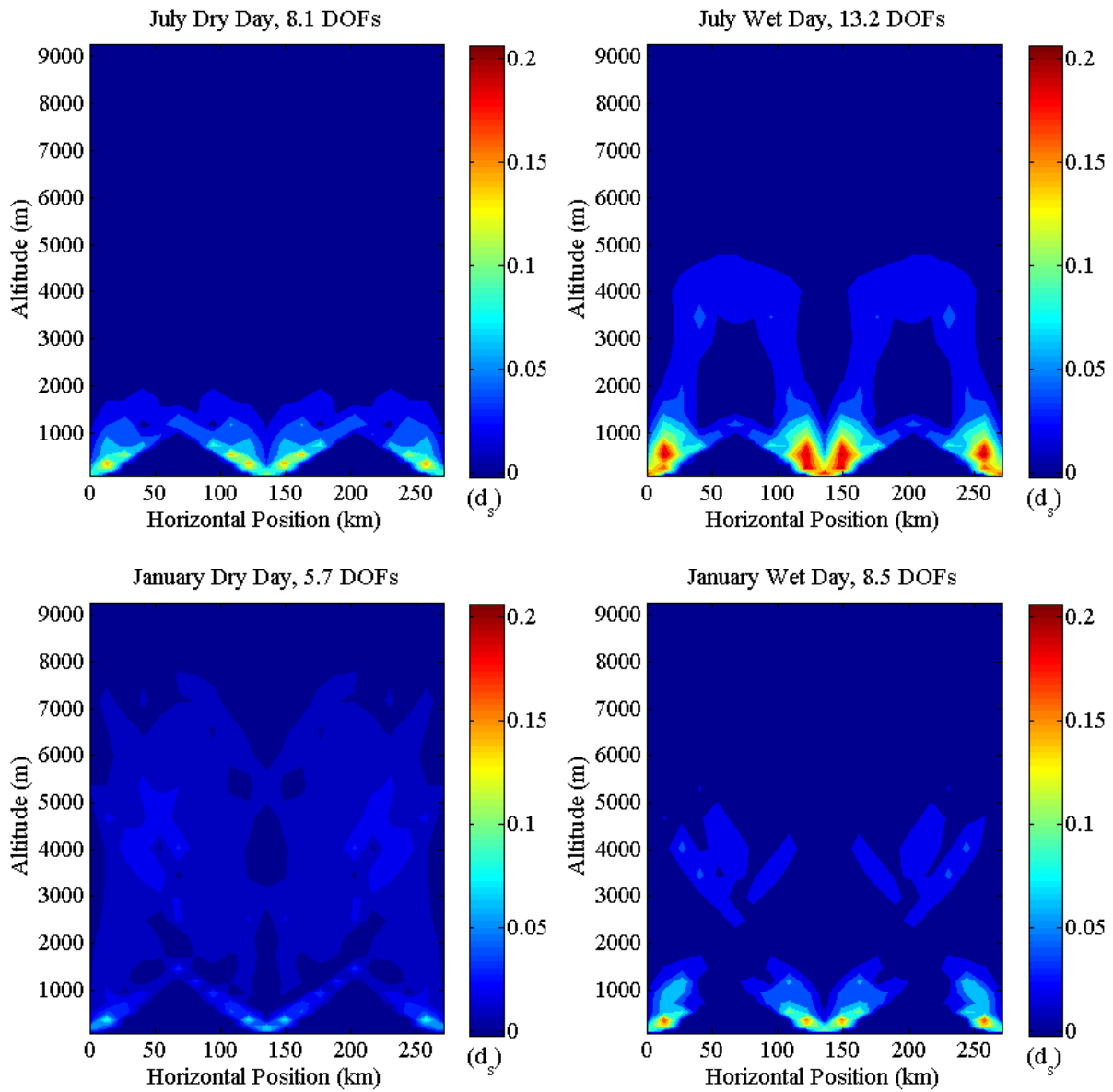
These results for temperature, while a marked improvement on those with the MMR system alone, are still not sufficient for most practical applications, lacking in coverage at appropriate accuracies; however, with the addition of more

of these instruments to the retrieval domain, it may be possible to extend the coverage of acceptable information to a more useful range.

3.2.2 Multiple Mesoscale Radiometers

To examine the capabilities of the MMMR system for retrieval within a network of instruments, we conduct a simple experiment, where we have placed three MMMR instruments within the retrieval domain: one at the center of the domain scanning 180 degrees in elevation and the other two instruments at the boundaries of the domain scanning inwards. The purpose of this experiment is to examine the effect of instrument coverage on the amount of information retrievable from the system in a network application, as well as to investigate the benefit, if any, of ray intersects on the information content of these measurements.

For this purpose, we have plotted contours of the water vapour and temperature DOF distribution retrieved for all four environments used in Section 3.1 in Figures 3.20 and 3.21.



Figures 3.20 Contours of the temperature DOFs for July (top) and January (bottom) wet (right) and dry (left) cases using three MMR systems.

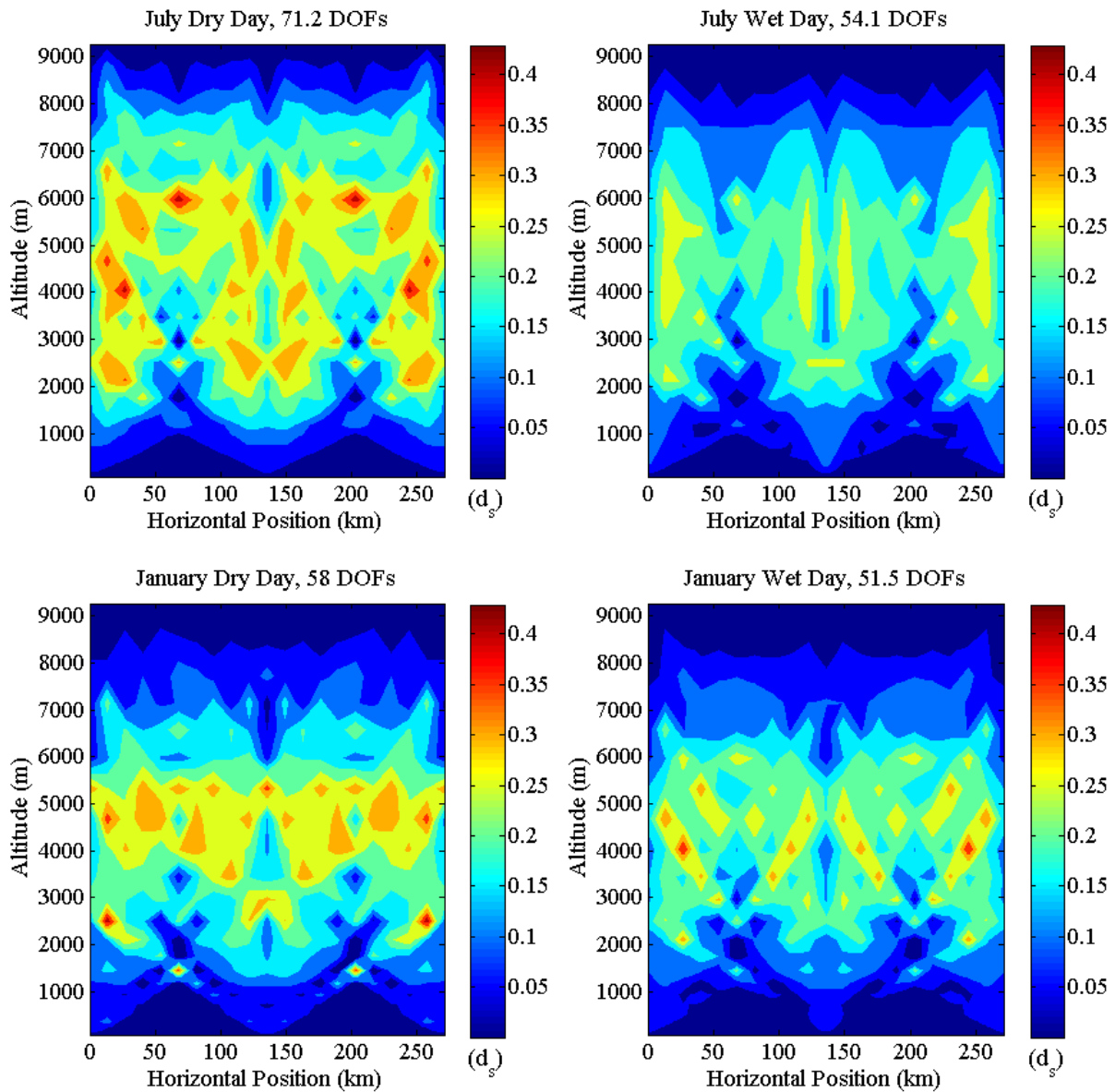


Figure 3.21 Contours of the water vapour DOFs for July (top) and January (bottom) wet (right) and dry (left) cases using three MMR systems.

The increase in instrument coverage has filled in the region of little information at the boundaries of the domain and produced a marked area of water vapour information between 1000 and 7000 meters altitude throughout the domain. Looking at Figure 3.22, we see that we now have ~ 2 water vapour DOFs or more per vertical column.

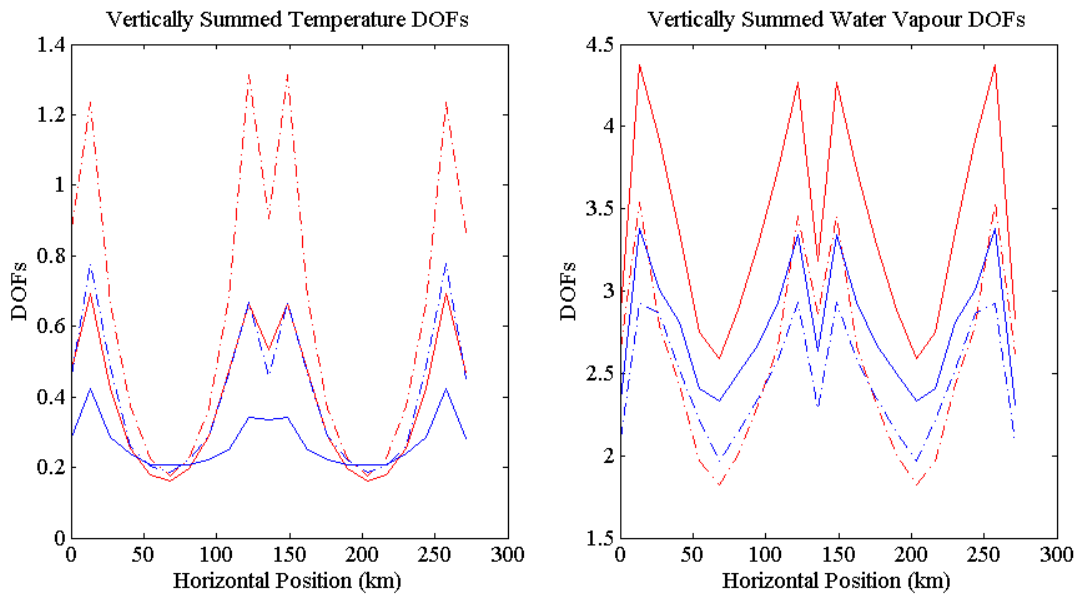
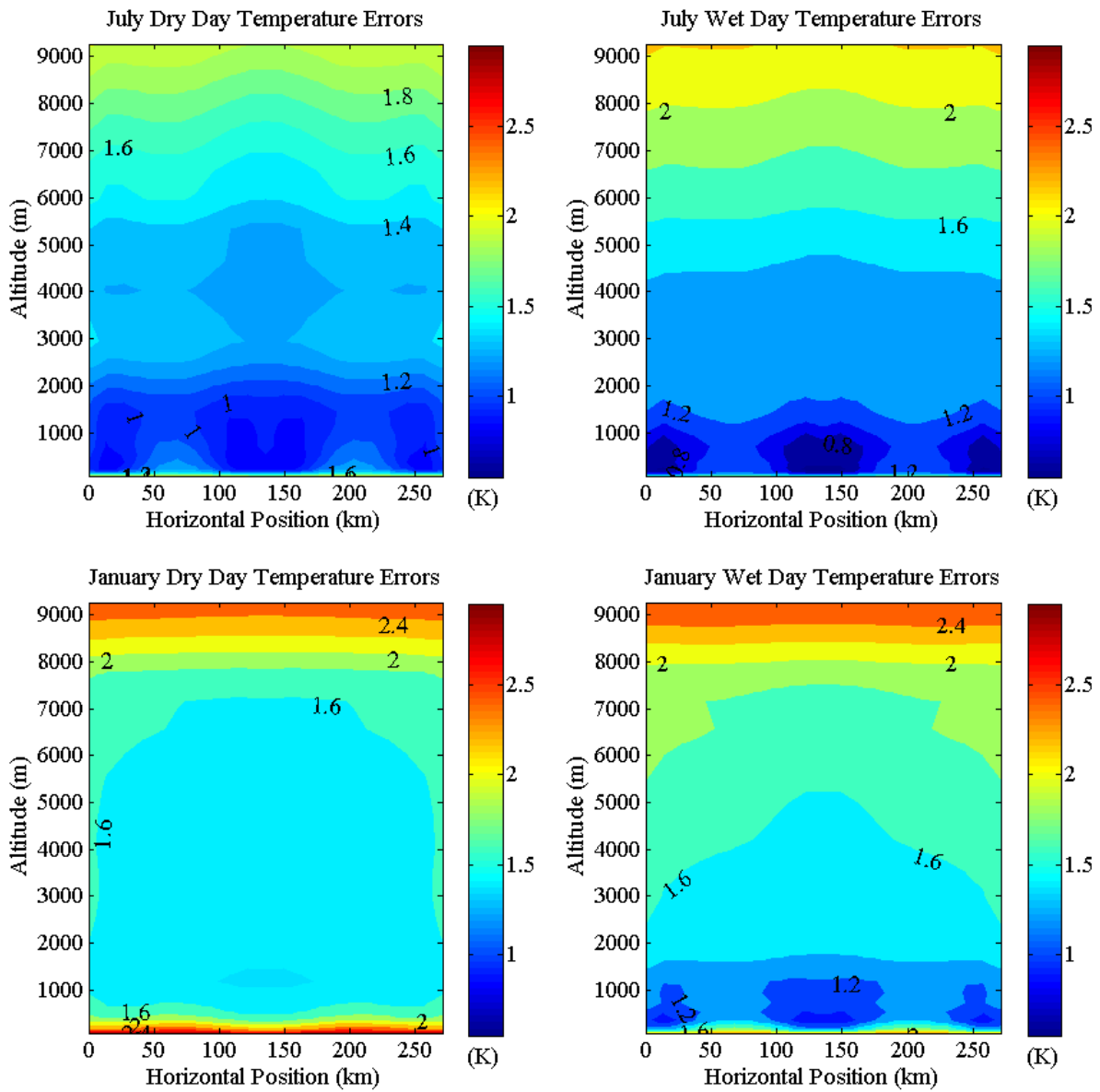


Figure 3.22 Vertically-summed temperature and water vapour DOFs at each horizontal position within the specified domain using three MMR systems.

For temperature, we observe the same type of features as were presented in Section 3.1: strong information content along the lowest elevation scan of each instrument and little information elsewhere. The effects of these constraints can be visualized through examining Figures 3.23 and 3.24, where we have plotted contours of the expected water vapour and temperature retrieval errors.



Figures 3.23 Contours of the expected temperature retrieval errors for July (top) and January (bottom) wet (right) and dry (left) cases using three MMR systems.

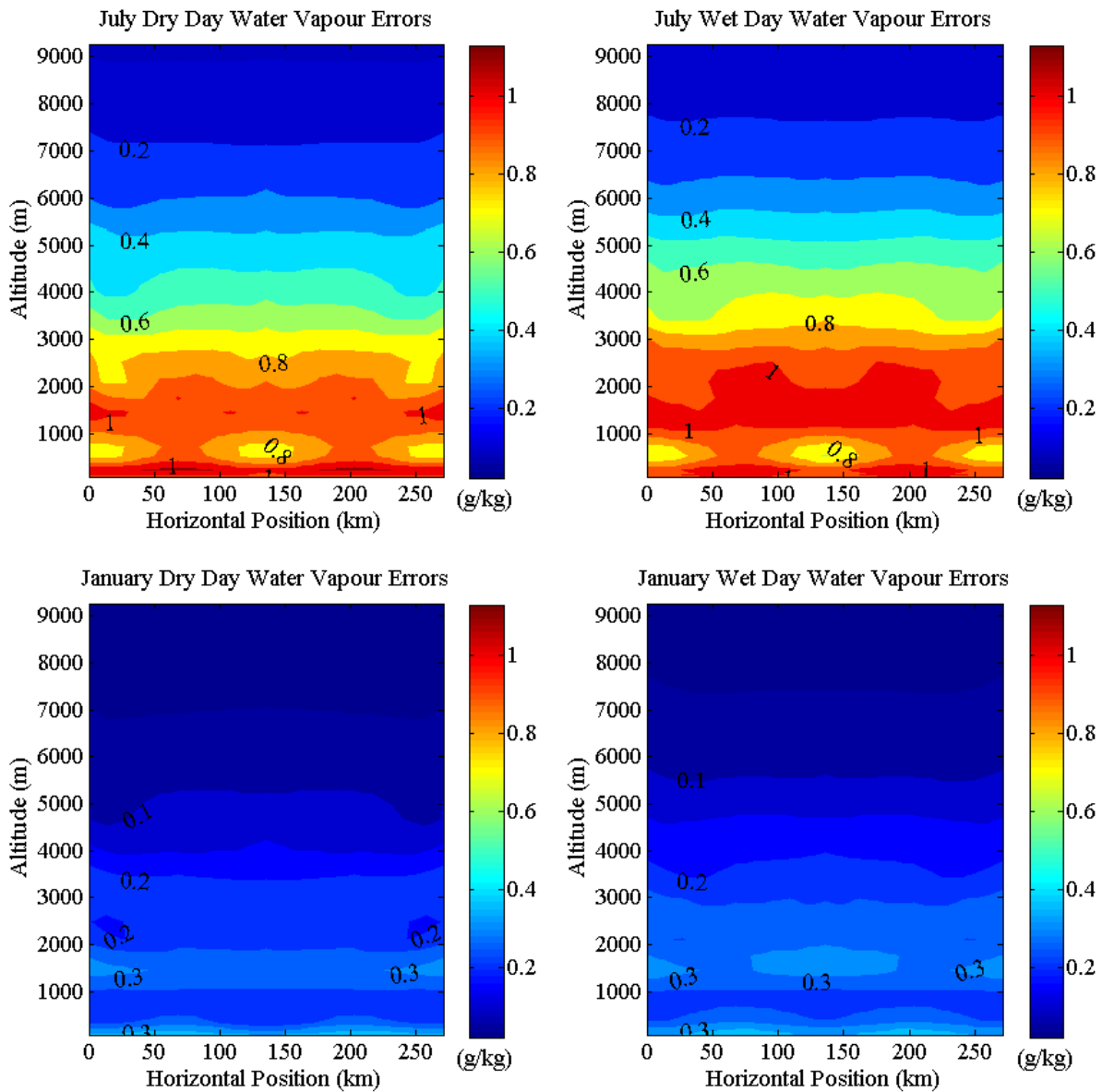


Figure 3.24 Contours of the expected water vapour retrieval errors for July (top) and January (bottom) wet (right) and dry (left) cases using three MMR systems.

As can be clearly seen, the addition of instruments at the edges of the domain has led to a significant increase in the constraint on both water vapour and temperature, where July and January water vapour errors are everywhere below 1 g/kg and 0.35 g/kg, respectively. Temperature constraints are, again, less encouraging, but with the addition of V-band radiometers at each instrument

location, we are able constrain temperature to within $\sim 1\text{K}$ everywhere below 2000 meters altitude. This is demonstrated in Figure 3.25, where we have plotted contours of the temperature DOFs and expected retrieval errors for the dry July case.

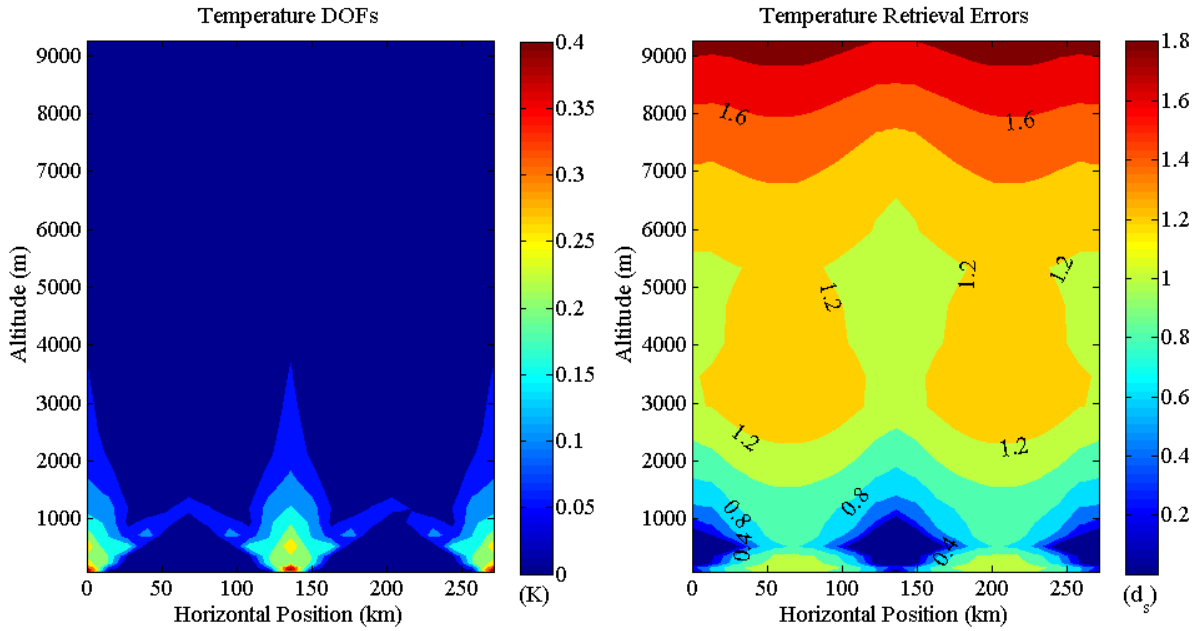


Figure 3.25 Contours of the temperature DOFs (left) and expected retrieval errors (right) using three K- and V-band systems.

A summary of the total water vapour and temperature DOFs for all four cases and the ratios of the multi-instrument DOFs to the single instrument DOFs are presented in Table 3.2.

Table 3.2 Water vapour (WV) and temperature (T) DOFs for various system configurations

Environment	K-Band Radiometer		K-V Band Radiometer		Three K-Band		Three K-V Band		Ratio of 3 to 1 K-Band	
	WV DOFs	T DOFs	WV DOFs	T DOFs	WV DOFs	T DOFs	WV DOFs	T DOFs	WV DOFs	T DOFs
July Dry	36.95	4.06	37.34	9.22	71.28	8.23	72.43	20.33	1.93	2.03
July Wet	27.30	6.56	27.62	10.47	54.07	13.16	54.80	22.84	1.98	2.01
January Dry	29.53	3.37	29.64	8.97	58.00	5.66	N/A	N/A	1.96	1.68
January Wet	26.60	4.37	26.73	9.69	51.46	8.49	N/A	N/A	1.93	1.94

As one can see, the total water vapour and temperature DOFs for each experiment are roughly twice what were retrieved in the single-instrument

experiments of Section 3.1. This is as expected since we have doubled the number of elevation scans through the domain; however, as this ratio is slightly less than double for water vapour, it is likely that some of the information that could be retrieved by the instruments is lost due to correlations between the instrument measurements; thus, intersecting ray paths have led to a decrease in the amount of retrievable information.

This loss of information should be most significant for intersects at midpoints between instruments and may be exacerbated by using a horizontally homogenous a priori state, since the weighting functions from like elevation scans at these mid points will be identical and thus do not contribute any complimentary information. It is, however, unclear how significant of an effect horizontal homogeneity may have on our results, as these weighting functions are only lightly non-linear within the bounds of environmental variability and thus even a natural a priori would likely suffer a similar effect, so long as the degree of non-homogeneity is within the bounds of the typical spatial variability. This effect is less significant, if not nonexistent, in wet environments, as the location of instrument sensitivity is drawn closer to the instrument as humidity increases. This is most obvious in the temperature DOFs: during the dry winter periods, we observe temperature information at significant distances from the instrument where there is greater potential for intersecting rays; during wet periods, most of the instrument's temperature information comes from quite close to the instrument and thus there is little information to be lost at distances where rays intersect.

3.3 How much information do we need?

While these information content computations are interesting and prove that the instrument should be capable of providing information over large horizontal distances, they do not provide a mechanism for assessing whether this instrument can meet the accuracy criteria of Section 1. For this purpose, we attempt to assess the information content associated with those accuracy criteria.

This is done using the same statistical regression framework presented previously, only with a slight modification. In this experiment, we use the retrieval framework to assess the true amount of information required to constrain the field to a specified accuracy; essentially using the statistical regression framework as an interpolator, such that we may determine the degree of independence between points within the domain. For this purpose, we simulate direct measurements of the water vapour fields within the retrieval framework. We then iteratively modify the accuracy of these measurements until the average expected retrieval error of the system at all altitudes is at 0.5 g/kg (for the summer we also use 1.0 g/kg). In the event that the a priori variability is less than the desired accuracy threshold, the expected errors are forced toward the a priori at that altitude. Figure 3.26 demonstrates the layer-averaged water vapour retrieval accuracies for both July and January at the end of this process.

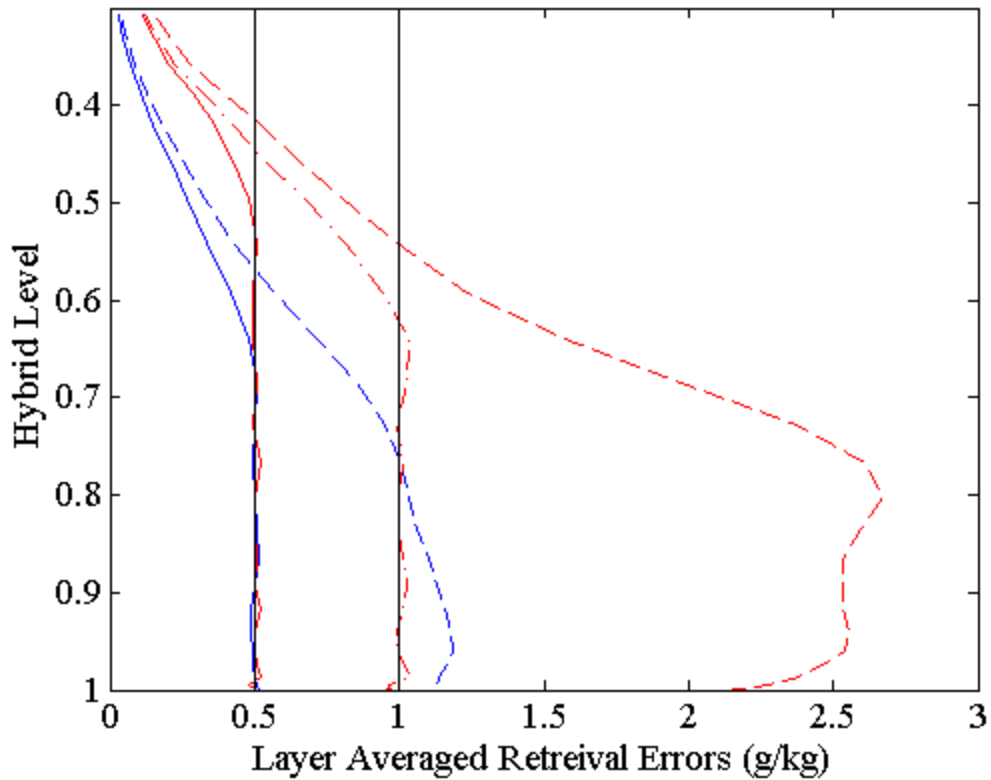


Figure 3.26 Layer-mean water vapour retrieval errors (0.5 g/kg experiment: solid, 1.0 g/kg experiment: dash-dotted) associated with the final measurement setup used in the experiments of Section 3.3. $1\text{-}\sigma$ a priori variability is also plotted (dashed) for comparison.

After the measurement errors have been determined, we use (2.8) to calculate the information content of this state, effectively assessing the information content needed in order to specify the state to the desired accuracy. Contours of the water vapour DOFs determined in this manner for both July and January are presented in Figure 3.27. The total DOFs for each situation are printed in the subplot captions of Figure 3.27.

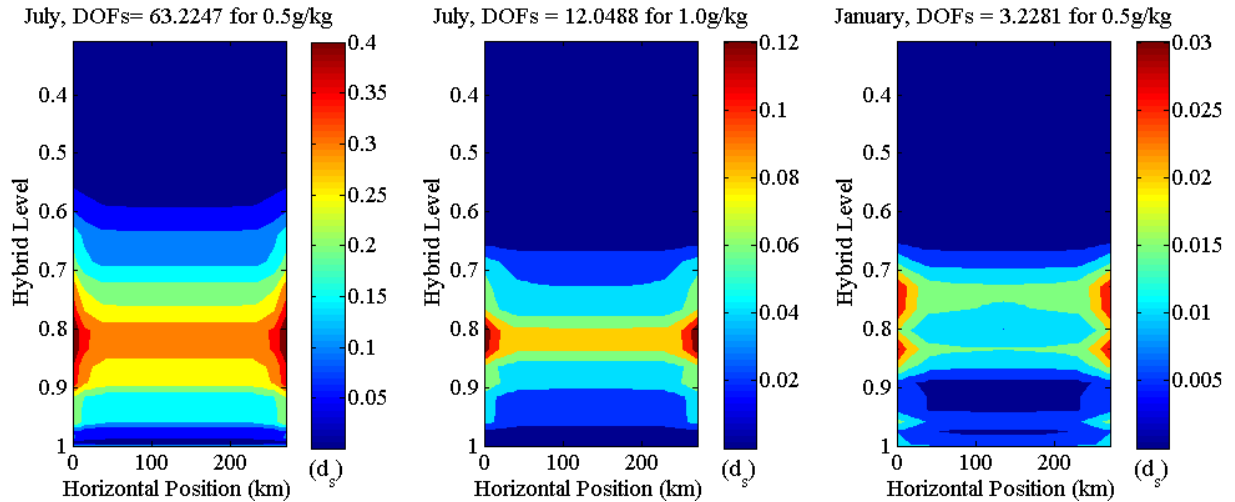


Figure 3.27 Contours of the distribution of DOFs necessary in order to specify the water vapour in the domain to specified accuracies. The total DOFs and specified accuracies are printed in the header of each subplot.

The first and most surprising observation one can draw from Figure 3.27 is the staggering difference between the number of constraints required to constrain water vapour to 1 g/kg and those required to constrain the field to 0.5 g/kg during July: 51.2 DOFs separate these two constraints. This draws into question the feasibility of the 0.2 g/kg, high resolution accuracies desired by some organizations (Hardesty et al., 2012), where exponentially more constraints would be required to achieve such high accuracies. These results, however, are specific to the covariance field of the RAP model, as we do not have a means of generating the true atmospheric covariance fields. An assessment of the sensitivity or accuracy of these results could be done through the use of other atmospheric models, particularly those with higher horizontal resolutions.

While we have no trouble meeting and exceeding the total number of required DOFs for January, July is another case all together. Looking at the sheer number of DOFs necessary in order to constrain water vapour to 0.5 g/kg in July, it would appear as if there is little hope that a single microwave radiometer would

be able to meet the criteria set out in Section 1; however, looking at the distribution of these DOFs as compared to those retrieved from the MMR system, this may only tell half of the story. In Figure 3.28, we have plotted contours of the difference between the MMR and the required DOFs for 0.5 g/kg fields for both the single- and multi-radiometer systems and both summer environments.

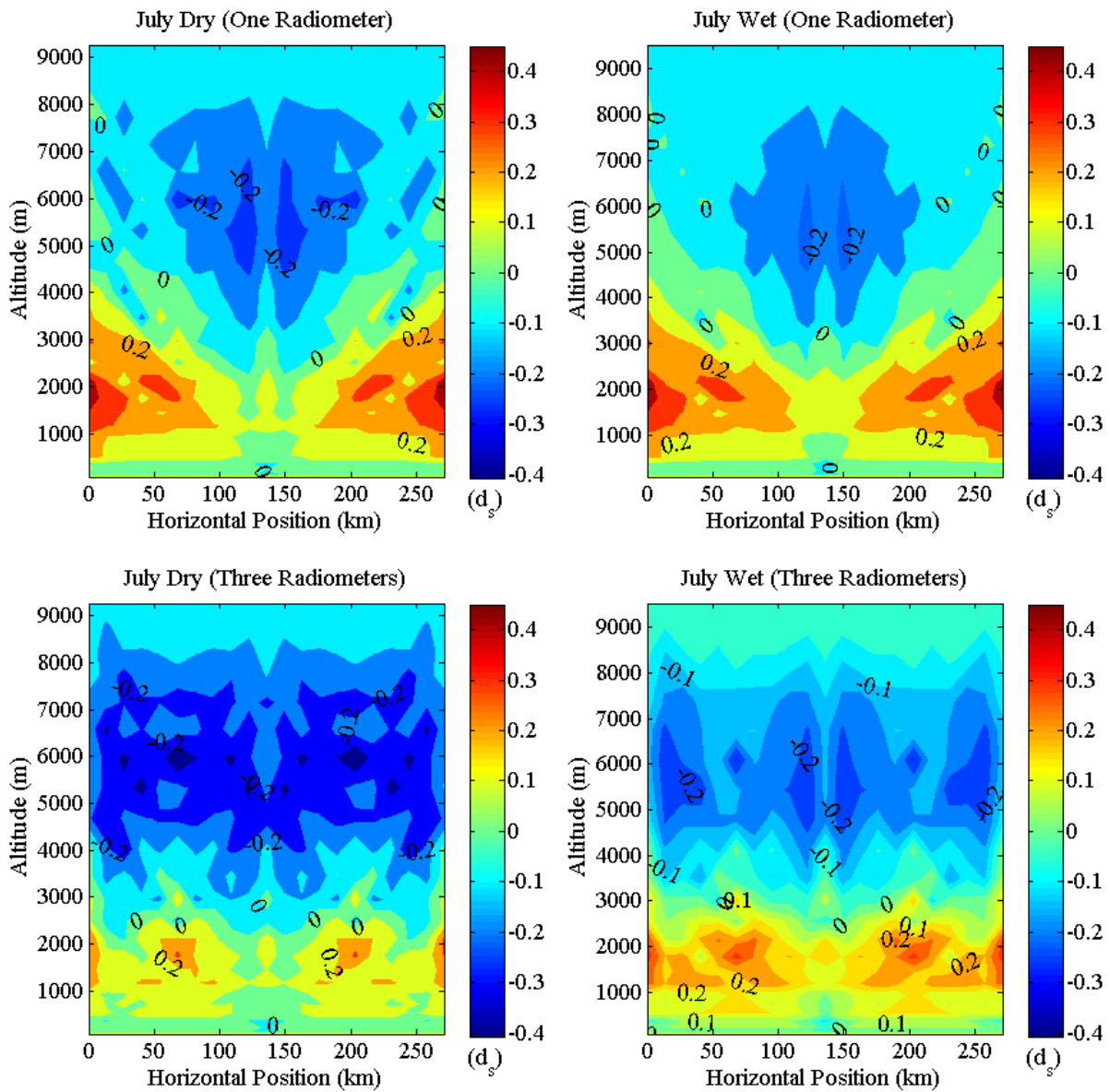


Figure 3.28 Differences between the water vapour DOFs retrieved from the instrument during the July dry (left) and wet (right) cases using one (top) and three (bottom) MMR systems and the DOFs necessary in order to specify the July water vapour field to an accuracy of 0.5g/kg. Negative values imply an over constraint and positive values represent an insufficient constraint.

As one can see, the single radiometer system provides a good constraint on water vapour within its cone of operation, in fact providing a more-than-necessary constraint on water vapour at higher altitudes, but is incapable of providing information at low altitudes away from the instrument. This coverage issue is somewhat addressed through the use of three radiometers but is still not fully corrected; thus, information at low elevations will likely have to be supplemented in some way by another instrument (perhaps by radar refractivity) or through the development of an instrument with an even narrower beamwidth.

Ignoring locations of over-constraint (i.e. negative values in Figure 3.28), we find that there remain a total of 44.18 and 47.79 water vapour DOFs to be constrained in the dry and wet single radiometer cases and 28.08 and 33.61 left to be constrained in the three radiometer cases, respectively.

This experiment was repeated for the three dimensional case, where it was found that only 589.49 water vapour DOFs were necessary in order to constrain the full 3D domain to 0.5 g/kg in July. We have again taken the difference between the required DOF field and that retrieved by the instrument using five degree azimuthal scan density and plotted the results in Figure 3.29.

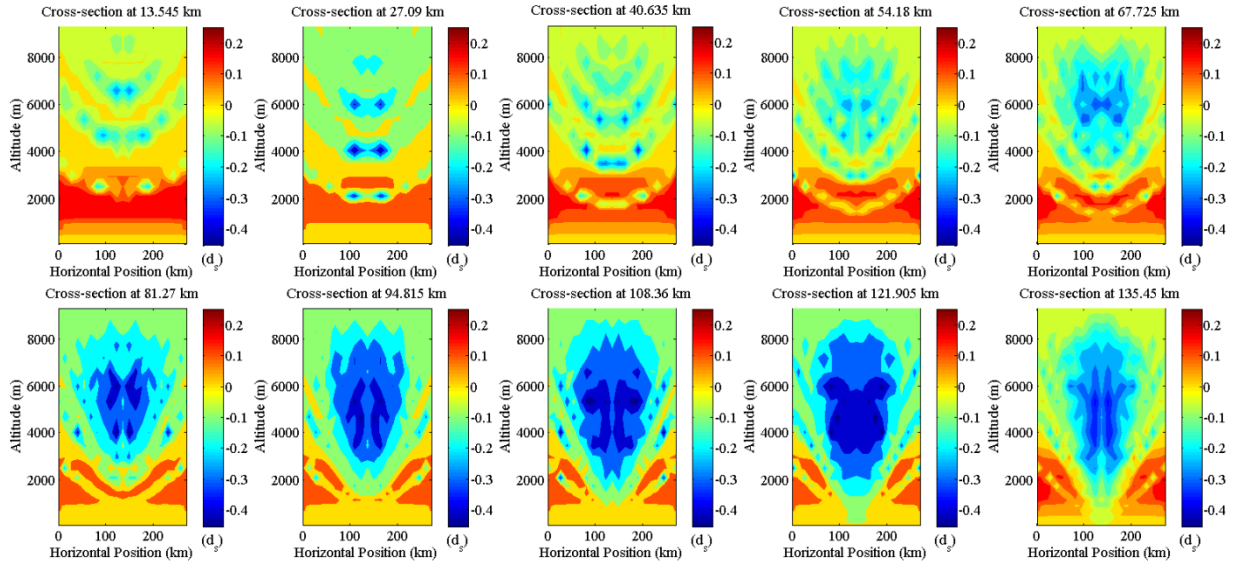


Figure 3.29 Differences between the water vapour DOFs retrieved from the instrument during the dry July case using a single MMR system with five-degree azimuthal scan density and the DOFs necessary in order to specify the July water vapour field to an accuracy of 0.5g/kg. Plot is organized in the same manner as Figure 3.12. Negative values imply an over constraint and positive values represent an insufficient constraint.

Again, we have a more than sufficient constraint on water vapour in the near vertical but fail to offer any real constraint within the lower boundary layer beyond 20 km from the instrument. Similar to the 2D comparisons, there remain 446.66 water vapour DOFs to be constrained in the system in order to achieve the desired measurement accuracy. This large amount of remaining variability is due to the fact that the instrument appears to be most sensitive to the middle atmosphere, above the boundary layer, where less water vapour constraint is necessary to achieve the desired accuracies. This result is consistent with the expected 3D water vapour retrieval errors of Section 3.1.2.

As a general note, we have neglected to undertake this analysis for temperature due to issues with stability when considering temperature in this

manner. As we likely do not come close to fulfilling the temperature requirements specified in Section 1, this is not a particularly great loss.

3.4 Sensitivity to A Priori and Measurement Covariances

While this study is largely a proof of concept, it is important to determine how sensitive our results are to changes in both the a priori and measurement information, as the final implementation of this instrument will likely involve the use of a more sophisticated a priori field and further refinements to the instrument design.

To assess the sensitivity of the total information retrieved by the MMR system to measurement error, we have calculated the 2D water vapour and temperature DOFs retrieved using various multiples of the instrument's measurement covariance matrix. The results of this experiment for all four environmental conditions used previously in this study are presented in Figure 3.30, where the difference in the water vapour and temperature DOFs estimated using the standard error set and the modified error sets is plotted against the factor by which the errors have been modified.

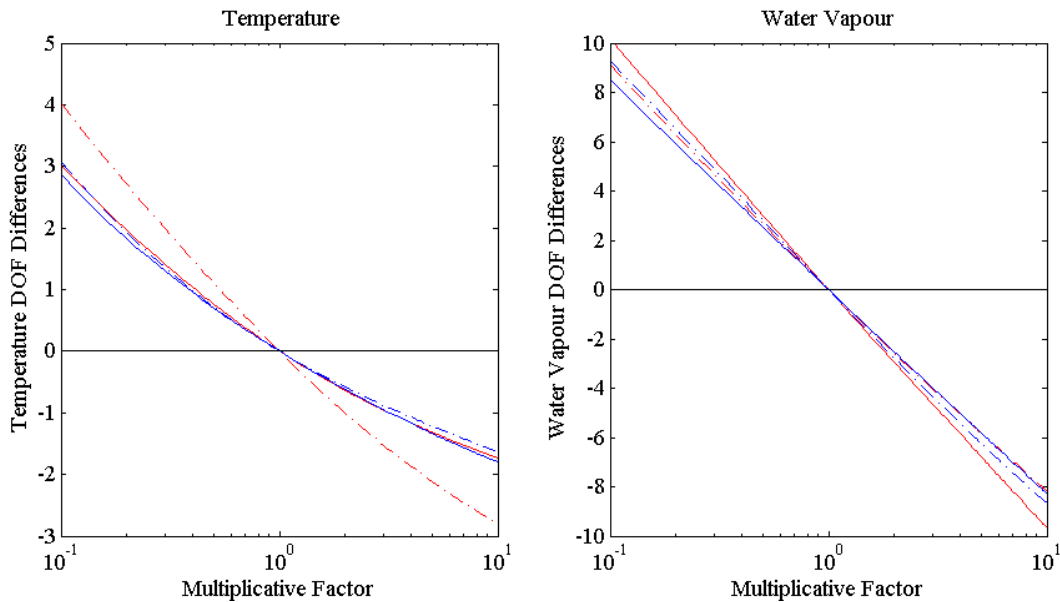


Figure 3.30 Differences between the total temperature (left) and water vapour (right) DOFs retrieved by a single MMR system using the measurement covariances of Section 2 multiplied by various multiplicative factors and those determined with no modification for the four July (red) and January (blue) dry (solid) and wet (dash-dotted) cases. Negative values imply a decrease and positive values imply an increase in DOFs from those of the unmodified case.

As can be seen, a doubling of measurement error will lead to a loss of ~ 3 DOFs for water vapour and ~ 0.6 DOFs for temperature over the entire domain. Likewise halving the instrument measurement errors results a corresponding gain in DOFs. The water vapour results appear to be only weakly affected by the environment used, while the temperature results demonstrate a notable departure from the group in the wettest environment. These increases or decreases in the amount of information lead to corresponding changes in the retrieval accuracy; as such, the change in layer-mean water vapour and temperature errors with respect to changes in measurement accuracy are presented in Figures 3.31 and 3.32.

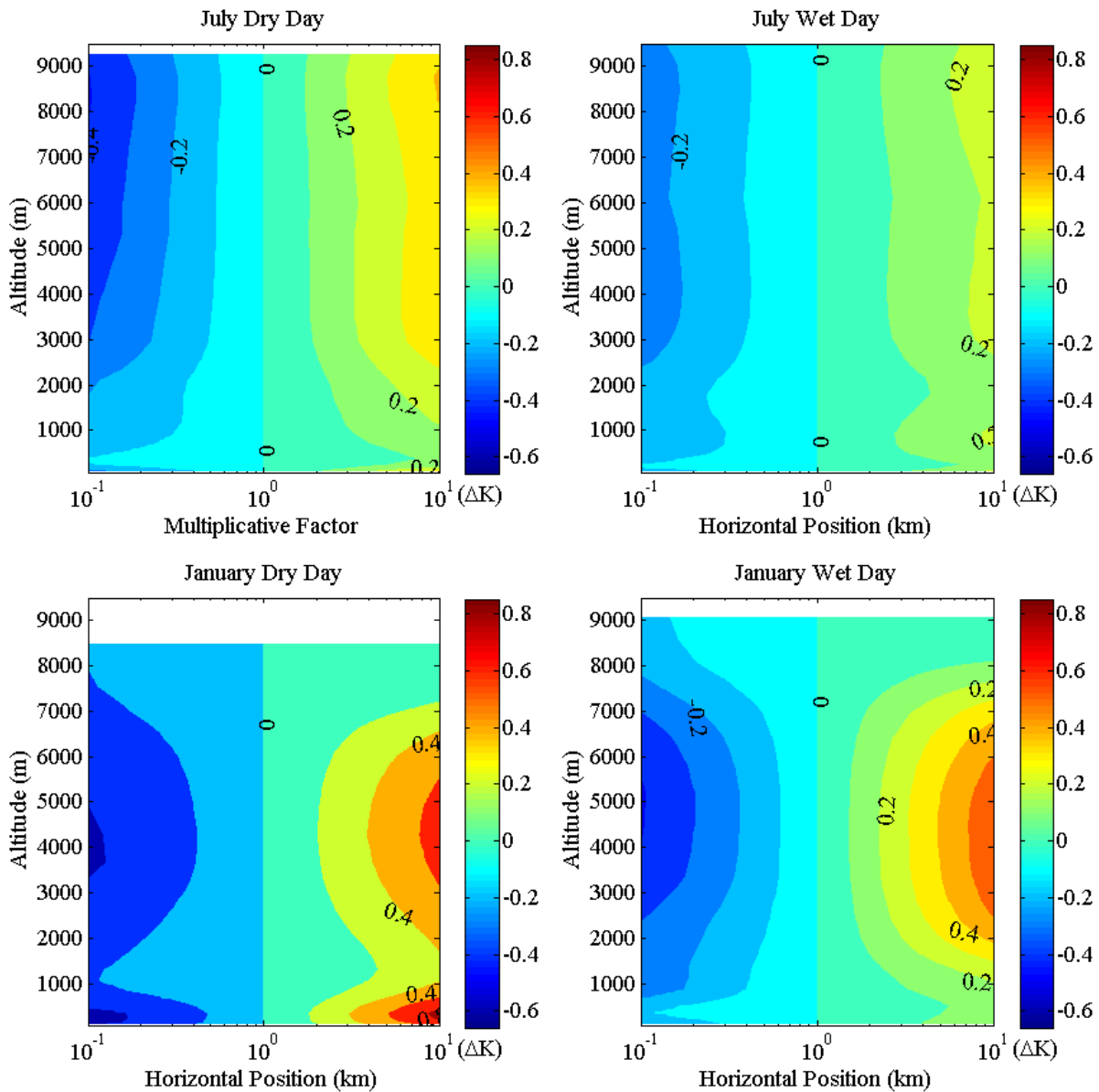


Figure 3.31 Differences between the temperature retrieval errors calculated using the measurement covariances of Section 2 multiplied by various multiplicative factors and those determined with no modification for the four July (top) and January (bottom) dry (left) and wet (right) cases. Negative values imply a decrease and positive values imply an increase in retrieval errors from those of the unmodified case.

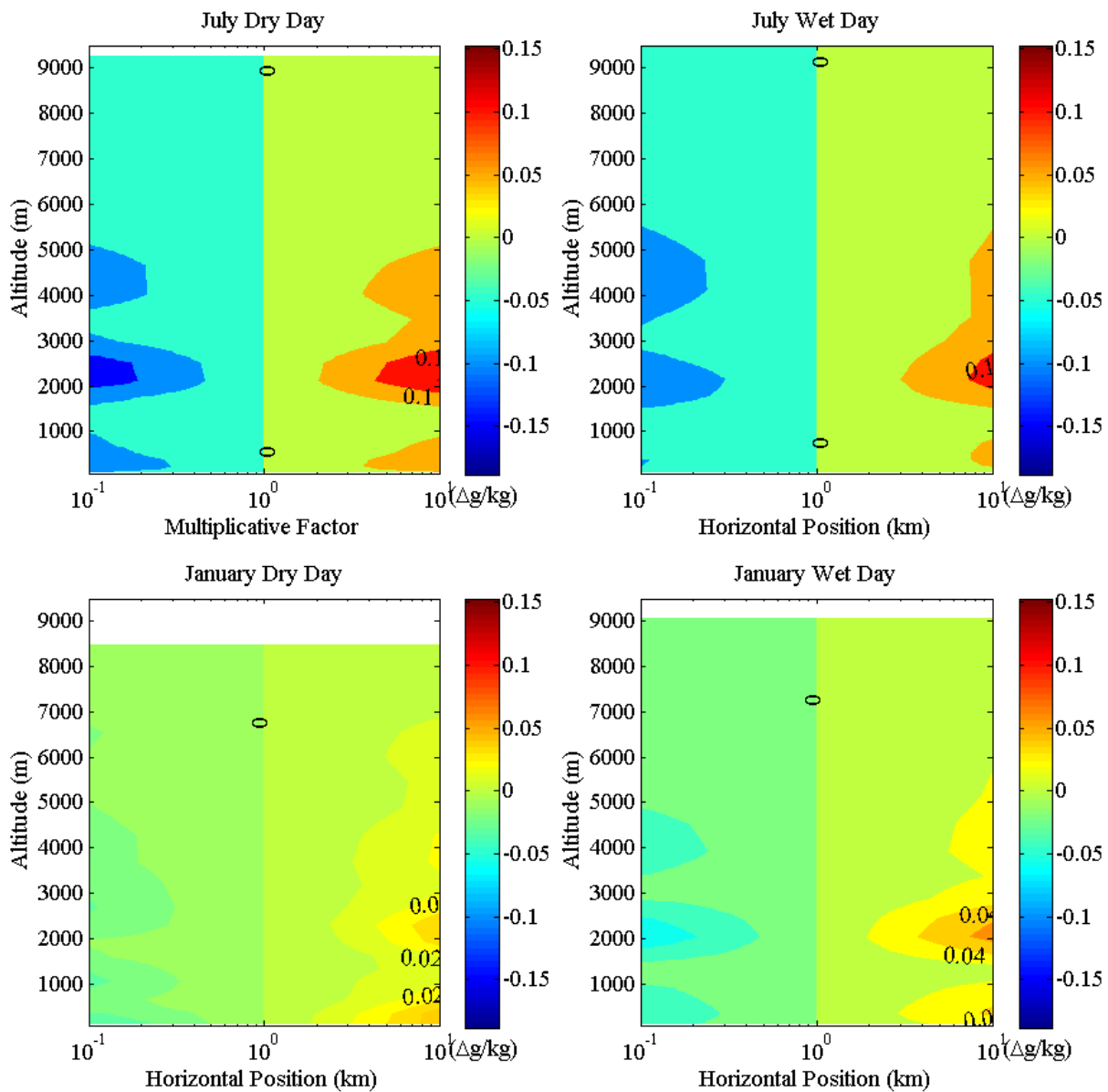


Figure 3.32 Differences between the water vapour retrieval errors calculated using the measurement covariances of Section 2 multiplied by various multiplicative factors and those determined with no modification for the four July (top) and January (bottom) dry (left) and wet (right) cases. Negative values imply a decrease and positive values imply an increase in retrieval errors from those of the unmodified case.

Looking at the water vapour contours, we see that there is little improvement in layer-averaged retrieval errors with even an order of magnitude increase in retrieval error, but the improvement that is achieved is located in the

lower part of the atmosphere, where we have the greatest difficulty in constraining water vapour. For temperature, an increase in measurement accuracy by an order of magnitude does produce an appreciable increase in retrieval accuracy, particularly in dry environments. Also, these results demonstrate that a significant improvement in measurement accuracy might facilitate the retrieval of temperature at higher altitudes, where the maximum altitude of improvement is highly dependent on the humidity of the environment. This is an encouraging observation and will be investigated more thoroughly in the future to assess the limits of the temperature information retrievable by a microwave radiometer. That, however, is outside the scope of this study, since significant changes in measurement errors would not be possible with even significant modifications to the current design of the MMR system. We can, however, improve the a priori information assumed in our retrieval process.

Multiplying the a priori covariance by the same multiplicative factor as was done for the measurement error covariance will result in an identical, but inverse, effect, where decreased a priori variability leads to less information available for retrieval. This is algebraically obvious, given (2.6) and (2.8). While decreasing the amount of a priori variability has the effect of diminishing the information retrieved by the system, the much stronger a priori constraint on these fields will generally lead to a decrease in the retrieval error; thus, there is merit to pursuing a more sophisticated a priori field. This is illustrated in Figures 3.33 and 3.34, where we present contours of the change of layer-mean retrieval errors with

changes in a priori variability or measurement error of up to one order of magnitude above or below that used in the rest of this study.

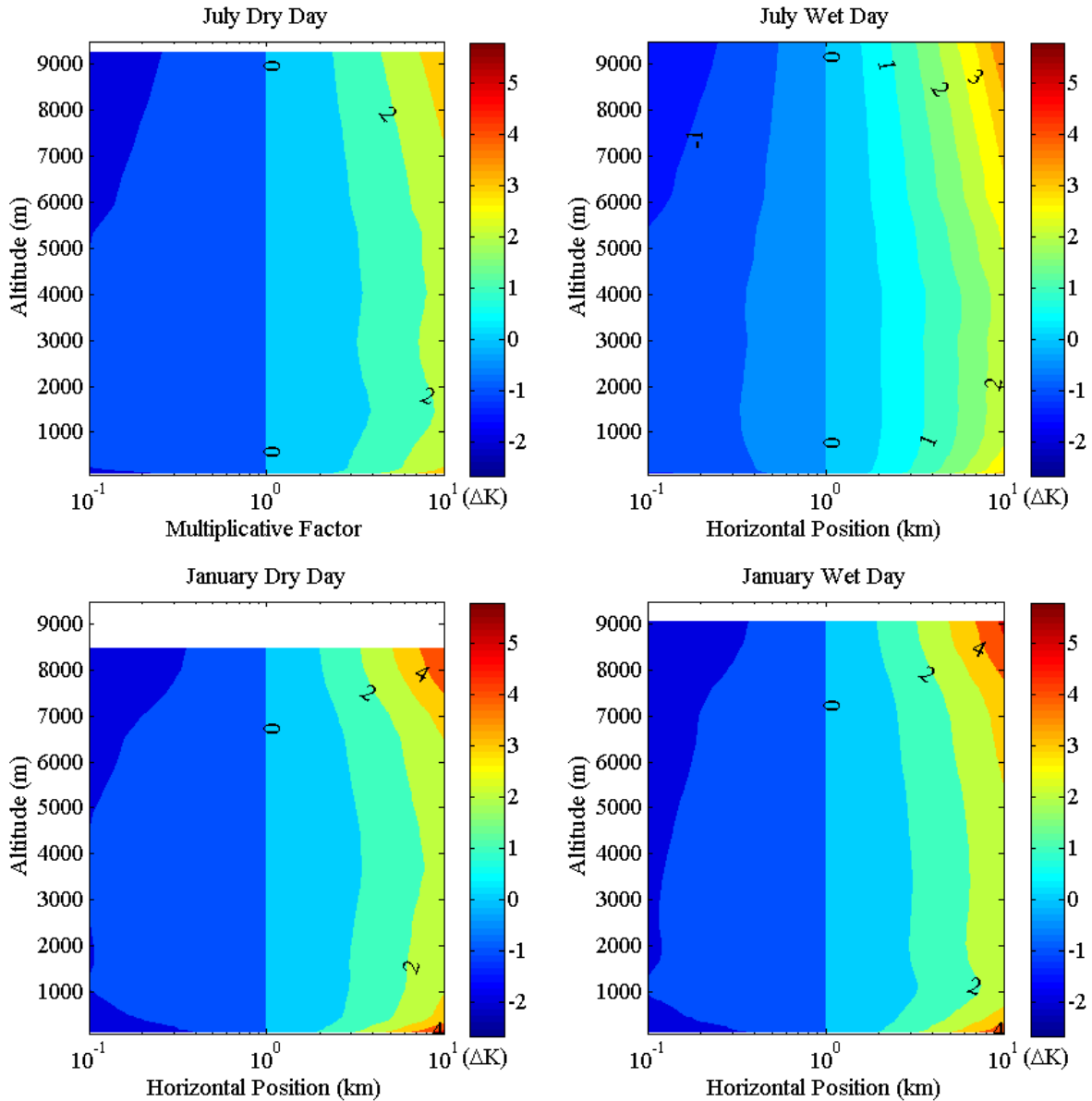


Figure 3.33 Differences between the temperature retrieval errors calculated using the a priori covariances of Section 2 multiplied by various multiplicative factors and those determined with no modification for the four July (top) and January (bottom) dry (left) and wet (right) cases. Negative values imply a decrease and positive values imply an increase in retrieval errors from those of the unmodified case.

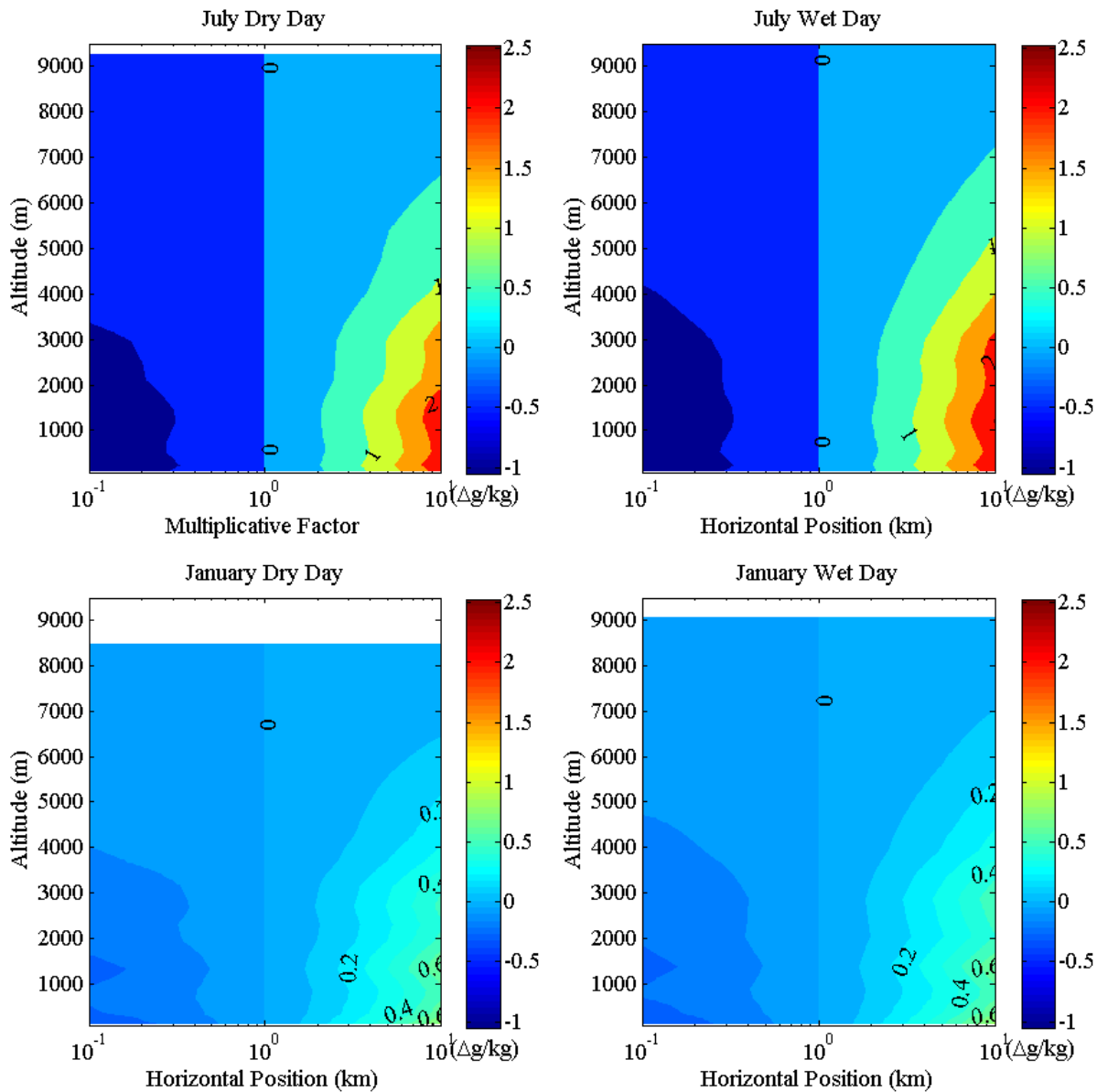


Figure 3.34 Differences between the water vapour retrieval errors calculated using the a priori covariances of Section 2 multiplied by various multiplicative factors and those determined with no modification for the four July (top) and January (bottom) dry (left) and wet (right) cases. Negative values imply a decrease and positive values imply an increase in retrieval errors from those of the unmodified case.

Halving the a priori water vapour variability leads to layer-averaged retrieval error improvements of between 0.3 g/kg at the surface and 0.1 g/kg aloft for summer periods and 0.1 g/kg throughout the domain for winter periods. Doing

the same for temperature, we have an improvement in retrieval error of $\sim 0.4\text{K}$ throughout the middle atmosphere in both summer and winter periods, with improvements of 0.8K and 0.6K at the upper and lower boundaries of the domain for winter and summer periods, respectively. These improvements do not bring the single instrument water vapour retrieval errors to within the 0.5 g/kg accuracies that we set out for, as the improvements are largely located at the edges of the domain, where errors were already quite large. For temperature, however, these changes manifest in a significant improvement in temperature retrieval accuracy, producing a region of greater than 1.0K accuracy up to 2000m altitude within $\sim 50\text{km}$ from the instrument.

We do not go into detail with regards to the effects of increasing the a priori variability, as we have used a monthly climatology as a priori in this study, a sort of worst case scenario a priori field that contains the least amount of a priori information possible (except, perhaps, that of a full annual of multi-year climatology). These results highlight the strong dependence of radiometric retrievals on the characteristics of the a priori field; thus, it is clear that this field should be carefully selected prior to using this type of instrument operationally, constraining the field as much as possible while still allowing an appropriate amount of variability so as to capture the correct retrieved state.

Setting aside this prospect of optimizing the a priori field, we will make an attempt to determine the optimal implementation of the MMR system.

3.5 Instrument Optimization

The MMMR system was designed to be extremely versatile and, as such, is able to scan at virtually any frequency within the range allowed by the instrument's waveguide (excluding those frequencies that are contaminated with interference). The digitally-tuned oscillator allows for the switching of frequencies nearly at will and thus allows for the use of an extremely large number of frequencies at the cost of additional measurement integration time. It is our interest to seek the optimal means of implementing this versatility. By removing the channel switching and thus reducing the number of frequencies from 26 to 8, we could reduce the overall integration time of each scan by a factor of four. This economization of scan time could be used to increase the frequency of instrument scans by a factor of four or to increase the accuracy of each channel by a factor of two (through (2.9) quadrupling the dwell time of a channel will double the channel accuracy). While this reduction in the number of frequencies will result in a decrease in the amount of information retrieved by each scan, the decrease of instrument integration time or measurement error could outweigh that loss. Of particular interest is the potential for decreasing integration time. A full elevation and azimuthal scan, using the elevation scan pattern of Figure 3.2 and an azimuthal scan density of five degrees, would take 17.4 minutes to complete with the current conformation of the instrument. This 17.4 minutes is larger than what we would consider ideal for mesoscale purposes but, by constraining our system to only eight frequencies, this scan time can be reduced to a mere 4.35 minutes, a far more acceptable temporal resolution.

While using only eight frequencies will drastically increase the temporal resolution of the radiometer retrieval, one must have some means of assessing what eight-frequency combination will provide the greatest amount of information. Scheve and Swift (1996) used an eigenvalue decomposition of channel weighting functions to determine which frequency combinations were most linearly independent. This approach is not ideal for a two- or three-dimensional retrieval, as it only uses the radiometer weighting functions and does not consider correlations within the retrieval field or interactions between neighboring scans.

We will approach this problem through an information content perspective using our concept of DOFs. In our approach we determine the water vapour DOFs using our full set frequencies and then determine the DOFs using all frequency combinations with one fewer frequency. The combination with the greatest DOFs is kept as the best combination for that number of frequencies. This process is iterated where the set of available frequencies at the end of each iteration is used as the available set for the next iteration step. Iteration ends once we are left with the best eight-frequency combination. We first undertake this process for a 2D elevation scan, where the instrument was located at the western edge of the domain scanning inward, using the total DOFs over the whole domain as our criteria. This gives us the best eight-frequency combination overall for this instrument setup. The results of this process are presented in Table 3.3 for all four environment cases. In the same table we also present the water vapour DOFs for

the case of using the saved time for doubling the measurement accuracy of the eight frequencies.

Table 3.3 Best overall frequency combinations for an eight-channel radiometer with associated DOFs for normal and double measurement accuracy cases and the DOFs from the 26 frequency system

Environment	Channel 1 (GHZ)	Channel 2 (GHZ)	Channel 3 (GHZ)	Channel 4 (GHZ)	Channel 5 (GHZ)	Channel 6 (GHZ)	Channel 7 (GHZ)	Channel 8 (GHZ)	8-Frequency DOFs	26-Frequency DOFs	8-Frequency DOFs (Double Measurement Accuracy)
July Dry	22.5	26.5	20.2	20.6	22.2	22.6	23.4	26.2	17.99	19.95	19.55
July Wet	22.5	26.5	16.2	20.2	21.0	21.8	22.2	26.2	12.78	14.69	14.13
January Dry	22.5	21.0	22.2	22.6	23.4	23.8	25.0	25.4	14.61	16.09	15.98
January Wet	22.5	26.5	20.6	21.0	22.2	22.6	24.2	26.2	12.82	14.52	14.30

Surprisingly there is a relatively small loss of information between the 26 and 8 frequency combinations, where only ~2 DOFs have been lost over the entire domain. Looking at the DOFs for the case of doubling measurement accuracy of the eight-frequency combination, we find that a gain in measurement accuracy does not outweigh the loss in information by significantly reducing the number of frequencies used; thus, there is little point to reducing the number of frequencies if the saved time is only used to improve the measurement accuracy. The relatively small loss of information between the 26- and 8-frequency combinations suggests that there would be little consequence to using the time saved from using only eight frequencies to decrease the overall scan time and increase the temporal resolution of retrievals. This, obviously, could not be fully evaluated unless we include time in our retrieval, which would consider the correlation of measurements between scans. Nonetheless, higher temporal resolution is favourable for profiling mesoscale processes.

To limit the amount of information lost by reducing the number of frequencies, we may take advantage of the instrument's capability to switch frequencies between measurements at each elevation, adopting an active channel selection strategy. For this type of approach, it is important to identify what

channels combinations are best at each elevation for various atmospheric conditions. For that purpose, we have undertaken the same process as above with a slight modification: rather than undertaking the process for the full scan pattern, we undertake the process evaluating the DOFs for each scan angle independently and thereby determining the best eight-frequency combination for each elevation angle. The results of this process are presented in Figure 3.35.

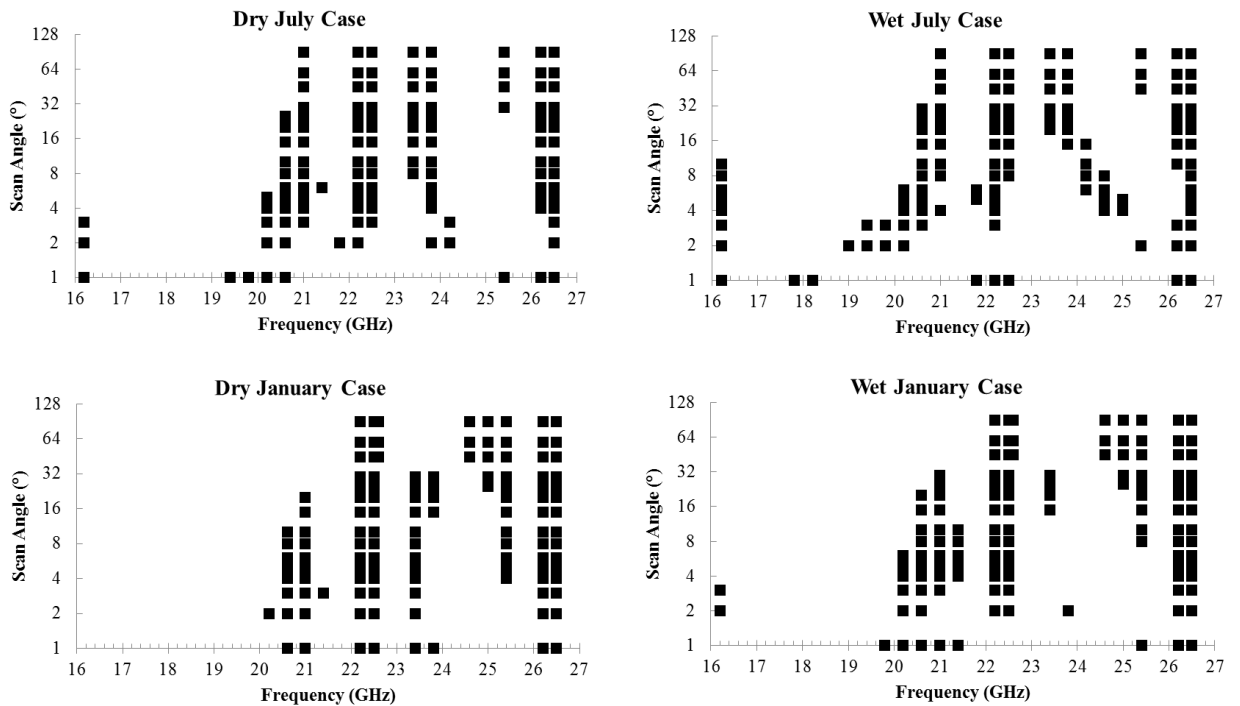


Figure 3.35 Plots of the best eight-channel radiometer frequencies for each scan angle in the four July (top) and January (bottom) dry (left) and wet (right) environments.

Within this figure, trends become apparent: at high elevations, couplets of frequencies above 20 GHz tend to form the basis for the ideal frequency combination; for the low water vapour cases, the frequency combinations demonstrate little variability with changes in elevation angles; for situations with high water vapour, the frequencies of the combinations tend to spread

significantly at lower elevations; and for nearly all cases, the lowest frequency channel at 16.2 GHz becomes a member of the best combinations at low elevation angles. The tendency for forming couplets is likely the result of little linear independence between channels, making the increase in accuracy, due to redundant, closely spaced measurements, more important than the small amount of information gained from the little linear independence between channels spaced far apart. This also confirms the results of Scheve and Swift (1996), where they demonstrated that there was little information to be gained through the use of more than four channels or by channels below 20GHz. Our results diverge from those of Scheve and Swift (1996) at low elevations in wet environments, where half the channels are at frequencies below 20 GHz and the frequencies are better spaced. Scheve and Swift (1996), however, did not consider scanning in their approach and thus this divergence is not surprising.

Overall, the results of Figure 3.35 suggest that using a single set of eight frequencies should be roughly sufficient for all elevations in dry environments, but will result in a significant loss of information at low elevations in wet environments. Using these results, and perhaps an expansion of this experiment for more environments, one may be able to develop a channel selection strategy that takes the most advantage of the information available from an eight-channel radiometer.

4. Conclusions

This study encompasses a variety of topics addressing the capability of a scanning microwave radiometer for providing accurate, three-dimensional water vapour and temperature fields. Theoretical experiments, run in four different atmospheric conditions, examine the 2D and 3D information content of a scanning microwave radiometer. These experiments demonstrate appreciable retrievable information at distances exceeding 150km from the instrument. The total number of water vapour and temperature constraints available from a single instrument were found to vary between 26.6 to 36.9 DOFs and 3.4 to 6.6 DOFs, respectively, for the 2D case. For water vapour information is found to increase with decreasing a priori water vapour, while for temperature, information is found to increase with increasing water vapour. Water vapour information is found to reside primarily in the region between 1000 and 7000m altitude and temperature information is found to reside much closer to the instrument, largely at altitudes below 1500m. Vertically summed water vapour DOFs are found to exceed ~ 2 DOFs at all locations within 50km of the instrument and never fall below 0.5 DOFs, while corresponding temperature DOFs are far more localized and variable based on the amount of a priori water vapour, reaching between 0.2 and 1.2 DOFs within 20km of the instrument but falling to ~ 0.1 DOFs outside of that range. Both water vapour and temperature DOFs are shown to reach a local minimum directly above the instrument. Overall, these results suggest that, not only can we retrieve information at large distances from the radiometer at comparable amounts to an analogous vertically pointing instrument, but we also outperform vertically pointing instruments at locations between 10 and 30km from the instrument.

Other experiments are undertaken using various conformations of instruments and adding further systems. It is found that, with the addition of instruments at the edges of the domain, the retrieved information content roughly doubles from that of the single instrument case. With the addition of a single V-band radiometer at the location of the MMR instrument, we find no appreciable increase in water vapour information but do find a doubling of temperature information that spreads to far greater altitudes than that of the MMR system alone. With the use of three MMR and V-band systems separated by 135.45km, we find that, even with the worst case a priori constraint, we are able to constrain temperature to within $\sim 1\text{K}$ at all locations below 2000m and water vapour to accuracies of $\sim 1\text{g/kg}$ over the entire domain in both summer cases, where accuracies increase to 0.15K and 0.7g/kg, respectively, as one approaches the region just above the instruments.

In the case of three-dimensional retrieval, with both elevation and azimuthal scanning, we find that the system is capable of providing 617.97 water vapour and 34.78 temperature constraints during the dry summer case while using a 5 degree azimuthal scan density, where increases in retrievable information had yet to saturate at even this high azimuthal scan density. Future experiments will test the limits of retrievable information from the system using higher azimuthal scan densities; nonetheless, these results vastly exceed the 2-3 water vapour and 1-3 temperature constraints found using these instruments for vertical profiling (Löhnert, et al; 2009).

An assessment of the sensitivity of these results to a priori variability and measurement errors is undertaken. We find that increasing measurement accuracies by an order of magnitude will do little to improve the water vapour errors of the retrieval but could lead to stronger temperature constraints at higher altitudes than are currently available. Halving a priori variability is found to have far more significant implications, where temperature and water vapour retrieval errors could be reduced appreciably but still not to within the criteria of Weckwerth et al. (1999).

While the instrument does not appear to be capable of reaching the criteria set out in the introduction, an attempt is made to assess the amount by which it falls short. Using a statistical regression approach it was found that one would need 63.22 independent constraints, concentrated between 500 and 4000m altitude, in order to define water vapour to within 0.5g/kg throughout the entire 2D domain examined during summer periods and only 3.22 to do the same during winter periods. Over the full three dimensional domain, this translates into 589.49 constraints in summer periods. Comparing this to the results for a single MMR system, it is found that there remain over 44 DOFs to constrain in the 2D case and 446 in the 3D case after the MMR system's information is accounted for, since the region of the instrument's sensitivity does not necessarily match the region of greatest variability.

Optimization of the MMR system is also considered. It is shown that, with the compromise of a few DOFs, the instrument frequency set can be reduced to a mere eight frequencies, reducing the required measurement integration time

by a factor of four. The time saved in this manner is found to be best used to reduce the time of a full instrument scan rather than improving the measurement errors of the remaining eight channels, as the improvement through this increase in accuracy would in fact lead to less information than would be available if the full 26 frequencies were used instead at the standard accuracy. The best combination of eight frequencies to be used by the instrument is found for each elevation angle, where it is shown that a fixed set of eight frequencies would serve well for elevations above five degrees and during winter periods but would not be optimal at low elevations. This leads us to believe that an active channel selection strategy would be ideal for this instrument.

5. Future Work

There is a significant amount of work left to be done prior to using MMR measurements to reconstruct three-dimensional profiles of water vapour or temperature. The foremost of this work is concerned with accurately constructing the radiometer error covariance matrix, assessing the appropriate method by which to assimilate radiometer measurements, and exploring synergies between radiometers and other instruments.

The problem of accurately assessing the measurement error covariance is not a simple one, as measurement errors are composed of several components that cannot be estimated directly. The measurement error covariance can be thought of as the sum of thermal noise errors, calibration biases, measurement drift errors,

forward model errors, and representativeness errors. For an explanation of representative errors, we leave it to the reader to consult Lorenc (1986) and Lorenc and Hammon (1988), which provide a detailed discussion on this matter. The two main components of the measurement errors with which we are concerned are the thermal noise errors and forward model errors.

Forward model errors arise as a result of our inadequate knowledge of the spectroscopic properties of atmospheric constituents, smoothed parameterizations of these spectroscopic properties, and through the use of a discretized field. Errors due to spectroscopic parameterization can be roughly estimated by comparing the brightness temperatures simulated by various absorption models in various atmospheric conditions. Errors due to profile discretization can be calculated through the use of high resolution data: radiosonde or LIDAR data for pure-vertical sensing or a high resolution model for two- or three-dimensional sensing. These fields and fields discretized to the resolution of our retrieval are used as inputs to the forward model. The covariance of the difference between these brightness temperatures can then be taken as an estimate of the discretization error of our choice of retrieval grid.

In our assessment, we assumed completely uncorrelated, theoretical thermal noise, measurement errors. We know however, that this is an idealization and may not adequately represent the actual magnitude or structure of the real measurement error covariance. In order to estimate these thermal noise errors experimentally, we will require the use of the operational MMR instrument.

The most basic method to estimate these errors would be by simply directing the instrument towards a stable target (a reference blackbody or liquid nitrogen target) in stable atmospheric conditions. Taking brightness temperature measurements over the course of an appreciable time frame, one may calculate the variability of these measurements from the mean. The measurement noise error covariance is then simply constructed from the variance of each channel and the inter-channel covariances of the observed variability from the mean over the chosen time frame. This process not only results in a direct estimate of the measurement errors but also produces realistic off-diagonal measurement error covariances.

While appropriately estimating the instrument errors is necessary prior to the operational use of the MMR system, an equally important task is that of choosing an appropriate a priori, offering the most prior information possible. This would likely involve creating the a priori covariance field from a short term forecast and using a forecast state as the a priori state. It is, however, more likely that one would seek to use the measured radiometer radiances directly, employing them as a model constraint using a forward model. This would bypass the need to specify a priori fields, as the model background would indirectly serve that purpose; thus, the model assimilation of measured radiances should be investigated.

The third major direction of future research should focus on taking advantage of the inherent synergy of radiometer measurements. One may endeavor to examine the benefits of incorporating GPS receiver measurements

into the retrieval, as GPS measurements could provide additional ray paths of constraint on the system variables. Also, GPS receivers and microwave radiometers are both exceptional at estimating integrated water vapour; thus, the ability for using GPS measurements to assist in the calibration of an associated radiometer could be investigated through these measurements of integrated water vapour.

As was highlighted in the above study, a radiometer system is incapable of providing water vapour constraints near the surface at appreciable distances from the instrument due to limitations in the instrumentation and ground contamination. This limitation could be, at least partially, accounted for through the use of near-surface radar refractivity measurements, which take advantage of ground clutter. Also, the MMR system would, ideally, be capable of providing information within precipitation. This, however, would require cooperation between the radiometer and a radar.

At the outset of this project, we were particularly interested in the capabilities of the MMR system within precipitation. As can be seen in Figure 1.1, the microwave spectrum is exceptionally sensitive to even modest amounts of precipitation; in fact, at the MMR frequencies, the range of liquid water opacities is similar to those of water vapour. This wide range of opacities suggests that the MMR system should be capable of retrieving liquid water thermal properties within precipitation. There is, however, a simple caveat to applying these systems within precipitation: scattering, which can be ignored for water vapour, is non-negligible when considering liquid water droplets of appreciable

size. In order to assess importance of scattering within precipitation at the frequencies of the MMR system, we considered the scattering and absorption properties of three environments: an environment with 50mm/hr rainfall at a temperature of 10C, an environment with 2mm/hr rainfall at a temperature of 10C, and an environment with 1mm/hr liquid-equivalent snowfall at -5C. Scattering and absorption coefficients for all three of these environments were calculated using a simple scattering model developed by Fabry and Szyrmer (1999) for the range of frequencies between 5.0 and 40.0 GHz. The results of these runs are presented in Figure 5.1.

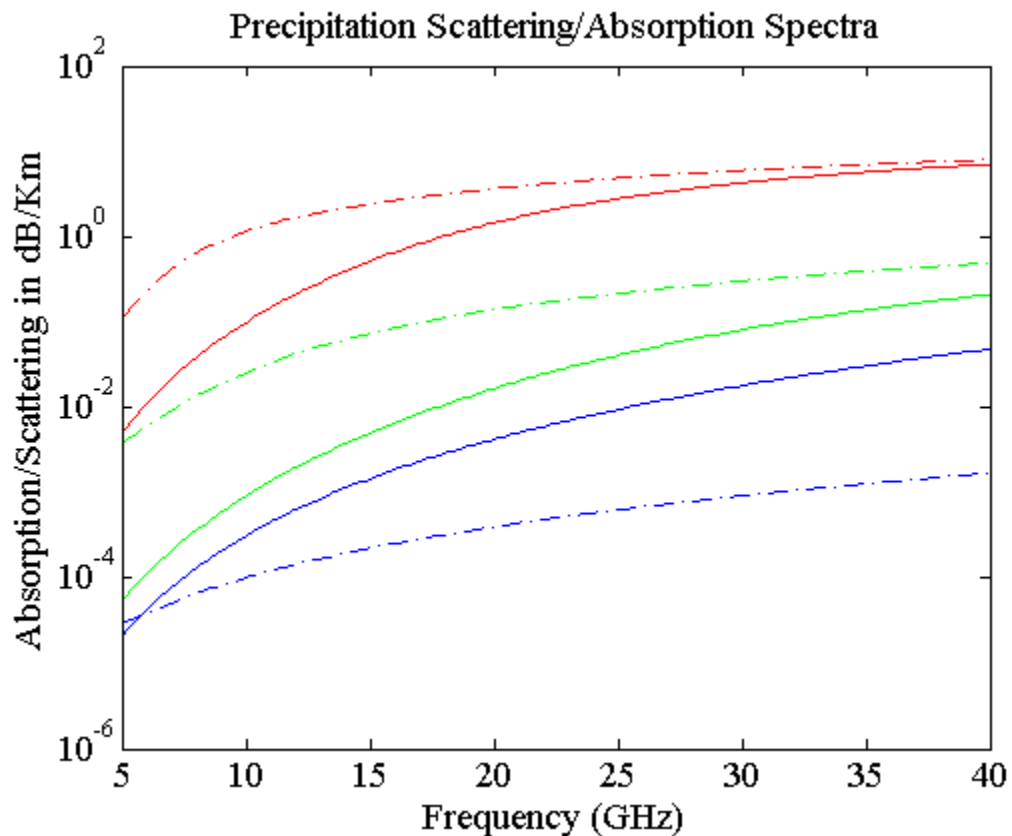


Figure 5.1 Scattering (solid) and absorption (dash-dotted) spectra for the case of 50mm/hr rainfall (red), 2mm/hr rainfall (green), and 1mm/hr snowfall (blue).

There are some expected features in the above Figure: the effect of scattering in snowfall significantly outweighs that of absorption, the amount of scattering increases with increasing frequency, and the amount of scattering and absorption increases with increasing rainrate. This Figure does a good job highlighting the issue of scattering within precipitation. During periods of weak precipitation, the absorption contribution of precipitation exceeds that of scattering by an acceptable order of magnitude throughout the range of frequencies used by the MMR system, but as rainrate increases, these contributions become dangerously similar for frequencies above 20GHz; thus, for high rainrates and at frequencies above 20GHz, scattering obviously cannot be ignored. That said, at low frequencies and low rainrates, scattering contributions are marginal and thus, could be neglected if accounted for appropriately within the measurement covariance matrix.

These results do not rule-out the possibility of applying a microwave radiometer within precipitation. With the use of an advanced scattering model and an accompanying radar, scattering and liquid water contributions to radiometer measurements may be neglected. This, of course, would be highly computationally expensive. A more simplistic possibility is to use radar precipitation measurements to actively limit the maximum frequency of the radiometer such that the potential impacts of scattering on radiometer measurements are minimized within precipitation.

The final topic of work left to be done involves the expansion of this study to higher horizontal resolutions. This would simply require the use of a

background model or analysis with higher horizontal resolution than that of RAP. Also, as increasing the resolution of the system would drastically increase the, already significant, computational requirements of this process, one should endeavor to acquire or construct a fast radiative transfer model.

References

- Battaglia, A., P. Saaverdra Garfias, T. Rose, and C. Simmer (2010). Characterization of precipitating clouds by ground-based measurements with the triple-frequency polarized microwave radiometer ADMIRARI, *J. Appl. Meteorol. Clim.*, **49**, pp. 394–414.
- Bender, M., G. Dick, M. Ge, Z. Deng, J. Wickert, H. Kahle, A. Raabe, and G. Tetzlaff (2011). Development of a GNSS water vapour tomography system using algebraic reconstruction techniques, *Advances in Space Research*, **47**(10), pp. 1704-1720.
- Bevis, M. (1994). GPS meteorology: mapping zenith wet delays onto precipitable water, *Journal of Applied Meteorology*, **33**(3), pp. 379-386.
- Bleisch, R., N. Kämpfer, and A. Haeferle (2011). Retrieval of tropospheric water vapour by using spectra of a 22 GHz radiometer, *Atmos. Meas. Tech.*, **4**(9), pp. 1891 - 1903.
- Bleisch, R., and N. Kämpfer (2012). Adding constraints by in situ informations to optimal estimation retrievals of tropospheric water vapour profiles from microwave radiometry, *J. Quant. Spec. and Rad. Trans.*, **113**(16), pp. 1993 - 2003.
- Bodine, D., P.L. Heinselman, B.L. Cheong, R.D. Palmer, and D. Michaud (2010). A case study on the impact of moisture variability on convection initiation using radar refractivity retrievals, *Journal of Applied Meteorology and Climatology*, **49**(8), pp. 1766-1778.
- Bösenberg, J. (1998). Ground-based differential absorption lidar for water-vapor and temperature profiling: methodology. *Applied Optics*, **37**(18), pp. 3845-3860

- Cadeddu, M. P. (2012). Microwave Radiometer – 3 channel (MWR3C) Handbook, Office of Science, US Department of Energy, DOE/SC-ARM/TR-108, Washington, DC, USA.
- Crewell, S., H. Czekala, U. Löhnert, C. Simmer, T. Rose, and R. Zimmermann (2001). Microwave radiometer for cloud cartography: a 22-channel ground-based microwave radiometer for atmospheric research, *Radio Sci.*, **36**, pp. 621 - 638.
- Crewell, S., and U. Löhnert (2007). Accuracy of Boundary layer temperature profiles retrieved with multifrequency multiangle microwave radiometry, *IEEE T. Geosci. Remote*, **45**, pp. 2195 - 2201.
- Crook, N.A. (1996). Sensitivity of moist convection forced by boundary layer processes to low-level thermodynamic fields. *Mon. Wea. Rev.*, **124**, pp. 1767–1785
- Dinoyev, T.S., V.B. Simeonov, Y.F. Arshinov, S.M. Bobrovnikov, R. Ristori, B. Calpini, M.B. Parlange, and H. van den Bergh (2012). Raman LIDAR for Meteorological Observations, RALMO – Part I: Instrument description. *Atmos. Meas. Tech. Discuss.*, **5**, pp. 6867-6914, doi:10.5194/amtd-5-6867-2012
- Ebell, K., U. Löhnert, S. Crewell, and D.D. Turner (2010) On characterizing the error in a remotely sensed liquid water content profile, *Atmos. Res.*, **98**(1), pp. 57 - 68.
- Fabry, F., C. Frush, I. Zawadzki, and A. Kilambi (1997). On the extraction of near-surface index of refraction using radar phase measurements from ground targets. *Journal of Atmospheric and Oceanic Technology*, **14**(4), pp. 978-987.
- Fabry, F., and W. Szyrmer (1999). Modeling of the melting layer. Part II: Electromagnetic, *J. Atmos. Sci.*, **56**(20), pp. 3593 - 3600.
- Fabry, F. (2004). Meteorological value of ground target measurements by radar, *Journal of Atmospheric and Oceanic Technology*, **21**(4), pp. 560-573.
- Fabry, F. (2006). The spatial structure of moisture near the surface: Project-long characterization. *Monthly Weather Review*, **134**, pp. 79-91.
- Fabry, F., and V. Meunier (2009). Conceptualisation and Design of a "Mesoscale Radiometer". Proceedings, *8th International Symposium on Tropospheric Profiling*, Delft, Netherlands, 18-22 October 2009, S06-P03.
- Fabry, F., and J. Sun (2010). For how long should what data be assimilated for the mesoscale forecasting of convection and why? Part I: On the propagation of initial condition errors and its implications for data assimilation. *Monthly Weather Review*, **138**, pp. 242-255.

- Foelsche, U., and G. Kirchengast (2001). Tropospheric water vapor imaging by combination of ground-based and spaceborne GNSS sounding data, *Journal of Geophysical Research D: Atmospheres*, **106**(D21), pp. 27221-27231.
- Goody, R.M., and Y.L. Yung (1989). *Atmospheric Radiation: Theoretical Basis*. New York: Oxford University Press.
- Grant, W.B. (1991). Differential Absorption and Raman Lidar for water vapor profile measurements: a review. *Optical Engineering*, **30**(1), pp. 40-48.
- Hardesty, R., R. Hoff, F. Carr, T. Weckwerth, S. Koch, A. Benedetti, S. Crewell, D. Cimini, D. Turner, W. Feltz, B. Demoz, V. Wulfmeyer, D. Sisterson, T. Ackerman, F. Fabry, K. Knupp, R. Carbone and R. Serafin (2011). Thermodynamic Profiling Technologies Workshop, *NSFNWS Workshop Report*.
- Hewison, T.J., and C. Gaffard (2006). 1D-VAR retrieval of temperature and humidity profiles from ground-based microwave radiometers, *2006 IEEE MicroRad Proceedings - 9th Specialist Meeting on Microwave Radiometry and Remote Sensing Applications*, pp. 235.
- Janssen, M.A. (1993). *Atmospheric Remote Sensing by Microwave Radiometry*, New York: John Wiley & Sons, Inc.
- Leick, A. (2004). *GPS satellite surveying*, 3rd edn., Wiley, Hoboken
- Levenberg, K. (1944). A method for the solution of certain nonlinear problems in least squares, *Quart. Appl. Math.*, **2**(164).
- Liljegen, J. C. (2002). Microwave radiometer profiler handbook: evaluation of a new multi-frequency microwave radiometer for measuring the vertical distribution of temperature, water vapor, and cloud liquid water, DOE Atmospheric Radiation Measurement (ARM) Program, Argonne National Lab., Argonne, IL, USA.
- Löhnert, U., S. Crewell, O. Krasnov, E. O'Connor, and H. Russchenberg (2008). Advances in continuously profiling the thermodynamic state of the boundary layer: integration of measurements and methods, *J. Atmos. Ocean. Tech.*, **25**, pp. 1251 - 1266.
- Löhnert, U., D.D. Turner, and S. Crewell (2009). Ground-based temperature and humidity profiling using spectral infrared and microwave observations: Part I. Simulated retrieval performance in clear-sky conditions. *J. Appl. Meteor. Climatol.*, **48**, pp. 1017 - 1032, doi: 10.1175/2008JAMC2060.1.
- Lorenc, A.C. (1986). Analysis methods for numerical weather prediction, *Quart. J. Roy. Meteor. Soc.*, **112**, pp. 1177 - 1194.

- Lorenc, A.C., and O. Hammon (1988). Objective quality control of observations using Bayesian methods. Theory, and a practical implementation, *Quart. J. Roy. Meteor. Soc.*, **114**(480), pp. 515 - 543.
- Marquardt, D.W. (1963). An algorithm for least-squares estimation of nonlinear parameters, *SIAM J. Appl. Math.*, **11**(164).
- Martin, L., M. Schneebeli, and C. Matzler (2006). ASMUWARA, a ground-based radiometer system for tropospheric monitoring, *Meteorol. Z.*, **15**, pp. 11–17
- Meunier, V., U. Löhnert, P. Kollias, and S. Crewell (2012). Biases caused by the instrument bandwidth and beamwidth on simulated brightness temperature measurements from scanning microwave radiometers. *Atmos. Meas. Tech. Discuss.*, **5**, pp. 8085 - 8130. doi:10.5194/amtd-5-8085-2012
- Niell, A.E. (1996). Global mapping functions for the atmosphere delay at radio wavelengths, *Journal of Geophysical Research B: Solid Earth*, **101**(2), pp. 3227-3246.
- Padmanabhan, S., S.C. Reising, J. Vivekanandan, and F. Iturbide-Sanchez (2009). Retrieval of atmospheric water vapor density with fine spatial resolution using three-dimensional tomographic inversion of microwave brightness temperatures measured by a network of scanning compact radiometers, *IEEE Transactions on Geoscience and Remote Sensing*, **47**(11), pp. 3708 - 3721.
- Rodgers, C.D. (2000). *Inverse Methods for Atmospheric Sounding: Theory and Practice*, World Scientific.
- Rose, T., S. Crewell, U. Löhnert, and C. Simmer (2005). A network suitable microwave radiometer for operational monitoring of the cloudy atmosphere, *Atmos. Res.*, **75**, pp. 183 - 200.
- Rosenkranz, P. W. (1998) Water vapor microwave continuum absorption: a comparison of measurements and models, *Radio Sci.*, **33**, pp. 919 - 928.
- Scheve, T.M., and C.T. Swift (1999). Profiling Atmospheric Water Vapor with a K-Band Spectral Radiometer, *IEEE Transactions on Geoscience and Remote Sensing*, **37**(3-II), pp. 1709-1718.
- Schween, J.H., S. Crewell, and U. Löhnert (2011). "Horizontal-humidity gradient from one single-scanning microwave radiometer", *IEEE Geoscience and Remote Sensing Letters*, **8**(2), pp. 336 - 340.
- Staelin, D.H. (1966). Measurements and interpretation of the microwave spectrum of the terrestrial atmosphere near 1 -centimeter wavelength. *Journal of Geophysical Research*. **71**(12), pp. 2875-2881.

- Sun, J. (2005). Initialization and numerical forecasting of a supercell storm observed during STEPS, *Monthly Weather Review*, **133**(4), pp. 793-813.
- Thayer, G.D. (1974). IMPROVED EQUATION FOR THE RADIO REFRACTIVE INDEX OF AIR., *Radio Science*, **9**(10), pp. 803-807.
- Townes, C. H., and Schawlow, A. L. (1975). *Microwave spectroscopy*. New York: Dover Publications.
- Vogelmann, H., and T. Trickl (2008). Wide-range sounding of free-tropospheric water vapor with a differential-absorption lidar (DIAL) at a high-altitude station. *Appl. Opt.*, **47**, pp. 2116-2132.
- Weckwerth, T.M., V. Wulfmeyer, R.M. Wakimoto, R.M. Hardesty, J.W. Wilson, and R.M. Banta (1999). NCAR-NOAA lowertropospheric water vapor workshop. *Bull. Amer. Meteor. Soc.*, **80**, pp. 2339–2357.
- Weckwerth, T.M., D.B. Parsons, S.E. Koch, J.A. Moore, M.A. LeMone, B.B. Demoz, C. Flamant, B. Geerts, J. Wang, and W.F. Feltz (2004). An overview of the International H2O Project (IHOP_2002) and some preliminary highlights. *Bull. Amer. Meteor. Soc.*, **85**, pp. 253–277, doi: 10.1175/BAMS-85-2-253.
- Weitkamp, C. (2005). LIDAR: Range-Resolved Optical Remote Sensing of the Atmosphere. *Springer Series in Optical Sciences*.
- Westwater, E.R., S. Crewell, and C. Mätzler (2005a). Surface-based microwave and millimeter wave radiometric remote sensing of the troposphere: a tutorial. *IEEE Geoscience and Remote Sensing Society Newsletter*. March, pp. 16-33.
- Westwater, E.R., S. Crewell, C. Mätzler, and D. Cimini. (2005b). Principles of surface-based microwave and millimeter wave radiometric remote sensing of the troposphere. *Quaderni della Società Italiana di Elettromagnetismo*. **1**(3), pp. 50-90.